NON-HOOKEAN MECHANICS OF CRYSTALLINE MEMBRANES

By

Ryan J.T. Nicholl

Dissertation

Submitted to the Faculty of the

Graduate School of Vanderbilt University

in partial fulfillment of the requirements

for the degree of

DOCTOR OF PHILOSOPHY

in

Physics

August 11, 2017

Nashville, Tennessee

Approved:

Prof. Kirill Bolotin, Ph.D.

Prof. Greg Walker, Ph.D.

Prof. Kalman Varga, Ph.D.

Prof. Norman Tolk, Ph.D.

Prof. Nickolay Lavrik, Ph.D.

ACKNOWLEDGMENTS

I would like to thank everyone that has helped me during my research. Firstly, Kirill Bolotin for always pushing for cleaner data and simple explanations of the physics we study. His past and present group members: Prof. AKM Newaz, Vijayashree PS, Jason Bonacum, Ben Weintrub, Austin Howes, Jan Kirchhof, Dr. Moshe Harats, and Dr. Kirill Greben. Collaborators: Dr. Yevgeniy Puzyrev, Prof. Sokrates Pantelides, Dr. Michael Alles, Wenjun Liao, Rajan Singh, and Prof. Saikat Ghosh. Vanderbilt VINSE staff members: Prof. Tony Hmelo, Dr. Ben Schmidt, Dr. Bo Choi, and Dr. Dmitry Koktysh. ORNL CNMS staff for being very welcoming when I moved part of our laboratory and myself to their facility — taking over their tools with cryogenics, vacuums and high voltage: Dayrl Briggs, Kevin Lester, Bernadeta Srijanto, Dale Hensley, and Ivan Kravchenko. Other researchers in the field that I have shared interesting an helpful discussions with via email and at conferences: Dr. Bob de Alba, Prof. Andrej Kosmrlj, Dr. Issac Storchs, and Prof. Paul McEuen. Special mentions: former colleague and mentor Dr. Hiram Conley for his expertise whilst teaching me nanofabrication and his patience to withstand my constant flow of questions, Dr. Ivan Vlassiouk for engaging discussions and providing me a production line of graphene for fabricating devices, Dr. Nick Lavrik for his integral role in many aspects of experiment design and nanofabrication, always suggesting ideas and being a great host to ORNL's facilities. Fellow graduate students and friends who shared my struggle: Alex Wynn, Kyle Conroy, Dr. Dhiraj Prasai, and Dr. Andrey Klots. My parents, John and Rosemary Nicholl, for their support. Finally and most importantly, my loving wife Jessica Nicholl for her continual encouragement.

TABLE OF CONTENTS

LIST OF TABLES

LIST OF FIGURES

CHAPTER 1

INTRODUCTION

Since the invention of the transistor, the electronics industry has been continually working to reduce its size. Remarkably, transistors used in commercial processors decreased from a ~ 10 μm channel size in 1971 to the state-of-the-art ~ 10 nm channel size used today (2017) [1]. Consequently the processors they comprise have been becoming faster and more powerful at a steady rate.

The same level of size reduction has not happened for machinery — generally classified as (micro) nano-electromechanical systems or (M)NEMS. There are countless commercial examples such as accelerometers (that are used in cell phones and video game consoles), inkjet printheads, and pressure sensors (used in e.g. airbag systems). Nevertheless, device sizes are rarely below $\sim 10 - 100$ μm in size and devices < 1 μm in size do not exist outside research laboratories. This is because it is difficult to fabricate small and thin structures in a way that has low cost and high device yield. Additionally, simply reducing the dimensions of a design will typically not yield a functioning system. There are multiple reasons for this. First, mechanical devices generally have multiple complex interfacing components. Second, the relevant device physics are scale dependent. For example electrostatic forces such as van der Waals interactions cause stiction between components with high surface to volume ratios [2]. Further, basic material properties such as stiffness and breaking strength can change with size due to reduced defect number and increased surface energy contributions [3, 4].

The benefits of miniaturizing machinery goes beyond packing a higher density of components into a product. Machinery at the nanoscale can have fundamental frequencies in the MHz-GHz range allowing photonic coupling to microwaves, large quality factors, tiny active masses, force detection limits as low as 10^{-18} N enabling weighing single molecules; the list goes on [5]. This motivates us to study, understand and manipulate mechanical devices with nanometer dimensions.

1.1 Graphene — a two-dimensional material

One of the biggest challenges in studying nanoscale mechanics is finding a suitable test material that can be procured with ease. Two-dimensional (2D) materials, a recently discovered class of materials only a few atoms thick, fit the bill perfectly. This class of materials includes graphene, monolayer hexagonal boron nitride (hBN), monolayer molybdenum disulfide (MoS_2), and many others [6]. The simplest 2D material is graphene. It is a single layer of carbon atoms arranged in a hexagonal lattice as shown in Fig. 1.1. Graphene can be easily obtained by either mechanically exfoliating thin flakes of graphite through the 'Scotch tape

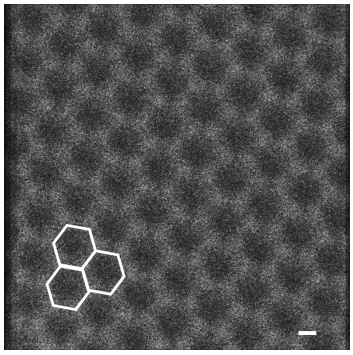

Figure 1.1: Scanning transmission electron microscopy (STEM) image of monolayer graphene, showing the hexagonal structure of the carbon lattice. Scale bar is 0.1 nm.

method' [7] or grown via chemical vapor deposition (CVD) [8]. Critically, graphene is extremely robust making it an ideal candidate for testing nanomechanics at the ultimate, atomic thickness limit. Indeed, a variety of NEMS devices for academic research a such as: resonators [9], switches [10], mass sensors [11] and photonic devices [12] have been made successfully from graphene.

The isolation and study of graphene earned a Nobel prize in 2010, even though the first studies of graphene appeared in the sixties. Graphene is a semimetal with conductance and valance bands touching at the K points. Near the K points the dispersion is linear forming 'Dirac cones'. This means the electrons here behave like massless relativistic particles. This, in part, leads to high electron mobilities [13], an ambipolar electric field effect [7], and supports a plethora of observable quantum phenomena [14, 15]. Despite the lack of band gap in graphene, its electronic properties made much of the research community consider it for superior transistors; but whether this will ever be viable is unclear [16]. Graphene also has a host of other interesting physical properties that promoted heavy study such as: high strength [17], high thermal conductivity [18], and impermeability to gases [19] to name a few.

In this work, we consider mechanical properties of graphene, which are equally remarkable. Multiple techniques were used to measure the stiffness of graphene such as: thin film bulge tests [20], Raman spectroscopy [21], bending apparatus [22], and specialized MEMS actuators [23]. Graphene's stiffness can also be inferred from inelastic neutron scattering of graphite, which measures the phonon dispersion relationship [24]. The simplest mechanical test is indentation with an atomic force microscope (AFM) tip [25]. From these experiments, graphene was found to exhibit a Young's modulus of $E = 1$ TPa. This is typically quoted in 2D units, as 'in-plane stiffness' $E_{2D} = Et \approx 340$ N/m, where t is the thickness of graphene, which is typically taken as 0.345 nm, the spacing between graphite lattice planes. This confirms that graphene is one of the stiffest materials ever discovered due to its sp^2 hybridized bonds. The magnitude of this stiffness is rivaled only by other carbon-based materials.

Furthermore, graphene has a record high breaking strength of ~ 40 N/m which is $100\times$ higher than steel [25]. Such high breaking strength means that graphene can be strained reversibly and elastically up to $\sim 20\,\%$ before failure [26], whereas steel fractures at $\sim 2-3\,\%$. This is a pertinent feature considering that the silicon transistor technology discussed previously was made possible by 'strain engineering' the silicon up to 5% [27]. There, strain modifies the electronic band structure of the silicon, preventing degradation of its electrical properties as the transistors are miniaturized. In a similar way, such a large range of sustainable strain in graphene means there is huge potential for tuning its properties to a greater extent than other materials. For example, the resonance frequency of a graphene nanoribbon can be tuned up to $14\,\%$ of its fundamental frequency [28]. Further, strain engineering is predicted to induce a bandgap [29] or allow study of exotic physics such as 'pseudomagnetic fields' [30]. Pseudomagnetic fields is a phenomenon in which the electrons in graphene behave as if under the influence of a magnetic field, due to strain, when no external field is applied.

In addition to being strong and stiff, graphene is also extremely flexible. There have been a number of attempts at measuring graphene's bending rigidity (κ) directly with widely varying results, for example: using buckled ribbons [31], resonances of few layer graphene cantilevers [32, 33], and resonances of single layer graphene cantilevers (suspended in liquid) [34]. The bending rigidity has also been extracted from the inelastic neutron scattering experiments discussed previously [24]. There, it was found to be $\kappa = 1.2$ eV, in agreement with simulations and comparable to the bending rigidity of biological tissue discussed in the next section. The small magnitude of the bending rigidity is expected for materials that are one atom thick. Correspondingly, the energy contribution due to bending is often neglected in experiments.

1.2 Crumpled membranes

Thin membranes are easy to crumple. This is because of their low bending rigidity and the resulting inability to sustain compressive forces. In graphene, compressive strains as small as $10^{-6}\,\%$ can cause wrinkling and buckling [35]. Sometimes crumpling is a nuisance and needs to be avoided as is the case in solar sails [36] or wrinkled skin [37, 38]. On the contrary, controlled corrugations can be used as an advantage to strengthen materials as is commonly used in the design and fabrication of sheet-metal roof-tops.

Graphene is usually depicted as a perfectly flat sheet (Fig. 1.2a), but in reality it is generally crumpled (Fig. 1.2b). In graphene, crumpling originates from two sources. The first is static wrinkling and folds such as those found in fabrics or sheared materials. This wrinkling likely arises due to uneven stresses at the border of the membrane. Such wrinkling in graphene has been characterized by optical microscopy, scanning electron microscopy (SEM), and atomic force microscopy (AFM) [39–41]. The second crumpling mechanism is related to the out-of-plane (flexural) phonon mode of graphene. Such phonons are unique to 2D

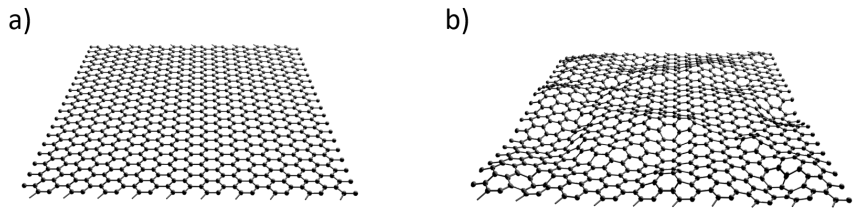

Figure 1.2: Illustration of graphene's structure a) Typical, flat depiction of graphene. b) Realistic depiction of graphene that includes crumpling.

materials and have been characterized by neutron scattering experiments [24]. Further evidence of flexural phonons come from transmission electron microscopy (TEM) [42–44]. Crumpling persists in both supported and freestanding samples [45].

Critically, crumpling has an important role in the mechanical response of thin membranes. One of the first studies of the mechanics of crumpled membrane appeared in the context of biological lipid membranes [46, 47]. Lipid membranes are lipid molecules arranged in a bilayer sheet. They cannot support shear deformations because the molecules can flow past one another. The bending rigidity of such structures is close to that of graphene, $\kappa_0 \sim 3$ eV. It was shown that thermal fluctuations cause these membranes to contract, similar to the behavior seen in an entropic spring, for example, DNA [48]. Another key result is that the bending rigidity of the biological membrane is reduced due to these thermal fluctuations $\kappa \ll \kappa_0$.

The contribution of out-of-plane crumpling to the mechanical properties of *crystalline* materials has also been considered theoretically [49–56]. However, ultra-thin crystalline membranes did not exist until very recently. Crystalline membranes by definition *can* resist shear deformations due to their strong covalent bonds, in contrast to the soft matter discussed previously. In crystalline membranes, in-plane modes are anharmonically coupled to the out-of-plane modes. This nonlinear coupling produces rich and complex renormalization of all mechanical constants. Renormalization in this context means that the elastic properties are not constant and depend on parameters such as system size, temperature, and applied stress. In graphene, crumpling leads to a decrease in the Young's modulus [57, 58], an increase in the bending rigidity [34, 44], variable (and negative) Poisson's ratio [59, 60], and negative thermal expansion [61, 62]. The renormalization of mechanical constants can be demonstrated by a crumpled sheet of paper shown in Fig. 1.3. Here, a flat and crumpled piece of paper are held on one end only. The flat sheet bends very easily whereas the crumpled sheet is rigid and can support its own weight. Theoretical works have mainly focused on the flexural phonon source of crumpling. Only recently has the competition between static wrinkling and flexural phonons been considered [51, 53, 63]. This is important because in experiment both effects may contribute.

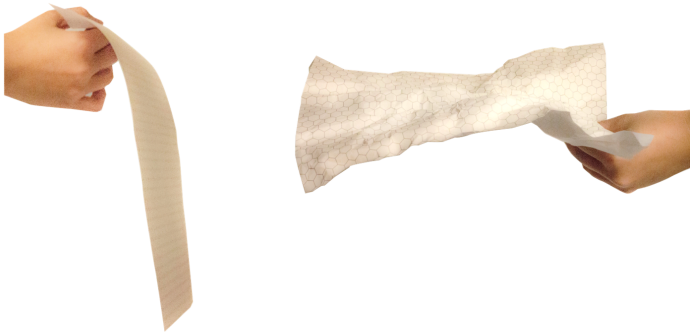

Figure 1.3: Demonstration of elastic constant renormalization with crumpled paper. Left, flat paper is very hard to stretch but bends easily under gravity. Right, crumpled paper becomes easier to stretch but can support more than its own weight under gravity.

The effects of crumpling in 2D materials extend beyond mechanics. Most notably, it has been suggested that the high thermal conductivity of graphene is caused by the large density of states of flexural phonon modes [64]. Also, flexural phonons may explain the temperature-dependent electrical conductivity in graphene since they are another mode of electron scattering [65, 66]. Suppressing the flexural modes via strain engineering may therefore offer a way to vary thermal and electrical conductivity.

1.3 Motivation of the work in the thesis

The goal of the thesis is to explore the effect of crumpling on the mechanics of graphene — the ultimate thin membrane [67]. The effect due to crumpling on the mechanical response of 2D materials is almost universally ignored in prior experiments. This is because the most widely used measurement schemes require high and non-uniform applied stress that suppresses crumpling. Experiments that do probe the interplay between crumpling and graphene mechanics remain highly challenging [34, 57, 68]. To measure the mechanical effects of crumpling we need to develop a new measurement scheme which can apply low and uniform stress, allow non-invasive topography measurements, and be applicable at cryogenic temperatures. The motivating questions of this thesis are the following:

- How does out-of plane crumpling affect the mechanical constants of 2D materials?
- How do we implement measurement techniques sensitive to crumpling?
- Can we identify sources of crumpling and distinguish between static and dynamic crumpling?
- Can we tune the mechanical properties of 2D materials by controlling crumpling?

CHAPTER 2

MECHANICS OF THIN AND CRUMPLED MEMBRANES

The main goal of this chapter is to show how to extract the mechanical properties of 2D materials from experimental data. We focus on two parameters: in-plane stiffness (E_{2D}) and bending rigidity (κ). First, we will present the continuum elasticity theory of thin plates. This is a good starting point to describe the mechanical behavior of graphene. In particular, we derive the deflection response of circular membranes subjected to out-of-plane pressure similar to what is done in experiments and show how to extract in-plane stiffness from deflection data. Then we derive the bending response of rectangular cantilevers, from which we can extract bending rigidity. Second, we consider how the definition of strain is altered for the case of crumpled membranes. Finally, we show how the two main sources of crumpling, static wrinkling/corrugations and flexural phonons, affect the mechanical response of graphene. Specifically, we review the main results of the theory of crumpled crystalline membrane mechanics and how it applies to our experiments.

2.1 Continuum theory of elasticity

Let us first consider the mechanics of flat graphene unaffected by crumpling. Stress (σ) and strain (ε) of that membrane are related through tensorial Hooke's law:

$$\sigma_{ij} = C_{ijkl}\varepsilon_{kl}. \tag{2.1}$$

Here σ_{ij} and ε_{kl} are second rank tensors with nine components each, meaning the stiffness, C_{ijkl}, is a fourth-rank tensor with 81 components. Fortunately, the stiffness tensor can be greatly simplified into only 2 independent elastic constants by assuming an isotropic material [69]:

$$\sigma_{ij} = \lambda\varepsilon_{kk}\delta_{ij} + 2\mu\varepsilon_{ij}. \tag{2.2}$$

Here λ is the Lamé parameter, μ is the shear modulus, and δ_{ij} is the Kronecker delta. This form is often used in the theoretical description of 2D materials because it offers the simplest relationship. Equation 2.2 can be re-parameterized into many pairs of variables. One common formulation uses Young's modulus $E = \frac{\sigma_{xx}}{\varepsilon_{xx}}$, and Poisson's ratio $\nu = -\frac{\varepsilon_{yy}}{\varepsilon_{xx}}$ [70]:

$$\sigma_{ij} = \frac{E}{1+\nu}\left(\varepsilon_{ij} + \frac{\nu}{1-2\nu}\varepsilon_{kk}\delta_{ij}\right). \tag{2.3}$$

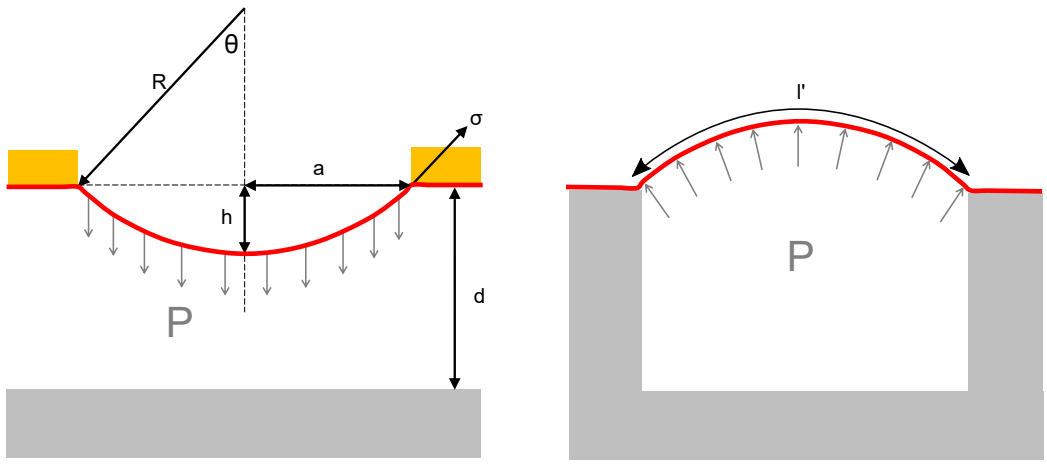

Figure 2.1: Schematic of the two bulge test schemes used in this work. Electrostatic actuation schemes is shown on the left. In it, a uniform force is applied to graphene with an electric field. On the right, a graphene membrane pressurized with gas is shown. R is radius of curvature, θ is the angle subtended from the center of the membrane to the edge, h is center-point deflection, a is membrane radius, σ is internal stress, l' is bulged arc length, and d is the gate distance.

Ideally, to determine the Young's modulus from experimental data, one would design an experiment where the material is pulled perfectly in one direction or equally in all directions. Then, stress and strain can be obtained from force and displacement through geometrical considerations, as explained in the next section. While such an experimental setup is easy to build for a macroscopic material, the nanoscopic size of graphene makes similar experiments more challenging.

2.1.1 Derivation of bulge test equations

Next, from the continuum theory of elasticity, I will derive the main 'bulge test' equations [71] for the analysis of experimental data. In bulge test experiments, uniform pressure is applied to the sample in the out-of-plane direction and its deflection is monitored. The two experimental set-ups used in this work are shown in Fig. 2.1: an electrostatic actuation scheme and a pressurized cavity. In the electrostatic technique, an effective pressure is applied to graphene with an electric field induced by a voltage between the sample and a chip underneath. Experimental details of this scheme can be found in chapter 3. In the pressurized cavity technique, pressure is applied to graphene with compressed gas. Experimental details of this scheme can be found in chapter 4. Technically, the first scheme is a uniform load and the second is uniform pressure. As we will see later, since the deflection of graphene is much smaller than device size ($h \ll a$) the two schemes are equivalent.

Following Landau and Lifshitz [69], lets consider the free energy of a deformed thin plate in the x-y plane with vertical deformation in the out-of-plane direction z, $\zeta(x, y)$ shown in Fig. 2.2. Assuming small

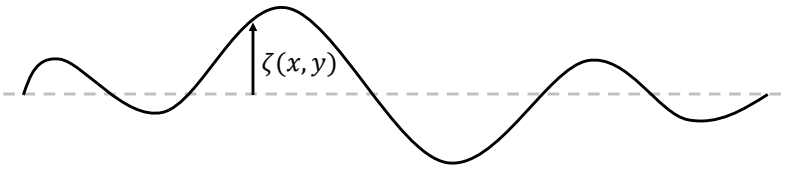

Figure 2.2: Cross-section of deformed membrane with deflection defined by ζ.

deformations (u), the strain tensor reads:

$$\varepsilon_{ij} = \frac{1}{2}\left(\frac{\partial u_i}{\partial x_j} + \frac{\partial u_j}{\partial x_i}\right), \tag{2.4}$$

where x_1 is a spatial coordinate x, x_2 is the spatial coordinate y, u_1 is displacement along the x direction, and u_2 is displacement along the y direction. Each term in the expression describes the infinitesimal in-plane strain in the membrane. The components of the strain tensor expressed in terms of ζ are:

$$u_{xx} = -z\frac{\delta^2\zeta}{\delta x^2}, \tag{2.5}$$

$$u_{yy} = -z\frac{\delta^2\zeta}{\delta y^2}, \tag{2.6}$$

$$u_{zz} = z\frac{\nu}{1-\nu}\left(\frac{\delta^2\zeta}{\delta x^2} + \frac{\delta^2\zeta}{\delta y^2}\right), \tag{2.7}$$

$$u_{xy} = -z\frac{\delta^2\zeta}{\delta x \delta y}, \tag{2.8}$$

$$u_{xz} = u_{yz} = 0. \tag{2.9}$$

The free energy of a deformed material per unit volume is:

$$F = \frac{1}{2}\varepsilon_{ij}\sigma_{ij}. \tag{2.10}$$

Now, substituting σ_{ij} (Eq. 2.3) and ε_{ij} (Eq. 2.4) using Eqs. 2.5-2.9 into Eq. 2.10, we arrive at Eq. 2.11

which is an expression for the free energy of a deformed plate in terms of Young's modulus and Poisson's ratio:

$$F = \frac{Et^3}{24(1-\nu^2)} \int\int \left[\left(\frac{\partial^2 \zeta}{\partial x^2} + \frac{\partial^2 \zeta}{\partial y^2} \right)^2 + 2(1-\nu) \left\{ \left(\frac{\partial^2 \zeta}{\partial x \partial y} \right)^2 - \frac{\partial^2 \zeta}{\partial x^2} \frac{\partial^2 \zeta}{\partial y^2} \right\} \right] dxdy. \tag{2.11}$$

Here, t is the membrane thickness and the quantity $\kappa = \frac{Et^3}{12(1-\nu^2)}$ is known as the effective bending rigidity of a thin membrane. The first term is related to the average curvature of the membrane: $\left(\frac{1}{R_1} + \frac{1}{R_2} \right)^2$ and the second term in curly braces is related to the Gaussian curvature: $\frac{1}{R_1 R_2}$, where R_1 and R_2 are the principle radii of curvature. For a clamped system the Gaussian curvature is zero. This is typically shown by applying two fixed boundary conditions and considering variations in the free energy (Eq. 2.11). The first boundary condition, $\zeta = 0$, ensures there is no out-of-plane deflection at the edge. The second boundary condition, $\frac{\partial \zeta}{\partial n} = 0$ (where n is the surface normal), ensures that the membrane remains horizontal at the edge. This calculation is too cumbersome to present here, the reader is directed to any textbook on elasticity theory (see e.g. [69, 72]). With these simplifications, Eq. 2.11 can be simplified to:

$$F = \frac{1}{2} \int \kappa (\nabla^2 \zeta)^2 dxdy. \tag{2.12}$$

The equation describing equilibrium of the membrane under uniform applied pressure P in the downward direction can be found by functional minimization of Eq. 2.12:

$$\kappa \nabla^4 \zeta = P. \tag{2.13}$$

Unfortunately, this result cannot be directly applied to graphene. For graphene, the assumption of small deflection that was silently assumed in derivation of Eq. 2.13 breaks down. Indeed, any realistic displacement magnitude is larger than the thickness of graphene $t = 0.34$ nm. Therefore we have to include a higher order term in the strain tensor as follows:

$$\varepsilon_{ij} = \frac{1}{2} \left(\frac{\partial u_i}{\partial x_j} + \frac{\partial u_j}{\partial x_i} + \frac{\partial \zeta}{\partial x_i} \frac{\partial \zeta}{\partial x_j} \right). \tag{2.14}$$

Once again, the free energy can be obtained by substituting σ_{ij} (Eq. 2.3) and ε_{ij} (Eq. 2.14) into Eq. 2.10 [73]:

$$F = \frac{1}{2} \int \left[\kappa (\nabla^2 \zeta)^2 + \lambda \varepsilon_{ii}^2 + 2\mu \varepsilon_{ij} \varepsilon_{ij} \right] dxdy. \tag{2.15}$$

While Eq. 2.12 only included the term related to bending rigidity, Eq. 2.15 includes additional terms related

to the stretching energy: $\lambda\varepsilon_{ii}^2 + 2\mu\varepsilon_{ij}\varepsilon_{ij}$, which originated from the higher order term, $\left(\frac{\partial\zeta}{\partial x_i}\frac{\partial\zeta}{\partial x_j}\right)$, in Eq. 2.14. Next, by minimizing the free energy described by Eq. 2.15, we arrive at the following equilibrium conditions:

$$\frac{Et^3}{12(1-\nu^2)}\nabla^4\zeta - t\frac{\partial}{\partial x_j}\left(\sigma_{ij}\frac{\partial\zeta}{\partial x_i}\right) = P, \tag{2.16}$$

$$\frac{\partial\sigma_{ij}}{\partial x_j} = 0. \tag{2.17}$$

Equations 2.16 and 2.17 are the Föppl von Karman equations. They are difficult to solve and are the general starting point for most modern theories of elasticity. These equations can be simplified in particular situations. As before, for graphene, since $\zeta > t$ and we consider large forces, the first term in Eq. 2.16 is negligible. We also redefine bulk stress to 'in-plane' stress: $t\sigma_{ij} \rightarrow \sigma\delta_{ij}$. This yields a simple expression for elastic equilibrium of a membrane subject to pressure P:

$$\sigma\nabla^2\zeta = -P. \tag{2.18}$$

Differential equation 2.18 is a classic example of Poisson's equation in elasticity. Now lets solve Eq. 2.18 for a circular membrane of radius a that is clamped at the edge subject to a downward pressure P. This is the main geometry used in this work. In polar coordinates Eq. 2.18 becomes:

$$\frac{1}{r}\frac{d}{dr}\left(r\frac{d\zeta}{dr}\right) = -\frac{P}{\sigma}. \tag{2.19}$$

The solution to Eq. 2.19 is:

$$\zeta(r) = \frac{Pa^2}{4\sigma}\left(1-\frac{r^2}{a^2}\right) = h\left(1-\frac{r^2}{a^2}\right), \tag{2.20}$$

where h is the center-point deflection. The solution is of the form $\zeta(r) \propto \left(1-\frac{r^2}{a^2}\right)$, i.e. parabolic. For $h << a$ the deflection is nearly spherical. Note that this solution is different from that of the biharmonic differential equation. 2.13, which has solution of form $\zeta \propto \left(1-\frac{r^2}{a^2}\right)^2$. The key difference of the latter solution is that $\frac{d\zeta}{dr} = 0$ at $r = a$ due to non-negligible bending rigidity.

Next, we can determine $P(h)$ by combining low and high deflection regimes of Eqs. 2.16 and 2.17 yielding a stress dominated term at small defections ($P \propto h$) and a stiffness dominated term ($P \propto h^3$) at high deflections:

$$P = \frac{4\sigma_0}{a^2}h + \frac{8}{3}\frac{Et}{1-\nu}\frac{h^3}{a^4}. \tag{2.21}$$

Again, the reader is directed elsewhere for more details (e.g Refs. [69, 73, 74]). Equation 2.21 is known as the bulge test equation in thin film mechanics and is the basis for extracting the mechanical constants of graphene from applied pressure P and measured deflection of center-point h. For an atomically thin membrane such as graphene, we define in-plane stiffness as $E_{2D} = Et$. It is the 2D equivalent to Young's modulus. The bulge test subjects the membrane to biaxial stress and strain. Consequently, $\widetilde{E}_{2D} = \frac{E_{2D}}{1-\nu}$ is known as the biaxial modulus. The numerical pre-factors of each term are approximations which allow for the extraction of the elastic constants within $10\ \%$ if $h \ll a$ [74]. Following the same derivation for a point load retrieves a similar expression used in AFM indentation experiments (discussed in Appendix B).

2.1.2 Geometrical derivation of bulge test equations

Here I will derive the stress and strain relations for a bulging circular thin film only from *geometrical considerations* and show the corresponding relationship is identical to Eq. 2.21 derived in the previous section [71, 75–77]. In this way, it is clear that the bulge test method to extract stress and strain does not depend on the nature of the deformation. I will also show that the stress and strain state can be calculated by knowing only the applied pressure (P), center-point deflection (h), and diameter (a) of the membrane.

To derive the expression for stress we consider the simplified case where the equilibrium of external pressure and restoring elastic tension results in a perfectly spherical membrane shape. In this case the radius of curvature R, is equal to membrane radius a. It can be shown that this simple derivation agrees with the general case of $a \ll R$ [78]. The force due to external pressure P is balanced by in-plane biaxial stress $\sigma = \sigma_{3D}t$:

$$P\pi R^2 = \sigma 2\pi R. \tag{2.22}$$

Solving for σ yields:

$$\sigma = \frac{PR}{2}. \tag{2.23}$$

Referring to Fig. 2.1, simple geometry allows us to find an expression for R as follows:

$$R = \frac{h}{2} + \frac{a^2}{2h} \rightarrow R = \frac{a^2}{2h} \text{ for } h \ll a. \tag{2.24}$$

Combining Eq. 2.23 and Eq. 2.24 yields:

$$\sigma = \frac{Pa^2}{4h}. \tag{2.25}$$

Note that this is identical to solution of the Föppl von Karman equations in Section 2.1, specifically Eq. 2.20 for $\zeta(r=0)=h$. We can also easily calculate the strain state of the membrane. Strain is given by:

$$\varepsilon = \frac{l' - l}{l} = \frac{\Delta l}{l}. \tag{2.26}$$

The bulged arc length is:

$$l' = 2R\theta, \tag{2.27}$$

where l is the length of the arc, l' is the length of the bulged arc, and θ is the angle between the membrane edge and the center (see Fig. 2.1). Since the membrane is deformed symmetrically, the change in arc length across perpendicular directions are identical. This means the strain is biaxial. The angle θ can be expressed in terms of a and R as follows:

$$\theta = \arcsin\left(\frac{a}{R}\right). \tag{2.28}$$

The original length of the flat membrane is simply: $l = 2a$, as shown in Fig. 2.1. Recalling Eq. 2.24 yields the following expression for strain:

$$\varepsilon = \frac{2R\arcsin\left(\frac{a}{R}\right) - 2a}{2a} = \frac{a}{2h}\arcsin\left(\frac{2h}{a}\right) - 1. \tag{2.29}$$

The first term in the Taylor expansion of Eq. 2.29 is our final equation for biaxial strain:

$$\varepsilon = \frac{2h^2}{3a^2}. \tag{2.30}$$

In general there can exist a stress in the flat membrane before the application of pressure. This is called built-in stress (σ_0). The relation between stress and strain is then:

$$\sigma = \widetilde{E}_{2D}\varepsilon + \sigma_0. \tag{2.31}$$

Using Eq. 2.25 and 2.30 and knowledge of applied pressure yields:

$$P = \frac{4\sigma_0}{a^2}h + \frac{8\widetilde{E}_{2D}}{3a^4}h^3. \tag{2.32}$$

Equation 2.32 derived from geometrical considerations is identical to Eq. 2.21 derived from the Föppl von Karman equations. From these expression, the mechanical constants such as $\widetilde{E}_{2D}$ can be extracted from

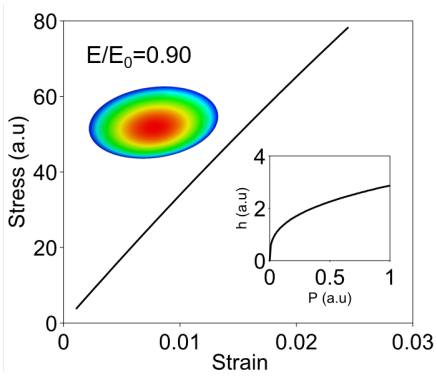

Figure 2.3: Finite element analysis of a clamped circular membrane loaded in the out-of-plane direction. Main panel shows the stress-strain response of the membrane. The inset (bottom right) shows computationally obtained center-point deflection (h) vs. applied pressure (P). Inset (top left) shows deformed geometry where color is deflection. The in-plane stiffness obtained from the slope of the stress-strain curve is within $10\ \%$ of the value obtained from fitting to the $P(h)$ data. This confirms the use of either technique to experimentally extract the mechanical constants of thin membranes.

experimentally measured $P(h)$. However, instead of fitting the $P(h)$ response, one can plot the stress vs. strain curves using Eqs. 2.25 and 2.30. The slope of this curve is biaxial in-plane stiffness $\tilde{E}_{2D}$.

We tested the accuracy of these approximate expressions Eq. 2.21 and stress-strain analysis Eqs. 2.25 and 2.30 by comparing their predictions to exact numerical calculations obtained using commercial finite element analysis (FEA) software, ABAQUS (Fig. 2.3). We used shell elements with fixed edges. The stiffness of membranes was set to an arbitrary $E_0 = 3.5$ GPa. We found that the slope of the stress strain curve is identical to $\widetilde{E}_{2D}$ as determined via the bulge test equations. Also, the obtained E does not deviate from the pre-set E_0 by more than $10\ \%$ in agreement with more detailed research [76].

2.1.3 Bending Beams

We have seen that the mechanical response of membranes only depends on stiffness and not bending rigidity. To access bending rigidity, we consider the cantilever geometry. The bending rigidity is defined as:

$$\kappa = \frac{dM}{dC}, \tag{2.33}$$

where M is bending modulus and C is bending curvature. We have seen from Eq. 2.11 that the bending rigidity can be related to the Young's modulus for a beam with thickness t by $\kappa = \frac{Et^3}{12(1-\nu^2)}$.

The bending of cantilevers can be described by the effective spring constant (k) relating applied force (F) and displacement (x) of the cantilever's end: $F = -kx$. For a rectangular beam of width W, length L, and

thickness t, the effective spring constant is [72]:

$$k = \frac{Et^3 w}{4L^3}. \tag{2.34}$$

The spring constant is related to κ through geometry [79]:

$$\kappa = \frac{kL^3}{3W}. \tag{2.35}$$

For the 5×5 μm^2 graphene cantilevers considered in chapter 5, assuming $\kappa = 1$ eV yields a spring constant of $k \approx 1 \times 10^{-8}$ N/m. This number is a good reference point to bear in mind. Even a cantilever this short is 10^6 times softer than commercial AFM cantilevers.

2.2 Renormalization of elastic constants due to crumpling

This section is devoted to considering the renormalization of the elastic constants of 2D membranes due to the two primary crumpling sources: static wrinkling and flexural phonons.

2.2.1 Hidden area

First we need to quantify crumpling strength through a concept known as 'hidden area' [58]. Consider Fig. 2.4 illustrating stretching a crumpled membrane. The hidden area ΔA_0 is the difference between the true area of the membrane A_0, and the area of its projection onto a plane parallel to the membrane at zero applied stress. ΔA_0 is the amount of area 'hidden' within out-of-plane crumpling and is 'revealed' when the membrane is stretched to the point of becoming flat. For a flat membrane the hidden area is zero. Consider the change in projected area ΔA of a crumpled square sheet when the length of its side l is increased by a small amount Δl:

$$\Delta A = A' - A = l^2 + 2l\Delta l + \Delta l^2 - l^2 = 2l\Delta l. \tag{2.36}$$

The fractional change in area can be expressed as:

$$\frac{\Delta A}{A} = \frac{2\Delta l}{l} = 2\varepsilon. \tag{2.37}$$

Here we have used the definition of strain $\varepsilon = \frac{l'-l}{l} = \frac{\Delta l}{l}$. Now, if a crumpled sample is stretched enough to become flat, Eq. 2.37 can be used to quantify the amount of hidden area ΔA_0. There, the change in area is due to unravelling the crumpling present in the membrane. So the difference in the projected area of crumpled

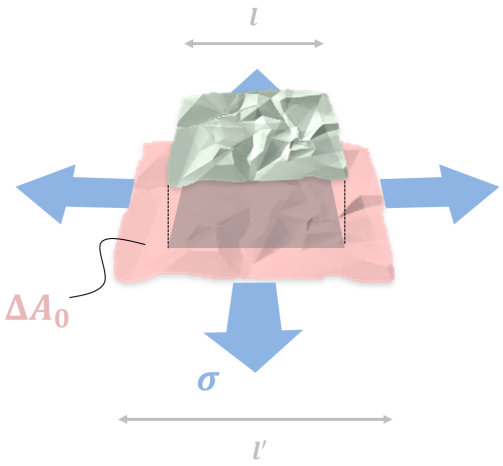

Figure 2.4: Hidden area and strain in a crumpled membrane. Original membrane length l is increased by uniform stress σ resulting in new length l'. ΔA_0 represents the amount of area unravelled due to uncrumpling and is the difference between the true membrane area and its projection (shown as the shadow).

membrane and the projected area of the flat membrane can be expressing using Eq. 2.37:

$$\frac{\Delta A_0}{A} = 2\varepsilon_t. \tag{2.38}$$

where ε_t is the 'threshold' amount of strain required to flatten the sample.

Strain in a crumpled membrane involves changes in both bond lengths in the material *and* changes in device geometry. The change in device geometry can lead to large effective extensions due to unravelling crumpling even if the bonds are not stretched very much. Therefore, when dealing with strain in 2D materials one needs to distinguish between change of the true material size and the projected size [80]. For flat materials they are identical — this is an implicit assumption of the continuum theory of elasticity discussed previously. However, for crumpled materials they can be considerably different. In chapter 4 we show how to measure this difference experimentally.

2.2.2 Static wrinkles and corrugations

We will first consider a simple case of 1D wrinkling and analyze changes in the elastic constants due to this wrinkling. We will discuss how wrinkles form in thin plates due to shearing and how their presence affects the mechanical constants the of a material. Compression and shear in thin materials cause wrinkling and buckling since the energy cost of out-of-plane buckling is much less than that of in-plane compression.

One can predict the relationship between sample length L, thickness t, and Poisson's ratio ν of a rectangular sample and the amplitude (δ) and wavelength (λ) of wrinkling [37, 81]. The main assumption of the

following analysis is that observed wrinkling is a single 1D sinusoid. For wrinkles that form predominantly due to uniaxial tension, the relationship is:

$$\frac{\delta\lambda}{L} = \sqrt{\frac{8\nu}{3(1-\nu^2)}}t. \tag{2.39}$$

For wrinkles that form predominantly due to shearing, the relationship is:

$$\frac{\delta\lambda}{L} = \sqrt{\frac{8}{3(1+\nu)}}t. \tag{2.40}$$

Direct measurement of the quantity $\frac{\delta\lambda}{L}$ revealed that Eqs. 2.39 and 2.40 hold for multilayer graphene up to 20 nm thick [41, 82]. To our knowledge, the same type of analysis for circular membranes has not been performed because such geometry is much more complicated to analyze.

Now we consider the changes in the effective elastic constants in a sinusoidally corrugated sheet as shown in Fig. 2.5. The effective in-plane stiffness and bending rigidity are [83, 84]:

$$E_{xx} = \frac{E}{6(1-\nu^2)}\left(\frac{t}{\delta}\right)^2, \tag{2.41}$$

$$\kappa_{yy} = \kappa + 0.5E\delta^2 t. \tag{2.42}$$

Here E is the uniaxial stiffness of the isotropic sheet. Equation 2.41 shows that the stiffness is softened due to corrugations by a factor $\left(\frac{t}{\delta}\right)^2$. This softening only occurs when stretching along the wrinkles (in this case, x-direction). There is no large change in stiffness when stretching perpendicular to the wrinkles (y-direction). Correspondingly, the bending rigidity is increased perpendicular to the wrinkles (bending along y-direction) by an additive term proportional to δ^2 and E. The pre-factor ~ 0.5 is an estimate of the increased moment of inertia due to effective increased thickness.

We used ABAQUS FEA to confirm that wrinkling leads to softening of the effective in-plane stiffness and produces nonlinear stress-strain curves as shown in Fig. 2.6. We used a rectangular ribbon geometry with wrinkles induced following the approach by Wong et al. [85]. The membrane was loaded under constant pressure. Its effective stress and strain were extracted. We observed a nonlinear stress-strain relationship (Fig. 2.6b) with the degree of nonlinearity depending on wrinkle amplitude δ. The effective stiffness of the wrinkled sample was calculated as a derivative of the stress-strain curve normalized by the stiffness of unwrinkled membrane E_0. The membrane is seen softened in the regime of small strain.

We also used the FEM data to illustrate the hidden area metric as shown in Fig. 2.6c. The fractional hidden area is defined from Eq. 2.38 is $\frac{\Delta A_0}{A} = 2\varepsilon_t$. The positions corresponding to threshold strains for

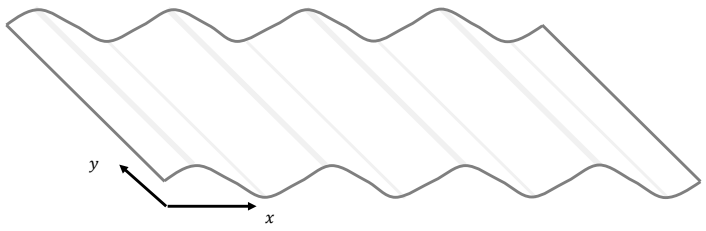

Figure 2.5: Illustration of a sinusoidally corrugated sheet. The sheet is corrugated in the x-direction. The effective in-plane stiffness is reduced along this direction. The effective bending rigidity is increased when bending along the y-direction.

different amounts of wrinkling calculated from geometry are shown by dashed lines. Initially, at strains $< \varepsilon_t$ the material is softened due to wrinkling. At strains $> \varepsilon_t$, the sample behaves linearly with constant stiffness as obtained in the FEM simulation.

Note that like all classical elastic theory, Eqs. 2.39, 2.40, 2.41 and 2.42 are derived for materials with finite thickness and whose material stiffness in stretching perpendicular to corrugations comes from compression and tension of opposite material surfaces. For a membrane such as graphene with only one layer it is less obvious what will happen. One might expect stretching perpendicular to corrugations should yield zero stiffness until the membrane is flat. One can see this is true by smoothly deforming paper along one dimension. It is almost impossible to feel the deformation forces it takes to flatten out the sheet — yet it extends by a large amount. Such an experiment with graphene would be extremely hard to realize.

To describe realistic crumpling of a membrane, we must introduce two complications to the 1D wrinkling models outlined above. First, the membrane is wrinkled along all directions rather than only one direction. Second, the amplitude of crumpling varies for different modes. One treatment [58] considers a membrane in initially warped configurations by summing distributions of sinusoids. Here no internal stress is considered and the crumpling height defined by $\langle h^2 \rangle = \frac{\delta^2}{Aq^{d_h}}$ where δ is an amplitude, A is membrane area and d_h is a constant which controls the distribution the crumpling wavevectors q. The result of this theory is that the mechanical constants E and κ are renormalized due to wrinkling. The renormalized elastic constants from this treatment are:

$$E_R \propto \sqrt{\frac{\kappa}{E\langle h^2 \rangle}}, \tag{2.43}$$

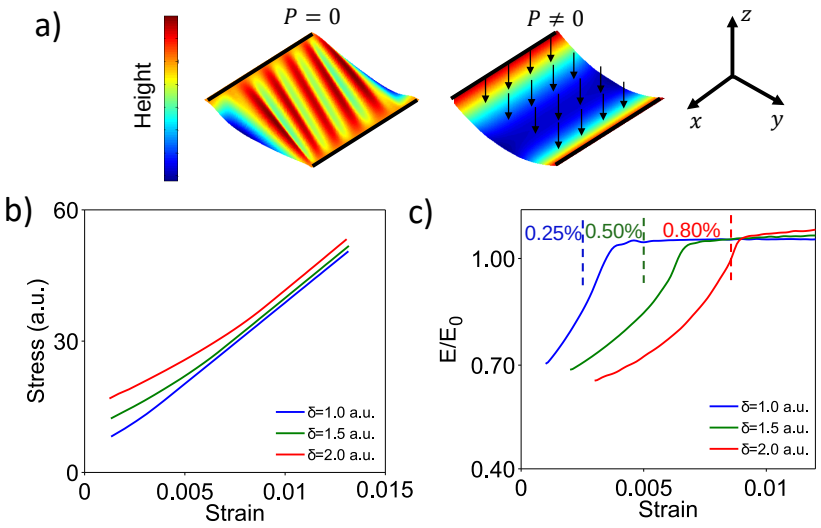

Figure 2.6: ABACUS FEM a) The model of a wrinkled membrane in unloaded ($P = 0$) and loaded ($P \neq 0$) configurations. Pressure is in $-z$ direction. b) Extracted stress-strain curves for different amplitudes (δ) of wrinkles. c) Extracted in-plane stiffness vs. strain. The material is softened at small strains. When strain is high enough to unravel the wrinkling (dashed markers at 0.25 %, 0.50 % and 0.80 %) we retrieve the defined material stiffness.

$$\kappa_R \propto \sqrt{\frac{E\langle h^2 \rangle}{\kappa}}. \tag{2.44}$$

The constant of proportionality for these relationships is ~ 1. It can be determined more precisely numerically. For $d_h > 2$ there is a size dependance of the elastic constants. In particular, the thermal fluctuations considered in the next section have $d_h = 4$, and therefore the elastic constants depend heavily on system size. It is interesting to compare Eqs. 2.43 and 2.44 for crumpled membranes to Eqs. 2.41 and 2.42 for 1D corrugations. The renormalization for crumpling scales with crumpling amplitude h as opposed to wrinkle amplitude squared (δ^2). Also, membrane thickness does not directly enter Eqs. 2.43 and 2.44. Instead, there is an effective elastic thickness described by the $\sqrt{\frac{E}{\kappa}}$ term.

2.2.3 Flexural phonons

Now we discuss out-of-plane, flexural phonons and their impact on crystalline membrane mechanics. To appreciate their interesting properties, I first briefly mention their relationship to mechanics. In bulk condensed matter systems the in-plane stiffness is related to acoustic phonon dispersions near the Brillouin zone center (TA and LA modes). This is because these modes have linear dispersion $\omega = v_g q$, where v_g is the speed of sound in the material which is dictated by the elastic constants. In *2D* condensed matter systems there are also out-of-plane (flexural) phonons in the ZA and ZO branches. These out-of-plane phonons have very different properties than in-plane phonons. Namely, the ZA branch has a quadratic dispersion relationship [86]:

$$\omega_q = \sqrt{\frac{\kappa q^4 + 2(\lambda + \mu)\varepsilon q^2}{\rho}}, \tag{2.45}$$

where ω is phonon frequency, q is phonon wavevector, ρ is mass density of graphene, ε is strain, κ is the bending rigidity and λ and μ are the elastic Lamé coefficients. For the simple case $\varepsilon = 0$ the dispersion is $\omega = \sqrt{\frac{\kappa}{\rho}} q^2$. We can then easily estimate the total number of flexural phonons (N) excited at finite temperature (T) [64]:

$$N_{flex} = \frac{1}{2\pi} \int \frac{q \, dq}{\exp\left(\frac{\hbar}{k_B T}\sqrt{\frac{\kappa}{\rho}} q^2\right) - 1}. \tag{2.46}$$

We note that this integral is divergent at $q \to 0$. This divergence in the flexural phonon number dominates the physical properties of a 2D membrane. For example, it leads to reduced in-plane stiffness and increasing bending rigidity.

Now let us consider the renormalization of the elastic constants due to dynamic crumpling from flexural phonons. Any fluctuation due to flexural phonons cannot occur without also stretching the membrane since bending and stretching are coupled (Eq. 2.14). What is the minimum amplitude of thermal fluctuations, $\langle u^2 \rangle$, that coupling between the bending and stretching modes affect the measurable mechanical properties

of the membrane? One estimate was performed by Nelson et al. [49]. The authors of Ref. [49] compared the magnitude of the terms in Eq. 2.15 with deflection ζ stemming from thermal fluctuations, $\langle u^2 \rangle \approx \frac{k_B T}{\kappa}$, where k_B is the Boltzmann constant, and T is temperature. The result from this analysis is:

$$\langle u^2 \rangle \geq \frac{1}{\gamma} l^2 \tag{2.47}$$

where $\gamma = \frac{E l^2}{\kappa}$ is the Föppl von Karman number and is a metric used to compare how easy it is to stretch or bend a membrane of linear size l. Very large γ means it is much easier to bend than to stretch. For a 200 μm sheet of graphene $\gamma \approx 10^{12}$. This is 6 orders of magnitude larger compared to the same ratio for paper. In other words, because graphene has an extremely high γ, the coupling between bending and stretching occurs for even tiny out-of-plane deformations. Because of this, Eq. 2.47 suggests that the elastic constants are renormalized for practically any amplitude of flexural phonons. The first order correction to the bending rigidity (κ) was estimated with perturbation theory [49, 73]:

$$\delta\kappa = \frac{3TE}{8\pi\kappa q^2} = \frac{3T}{8\pi}\gamma \tag{2.48}$$

The appearance of the Föppl von Karman number means that the predicted corrections to the bending rigidity ($\delta\kappa$) are large ($\geq \kappa$). Therefore, perturbation theory is not applicable. There are a number of ways to tackle this problem. Most formal theory considers the free energy Hamiltonian (Eq. 2.15) that is used to derive the Föppl von Karman equations. The energy of the crumpled membrane is then calculated using approaches such as: iterative perturbation, the self-consistent screening approximation (SCSA), renormalization group theory, atomistic simulations, and numerical models [49–51, 53–55, 87]. The result of these sophisticated theories are the following expressions for the renormalized elastic constants:

$$E_R \propto E \left(\frac{l_{th}}{l} \right)^{2-2\eta}, \tag{2.49}$$

$$\kappa_R \propto \kappa \left(\frac{l}{l_{th}} \right)^{\eta}. \tag{2.50}$$

Here $\eta \approx 0.8$ for thermal fluctuations and l_{th} is the 'cross-over length' representing the minimum sample size in which renormalization affects are important:

$$l_{th} = \sqrt{\frac{32\pi^3\kappa}{3Ek_BT}}. \tag{2.51}$$

For graphene, $l_{th} \approx 3$ nm. This means that for virtually any realistic sample size with dimensions $l \gg l_{th}$,

the elastic constants are renormalized. Specifically, in-plane stiffness is reduced and bending rigidity is increased. This is because when stretching a crumpled membrane one effectively pays the small energy cost to bend the membrane locally. Conversely, when bending a crumpled membrane one effectively pays the larger energy cost of stretching the membrane. Both effects originate in the coupling between bending and stretching caused by crumpling.

Now that we understand how the elastic constants of a crystalline membrane are renormalized, we derive a simple stress-strain relationship of graphene that is crumpled due to flexural phonons. We follow a modified derivation by Helfrich and Servuss [46]. First we consider a crumpled membrane. For any arbitrarily crumpled membrane the displacement profile can be decomposed into Fourier modes $u_q = \exp(iqr)$, where q is the wavevector of a single mode, and u_q is the displacement of graphene from the x-y plane. Let us consider a membrane crumpled by a single mode. For a small section of this mode, the difference of the membrane area and the projected area is:

$$\Delta A = A(\cos(\theta) - 1) \approx -A\frac{\theta^2}{2} \approx -A\frac{\tan(\theta)^2}{2} \tag{2.52}$$

where θ is the angle a section of the membrane makes with the x-y plane. For small angles θ, $|\nabla u| \approx \tan(\theta) = iqu_q$. Then, ΔA per mode q can be expressed as:

$$\Delta A_q = -\frac{1}{4}Aq^2|2u_q|^2. \tag{2.53}$$

It costs energy $\sigma\Delta A_q$, where σ is stress, to increase the in-plane area of the membrane by ΔA_q. Then, the stretching energy associated with mode q is:

$$\frac{1}{4}A\kappa q^4|2u_q|^2. \tag{2.54}$$

From the equipartition theorem, we can find the average amplitude per mode:

$$|u_q|^2 = \frac{k_B T}{A\left(q^4\kappa + q^2\sigma\right)}, \tag{2.55}$$

where k_B is Boltzmann constant, and T is temperature. Next, from Eq. 2.53 and 2.55 and we can calculate the amount of crumpling due to a single mode:

$$\left(\frac{\Delta A}{A}\right)_q = q^2\frac{k_B T}{A\left(q^4\kappa + q^2\sigma\right)}. \tag{2.56}$$

As discussed earlier, κ, the bending rigidity, is renormalized due to crumpling. Therefore we use Eq. 2.50

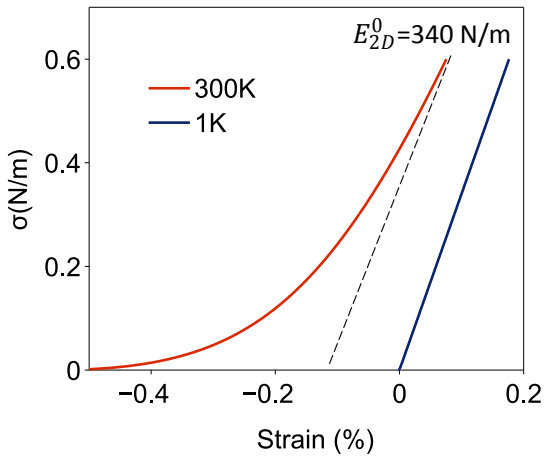

Figure 2.7: The stress-strain curves for graphene subject to thermal crumpling obtained numerically from Eq. 2.58. At = 1 K, the flexural phonons are almost completely suppressed and the stiffness of graphene is close to that of flat graphene: 340 N/m. At $T = 300$ K, graphene appears much softer due to a large amount of thermal crumpling.

to write: $\kappa(q) = \kappa_0 + k_B T B \left(\frac{q_0}{q}\right)^\eta$, with $B = 5.9T^{(\frac{\eta}{2}-1)}$, $q_0 = 2\pi\left(\frac{E^0_{2D}}{\kappa_0}\right)^{1/2}$, $\eta = 0.85$, $E^0_{2D} = 340$ N/m and $\kappa_0 = 1$ eV [73]. We must sum the total contribution from all modes by integrating. This yields the total decrease in projected area ΔA in a crumpled membrane:

$$\frac{\Delta A}{A} = -\frac{1}{2\pi}\int_{q_{min}}^{q_{max}} \frac{k_B T}{(q^2\kappa(q) + \sigma)} q dq. \tag{2.57}$$

In this expression the lower integration limit $q_{min} = \frac{2\pi}{\sqrt{A}}$ is the lowest possible mode of excitation and is related to the membrane size. The upper limit $q_{max} = \sqrt{\frac{3k_B T E^0_{2D}}{8\kappa_0^2 \pi}}$ ensures only phonons with wavelength $> l_{th}$ contributing to stiffness are counted.

To compute the stress-strain relationship of a crumpled material, we convert changes in area to lengths changes (section 2.2.1) and add the contribution due to stretching of the flat membrane:

$$\varepsilon = \frac{1}{2}\frac{\Delta A}{A} + \frac{\sigma}{E^0_{2D}}. \tag{2.58}$$

The two terms in this expression stem from two sources of strain. The first term is crumpling due to flexural phonons and the second term is stretching of carbon-carbon bonds with effective stiffness $E^0_{2D} = 340$ N/m. The stress-strain curves computed from the model are plotted in Fig. 2.7.

Renormalized elastic constants changes the bulge test expressed in Eq. 2.21 to [88]:

$$P = Ah + Bh^{3+2\mu} \tag{2.59}$$

where $\mu = \frac{2-2\eta}{2-\eta} \approx 0.28$ and $B \propto \left(\frac{\kappa}{k_B T}\right)^{\mu} \frac{E}{L^{4+2\mu}}$ is an effectively reduced in-plane stifffness. Also note the non-trivial power of deflection $h^{3+2\mu}$, where for a flat membrane this is simply h^3.

2.2.4 General stress-strain relationship

Recently, a more sophisticated theory [63] was developed to describe the 'anomalous' Hooke's law of crumpled graphene with static or dynamic crumpling:

$$\varepsilon(\sigma) = \frac{\sigma_*}{E}\left[\frac{\sigma}{\sigma_*} + \frac{1}{\alpha}\left(\frac{\sigma}{\sigma_*}\right)^{\alpha}\right]. \tag{2.60}$$

Here α is an exponent which determines the degree of nonlinearity caused by crumpling and σ_* is the 'crossover stress', a measure of the stress required to flatten the membrane. Qualitatively, the mechanical behavior described by Eq. 2.60 is that of two springs in series. The first linear 'spring', with stiffness $\widetilde{E}_{2D} \sim 400$ N/m describes stretching of C-C bonds, while the second, nonlinear 'spring' corresponds to uncrumpling of a membrane. The theory predicts $\alpha \sim 0.1$ for static disorder (wrinkling) and $\alpha \sim 0.5$ for thermal fluctuations (flexural phonons). The Hooke's law is called 'anomalous' because the stress-strain relationship is nonlinear at low stress governed by the second term in Eq. 2.60. This is in contrast to nonlinearities in bulk materials which occur at very large stress. This theory is particularly useful because it allows us to identify the source of crumpling and only requires three fitting parameters.

2.2.5 Effect of finite bending rigidity

In the derivations of the bulge test Eq. 2.21, we assumed negligible bending rigidity of graphene. For flat graphene, with $\kappa = 1$ eV, this assumption is fully justified. However, as discussed previously, crumpling increases κ. So can we still neglect the effects of bending in the bulge test for crumpled graphene?

To answer this question, we estimate the relative magnitude of the bending ($U_b = \frac{1}{2}\kappa\frac{1}{R^2}$) and stretching ($U_s = \frac{1}{2}E\varepsilon^2$) energies per unit area of a graphene sheet:

$$\frac{U_s}{U_b} = \frac{E}{\kappa}\varepsilon^2 R^2 \approx 10^9. \tag{2.61}$$

Here $R = 25$ μm is the minimum radius of curvature seen in experiment for a $l = 10$ μm device, and corresponding strain $\varepsilon = 0.0067$. This estimate quantitatively confirms that for flat graphene bending rigidity is negligible. Now to describe crumpled graphene, we substitute the elastic constants E and κ with the renormalized ones E_R and κ_R from Eqs. 2.49 and 2.50:

$$\frac{E}{\kappa} \to \frac{E_R}{\kappa_R} = \left(\frac{l_{th}}{l}\right)^{-2\eta}\left(\frac{l}{l_{th}}\right)^{-2-\eta}\frac{E}{\kappa} \approx 10^{-6}\frac{E}{\kappa}. \tag{2.62}$$

By substituting $\frac{E_R}{\kappa_R}$ into Eq. 2.61, allows us to include the effect of renormalization in our estimate. Now the relative magnitude of stretching and bending energies per unit area is:

$$\frac{U_s}{U_b} = \frac{E_R}{\kappa_R}\varepsilon^2 R^2 \approx 10^3. \tag{2.63}$$

This confirms that the stretching energy contribution is larger by a factor of 10^3 and therefore bending rigidity can still be neglected.

2.3 Summary

In summary, graphene is the thinnest possible crumpled membrane. From the view of continuum elastic theory, the mechanical response of flat graphene is characterized by three elastic constants: Young's modulus ($E = 1$ TPa), Poisson's ratio ($\nu = 0.165$), and bending rigidity ($\kappa = 1$ eV). Related experimentally relevant parameters such as the 2D Young's modulus or in-plane stiffness $E_{2D} = Et \approx 340$ N/m, and biaxial modulus $\widetilde{E}_{2D} = \frac{E_{2D}}{(1-\nu)} \approx 400$ N/m are also used, since the thickness of an atomic layer (t) and ν are not well known for monolayer graphene. However, graphene is always crumpled and such crumpling renormalizes these constants. For a graphene sample with size L and crumpling amplitude δ, the Young's modulus is predicted to decrease ($E_{2D} \propto \frac{1}{\delta}$, $E_{2D} \propto L^{-0.4}$) whereas the bending rigidity is predicted to increase ($\kappa \propto \delta$, $\kappa \propto L^{0.8}$). We also show the effective or renormalized in-plane stiffness can be extracted by using simple geometrical relationships and known applied pressures, avoiding complicated force-deflection models in circular membranes.

CHAPTER 3

RENORMALIZATION OF IN-PLANE STIFFNESS

The first goal is to accurately probe the mechanical response of graphene drums characterized by in-plane stiffness E_{2D}. For that, we developed a new bulge test technique using electrostatics to apply a low and uniform pressure, and interferometry to measure graphene's deflection. Our results show that E_{2D} is reduced by up to 10 times from its standard value in flat graphene, $E_{2D} = 340$ N/m, due to crumpling. Specifically, we show that the origin of crumpling is static wrinkles, with only a minor contribution due to flexural phonons.
Published as: Nat. Comm. 6, 8789 (2015)

3.1 Device preparation and set-up

Our experimental setup is shown in Fig. 3.1. At its heart is a suspended graphene membrane that is actuated by applying an electrical bias between it and a silicon 'gating chip' underneath and whose deflection is monitored via interferometric profilometry.

The main sample chip is a silicon based die with suspended silicon nitride (SiN_x) windows with pre-patterned holes of diameters ranging between 7.5 μm and 30 μm onto which graphene is transferred by the wet transfer of graphene grown via chemical vapor deposition (CVD) with subsequent thermal annealing as described in Appendix A. The SiN_x used was very thick (~ 1 μm) to minimize deformation under load since windows less than 300 nm thick were seen to bend severely and eventually fracture. The sample chip is placed onto the gating chip consisting of degenerately doped silicon coated with 2 μm of SiO_2. To provide additional electrical insulation, a 7.5 μm thick Kapton film with a hole punched in the center is inserted between sample and gating chips. The kapton was laterally larger than the size of the chips to prevent electrical arcing around the edges when using high voltages. The entire structure is then mechanically clamped as shown in Fig. 3.1, resulting in an average separation of 15 μm between the graphene and the gating chip. Finally, separate electrical contacts are made to the graphene and the gating chip. The entire device structure is placed inside an optical cryostat (Janis ST-500) in vacuum better than 10^{-5} Torr at temperatures between 4 K and 400 K.

Close inspection of our freestanding samples reveal static wrinkles with wavelength ~ 50 nm and average amplitude ~ 1 nm via AFM (Fig. 3.2, left/bottom). Somewhat larger micron-scale features are seen in a minority of membranes, as shown in the SEM images (Fig. 3.2, right). Also, flexural phonons are invariably present in graphene at room temperature.

Graphene was electrostatically pressured by applying a voltage V_g between the graphene and the gating

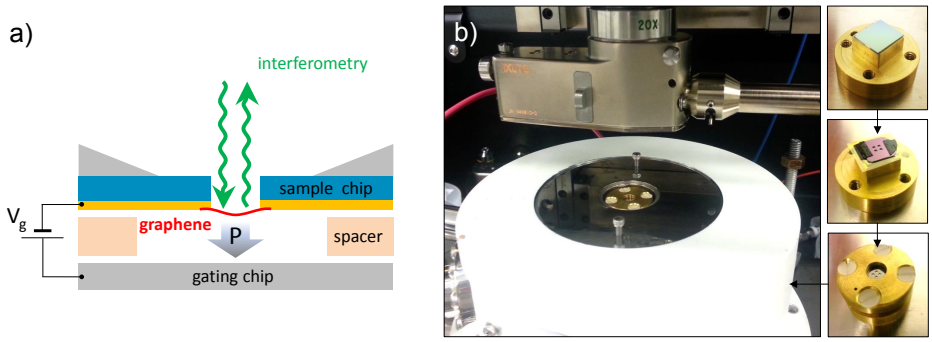

Figure 3.1: Electrostatic bulge test experimental setup. a) Schematic of device consisting of the gating chip, insulating kapton spacer, and the sample chip. The sample chip holds graphene whose deflection under gate voltage V_g is measured via interferometric profilometry. b) Photographs of device and experimental setup. Main panel, shows device within a Janis ST-500 optical cryostat to be measured via the Veeco Wyko 9800 NT $20\times$ through-transmissive media interferometric objective. Right, shows how the device stack is mechanically clamped between two brass plates with insulting screws.

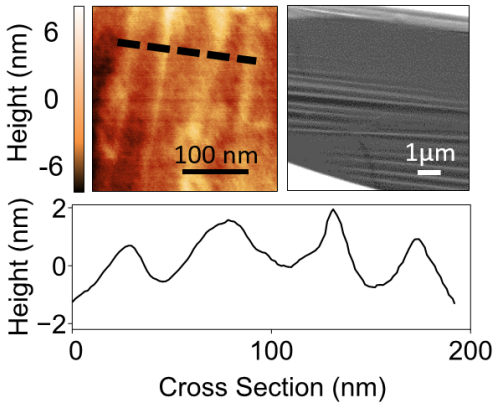

Figure 3.2: AFM measurements of graphene membrane showing nanometre-scale static wrinkles (left, scale bar, 100nm). A cross section of the AFM data are shown in the bottom panel. Wrinkling is also evident on the high-angle tilted SEM image (right, scale bar, 1 μm).

chip. The pressure applied to graphene can be evaluated as:

$$P = \frac{\epsilon_0}{2}\left(\frac{\epsilon_r}{\epsilon_r d + d_{oxide}}\right)^2 V_g^2 \approx \frac{\epsilon_0 V_g^2}{2d^2} \tag{3.1}$$

where ϵ_0 is the vacuum permittivity, ϵ_r is the relative permittivity of SiO_2, and d is the separation between graphene and gate as determined by interferometric profilometry (discussed below), and d_{oxide} is the thickness of the SiO_2. Even though we use very thick oxides, $d_{oxide} \sim 2$ μm, to prevent dielectric breakdown. The presence of oxide does not influence gating since $\epsilon_r d \gg d_{oxide}$. Additionally, the applicability of parallel-plate capacitor approximation is justified since $d \sim 10 - 20$ μm is much larger compared to the maximum deflection of graphene ($\sim$ 600 nm). The maximum V_g that can be applied without dielectric breakdown is ~ 2000 V, which allowed us to reach maximum pressures around 30 KPa. The uncertainty in P is below 5% for all voltages.

3.2 Interferometric profilometry

A legacy Veeco Wyko 9800 NT wide-field interferometric profilometer offered a non-invasive method to probe the topography of graphene membranes. A schematic of the setup is shown in Fig. 3.3. The sample rests within a cryostat, on a 5-axis stage suspended on an air table to isolate the sample from vibrations. The deflection of graphene is probed via phase shift interferometry (PSI) using a 530 nm high brightness (HB) LED. This allowed the direct measurement of the graphene surface $h(x, y)$ with sub-nanometer precision in the out-of-plane direction and sub-micron resolution in the in-plane direction (e.g. Fig. 3.4a and Fig. 4.2).

The light in the interferometer is split into two arms. The measurement arm illuminates the sample. The reference arm is calibrated to match the working distance of the measurement arm. Variations in sample height changes the path length of light travelling through the measurement arm. Then, the light from both paths is combined. Modulation in the light intensity allows detection of phase difference. Since the wavelength of light is known, this phase difference can be converted to a length travelled by the light. When the sample is in a cryostat there is an additional optical element that the light transverses (quartz cryostat window). The through-transmissive media lens includes an identical compensating piece of quartz in a Michelson interferometer geometry (perpendicular arms). This ensures that no spurious phase shifts occur due to differences in the arms other than topography changes. When samples are not inside a cryostat this special lens and compensating quartz is not needed (e.g. chapter 4). There, the lenses have a Mirau interferometer geometry (coaxial arms, not pictured). A separate measurement is performed to find gate distance d by deliberately sweeping the focus from the sample to gating chip using white light in vertical scanning interferometry (VSI) mode (Fig. 3.4b). In VSI mode, the sample stage is moved with motors to determine topography, rather

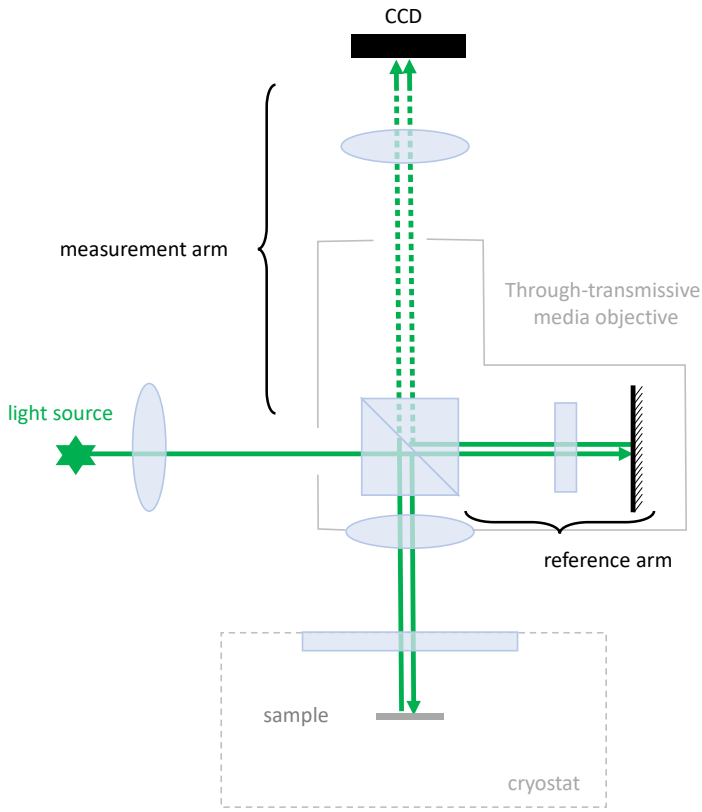

Figure 3.3: Schematic of the Veeco Wyko interferometric profilometer. A 530 nm light source is split between two arms: the reference and measurement arms. These arms are calibrated to have identical optical paths. Within the 'through-transmissive media' objective there is a compensating quartz window to account for the cryostat window which sits in the measurement arms' optical path. The light is then combined and viewed on a CCD. Variations in sample height causes a phase difference between the arms, indicated by bright and dark fringes on the CCD. The distance between these fringes are used to calibrate sample deflection in nanometers.

than detecting path differences of the light. We use a wide field interferometer for all interferometry measurements. Wide-field means interferometric data from the entire image plane is collected without the need for laborious raster scanning. This offers a significant advantage compared to confocal interferometry which only collects data at a single point. One limitation of this method is that sample deflections beyond 10° from horizontal cannot be detected since since light is reflected outside the range of the lens. This limits the applicability of this method for measurements of graphene cantilevers (see chapter 5).

The main goal of the topography measurement is to determine the center-point deflection of the membrane h. This can be achieved in two ways. The first is directly taking the difference $h = h(x_{center}, y_{center}) - h(x_{edge}, y_{edge})$. The second is fitting multiple membrane cross-sections to circles $h = \frac{a^2}{2R}$ (valid for $h \ll a$, see chapter 2) and averaging. Both methods are valid, however the former should be used with care. The underlying assumption of the measurement is that all phase shifts come from topography changes. This is

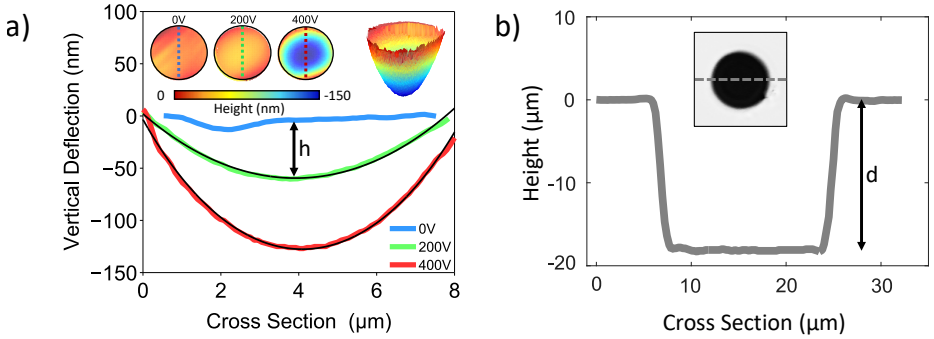

Figure 3.4: a) Cross-sections of a graphene membrane at various applied voltages. Height data obtained from phase shift interferometric profilometry (PSI mode) corresponding to these cross-sections are shown in the inset. Also shown is a three-dimensional view of the data at $V_g = 400$ V. b) Gate distance determined from interferometric profilometry (VSI mode). In this case the gate distance is $d = 18$ μm

not true. Since the refractive index of graphene and SiN_x are different, there can be an arbitrary phase jump from the reflection of either surface. Therefore checking consistency between both measurements methods gives the most accurate data. This is another example of the advantage of using a wide-field interferometer, both methods are available to cross-check our results and we do not only rely on phase shifts from a single point.

It is interesting to consider how it is possible to see a single atomic layer optically. High contrast optical microscopy allowing identification of single layer graphene is typically achieved through a Fabry-Perot cavity geometry. Most often, graphene is deposited on a silicon substrate with 300 nm of SiO_2. The silicon acts as a high reflectance mirror and the graphene acts as the lossy mirror resulting in a increase of signal intensity contrast by 15 % relative to the signal intensity when no graphene is present [89]. Other researchers have exploited this as an optical measurement technique for graphene NEMS on silicon [90, 91]. There, graphene under the influence of external forces acts as a movable mirror which changes the cavity resonance condition. This modulates the intensity of the signal, identical to the function of the interferometer described above. Subsequently this allows the extraction of the distance between graphene and the fixed mirror.

In our experimental setup we do not exploit cavity resonances, but instead look directly at the reflection from the graphene surface. We ensure a large gate distance so that the gating chip is completely out of focus to reduce unwanted signal. For gate distances < 2 μm we found that the reflection from the gating chip obscures the measurement of graphene. In general the reflection signal from graphene is weak. Below we estimate the magnitude of that signal and ensure that it is measurable. We consider the reflection (R) and transmission (T) coefficients of graphene as follows: $R \approx \frac{(\pi\alpha)^2}{4} = 0.013$ % and $T \approx 1 - \pi\alpha = 2.3$ % [92] where $\alpha = \frac{1}{137}$ is the fine structure constant. The field of view of the 640×480 CCD array translates to an on sample area of $\sim 62 \times 46$ μm^2 for the $50\times$ objective. Lets assume this entire area is occupied by

suspended graphene. The intensity of the 530 nm HB-LED is at least ~ 10 W/m^2. The reflected power using the estimate for graphene above is $P_{reflected} \geq 4 \times 10^{-13}$ W. Using $E = \frac{hc}{\lambda}$, this is $\geq 1 \times 10^7$ photons per second. The absolute sensitivity threshold for a typical CCD sensor requires $10 - 50$ electrons per pixel to beat the noise in the detector. The electrons per pixel from my estimate is at least $\frac{1}{2}\frac{1\times10^7}{640\times480} \approx 15$ assuming a typical quantum efficiency of $50\ \%$. This means for pristine graphene and a typical CCD sensor, detection via reflection from the graphene surface is possible, especially with an integration time of a few seconds. Realistically, the reflection from graphene may actually be many times larger due to surface contaminants.

3.3 Mechanics at room temperature

The in-plane stiffness of graphene at room temperature is extracted from measured membrane profiles $h(x, y)$ vs. known applied pressure P. We determined the biaxial in-plane stress σ and biaxial strain ε from the equations derived in chapter 2:

$$\sigma = \frac{Pa^2}{4h}, \tag{3.2}$$

$$\varepsilon = \frac{2h^2}{3a^2}, \tag{3.3}$$

where a is the radius of a graphene membrane, and h is its center-point deflection determined by fitting many cross sections to a circle and averaging (e.g. Fig.3.4a). We note the stress σ is the total stress that includes both the built-in (existing without the application of pressure) and applied (due to applied pressure) stress components. Consequently, $\sigma = 0$ means the membrane is completely relaxed. We call the strain determined from interferometry ε_I in later chapters to distinguish it from other extraction methods (e.g. Raman spectroscopy in chapter 4). Since ε is measured geometrically relative to the initial state at $P = 0$, it does not include the built-in strain (ε_0) component. In the majority of measured devices we observe a linear relationship between ε and σ (Fig. 3.5a), allowing us to determine the in-plane stiffness of graphene. It is given by $E_{2D} = (1 - \nu)\frac{\sigma}{\varepsilon}$, where we use the Poissons ratio for flat graphene $\nu \sim 0.165$. This is only an approximation since the the value of flat graphene likely doesn't apply here. In chapter 4, where crumpling strength is changed, we do not make this assumption.

While in realistic devices both strain and stress vary slightly throughout the device, our finite element modeling in chapter 2 confirms that the exact numerical solution for E_{2D} does not deviate more than 10% from the simple analytical estimates [76]. This is within the uncertainty of extracting E_{2D} from our data. We also note that the obtained E_{2D} agrees with the value obtained by fitting $P(h)$ data to the bulge-test equation (Fig. 3.5a, Inset). In all 26 measured monolayer CVD graphene membranes (Fig. 3.5b) we find $E_{2D} = 35 \pm 29$ N/m, consistent with previous work [57].

Our method of probing the mechanical properties of graphene has several critical advantages over AFM-

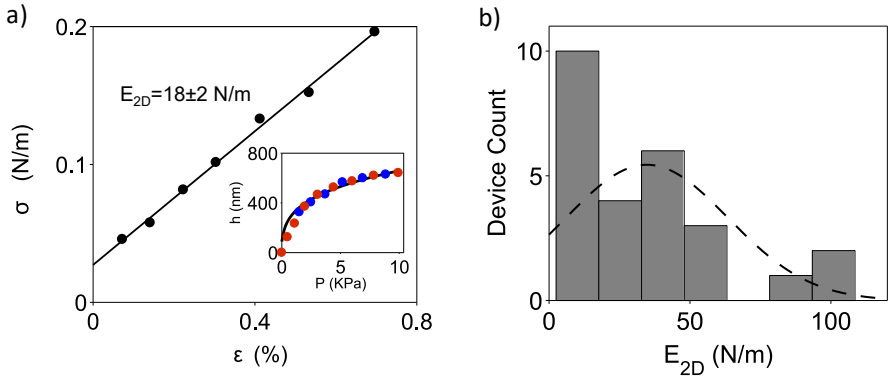

Figure 3.5: a) Stress (ε) vs. strain (σ) dependence for a typical device. The in-plane stiffness E_{2D} is extracted from the slope of linear fit to these data (black line). Inset a) shows raw center-point deflection, h, vs. pressure, P, data used for calculation of stress and strain (red: loading cycle, blue: unloading cycle) b) Histogram of E_{2D} for all measured CVD graphene devices

based nanoidentation and other techniques. First, graphene deflection is measured via a non-contact approach. This means that the membrane morphology is not disturbed with a sharp tip that applies non-uniform stress. Second, the height data from the entire membrane is recorded at the same time. This means we can find the true maximum center point deflection, h, and verify that the membrane is deflecting symmetrically. Third, the pressure is applied uniformly, allowing us to use simple and reliable models to extract mechanical constants. Fourth, the optical nature of the technique allows simple characterization of devices inside an optical cryostat at low temperatures. A limitation of the method is that it cannot be used to measure breaking strength.

We performed numerous consistency checks to rule out possible measurement artifacts. First, we observed no hysteresis in $P(h)$ data between loading and unloading cycles (Fig. 3.5a, Inset). This establishes that graphene is not slipping against the substrate. Second, we observed similarly soft E_{2D} for CVD graphene (Fig. 2b; grain size ~ 50 μm, bigger than the membrane size) and exfoliated graphene ($E_{2D} \sim 50 - 80$ N/m in two devices). This confirms that E_{2D} in our experiments is not affected by the grain boundaries in graphene, consistent with conclusions from previous experiments [93]. Third, we cross-checked our results against the measurements obtained via AFM nanoindentation. In the regime of low loading forces < 300 nN, nanoindentation measurements on the same devices yielded E_{2D} consistent with optical profilometry measurements. It is important to note that AFM nanoindentation pushes graphene towards the substrate, while electrostatic loading pulls graphene away from it. Similarity in E_{2D} values obtained for opposite loading directions confirms that interaction of graphene with the sidewalls does not affect the measured E_{2D}. Finally, simple estimates show that the organic residues that may remain on graphene after the fabrication process [94] are unlikely to affect E_{2D}. A uniform residue layer with Youngs modulus of ~ 2 GPa [95] and thickness < 5 nm is expected to be at least 100 times softer compared to graphene. However, it is still possible that residues

contribute to crumpling to begin with.

In a few devices we observed pronounced nonlinear dependence of $\sigma(\varepsilon)$, with $E_{2D} = (1-\nu)\frac{d\sigma}{d\varepsilon}$ increasing from less than 10 N/m at low stress to 50 N/m at higher stress (Fig. 3.6). This nonlinearity is investigated in chapter 4. In that chapter, we measure identical devices at higher stress and retrieve $E_{2D} = 340$ N/m. This offers a final consistency check that our mechanics measurement is artifact free — and the low stress softening is physical. We hypothesize that this softening is due to crumpling from static wrinkling or flexural phonons.

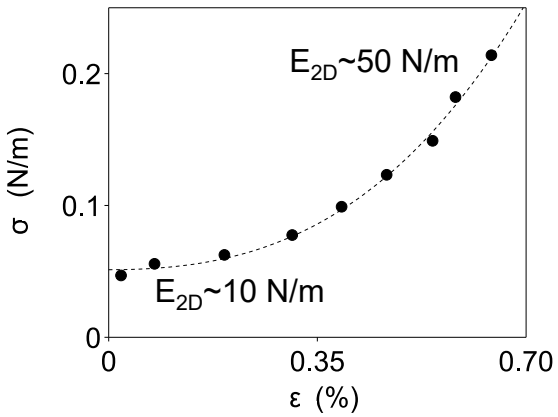

Figure 3.6: A nonlinear stress-strain curve seen in a minority of devices. Stiffness increases from ~ 10 N/m at low stress to ~ 50 N/m at higher stress. The dashed line is a guide to the eye. We hypothesize that this is due to changing the amount of crumpling present in the membrane as a function of strain. This is investigated in more detail in chapter 4.

3.4 Probing contribution due to flexural phonons

To study the effect of flexural phonons, we examined changes of graphenes E_{2D} with temperature. Since the amplitude of flexural phonons causing crumpling scales with temperature T as k_BT (k_B is the Boltzmann constant), we would expect strong stiffening of graphene at low temperature if this were the dominant effect. We measured two different devices in the range of temperatures between 400 K and 10 K (Fig. 3.7). While we observed moderate stiffening of graphene from $E_{2D} \sim 20$ N/m at 300 K to $E_{2D} \sim 85$ N/m at 10 K, all of the measured devices are much softer compared to 340 N/m throughout the range of temperatures. This suggests that the contribution due to flexural phonons does not dominate the mechanics of graphene at room temperature.

We note that it is tempting to interpret the stiffening of graphene at low temperature seen in Fig. 3.7 as a signature of the temperature-dependent suppression of crumpling due to flexural phonons. Indeed, the data in Fig. 3.7 can be fit to an expression describing the contribution of flexural phonons to in-plane stiffness. That

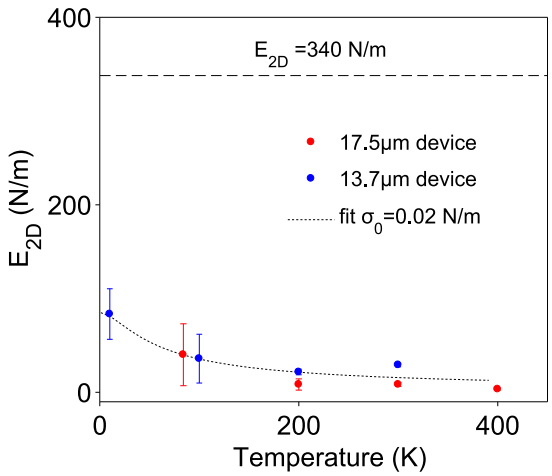

Figure 3.7: The in-plane stiffness E_{2D} measured for two circular membranes (diameters 17.5 μm and 13.7 μm) as a function of temperature. The dotted line is fit to an analytical model which includes the effect of crumpling from flexural phonons (Eqs. 3.4 and 3.5). The dashed line shows the stiffness of a flat graphene, $E_{2D} = 340$ N/m. The error bars are obtained by estimating the standard deviation of E_{2D} measurements.

expression was derived in chapter 2:

$$\varepsilon = \frac{1}{2}\frac{\Delta A}{A} + \frac{\sigma}{E_{2D}^0} \tag{3.4}$$

$$\frac{\Delta A}{A} = -\frac{1}{2\pi}\int_{q_{min}}^{q_{max}} \frac{k_B T}{(q^2\kappa(q) + \sigma)} q dq \tag{3.5}$$

For a realistic value of built-in stress $\sigma_0 = 0.02$ N/m, the model fits our data well as shown by the dotted line in Fig. 3.7. However, since the contribution due to static wrinkling may also be temperature dependent, this agreement may be accidental.

3.5 Probing contribution due to static wrinkles

To isolate the contribution due to static wrinkles, we analyzed changes in E_{2D} of patterned graphene membranes. In general, there is a concentration of stress along the wrinkles in a crumpled sheet called a 'tension ray' [96, 97]. The stress can be relieved by cutting the membrane across such wrinkles. The reduction in stress, in turn, leads to a decrease in wrinkle amplitudes. In particular, for very narrow ribbons we expect fully suppressed wrinkles.

Experimentally, our suspended graphene devices were cut using focused ion beam (FIB) lithography. The FIB beam was rastered to carve thinner and thinner ribbons out of the same, initially circular graphene membrane. The FIB lithography was carried out using a Novalab 600 Dual-Beam (electron/ion) FEI. The

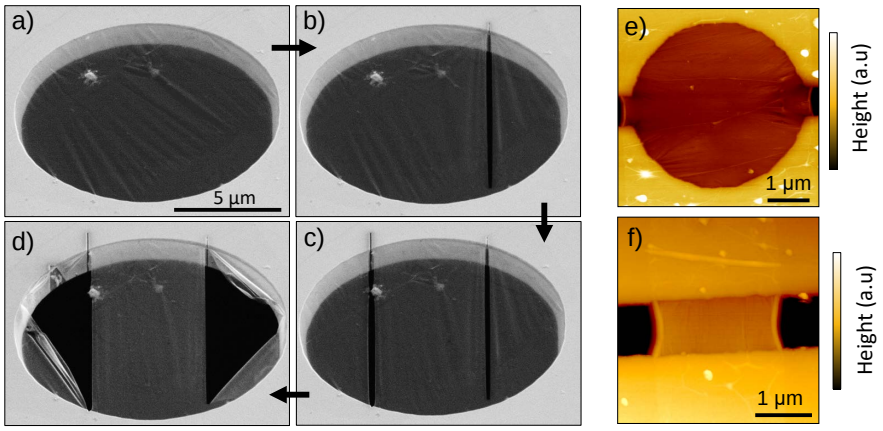

Figure 3.8: Crumpling in graphene membranes and ribbons. a-d) Evolution of the topography of a wrinkled device as viewed by SEM during FIB cutting. e-f) As fabricated circular membrane and ribbon without the use of FIB. The ribbon shows less wrinkling overall than a similarly sized circular membrane.

system is aligned to the graphene with the electron beam (5 KeV, 0.4 nA) while cuts are made with Ga+ ion beam (30 KeV, 50 pA current, exposure time $<$ 500 ms). Using SEM we confirmed that the process of cutting reorients wrinkles along the cut direction and suppresses their amplitude. The progression of cutting and corresponding changes in the wrinkling are seen in Fig. 3.8a-d. Additionally, Fig. 3.8b shows as-fabricated circular membranes and ribbons without the use of FIB cutting. Since stress and strain from fabrication in ribbons is mostly uniaxial, there is less wrinkling compared to the circular device.

The initial circular membrane with diameter 12.5 μm was first cut into a ribbon with width of $w = 5$ μm. Then width of this ribbon was then reduced to $w = 2.7$ μm. This progression is shown in the three panels at the bottom of Fig. 3.9a. We extracted the effective mechanical constants of such devices by measuring their deflection vs. applied electrostatic force, similar to the analysis above. For near-rectangular ribbons uniaxial stress is extracted as:

$$\sigma = \frac{Pa^2}{2h} \tag{3.6}$$

Since the derivation of Eq. 3.3 considered changes in arc lengths (see chapter 2), it is valid to use it here for uniaxial strain in ribbons. The in-plane stiffness was then computed as: $E_{2D} = \frac{\sigma}{\varepsilon}$. We observed that the devices stiffen with each subsequent cut (Fig. 3.9a). The in-plane stiffness increased from $E_{2D} = 36$ N/m

for initial circular membrane to 138 N/m for 5 μm wide ribbon, and to 300 N/m for 2.7 μm wide ribbon. The in-plane stiffness of flat graphene, 340 N/m, is within the uncertainty of the last value.

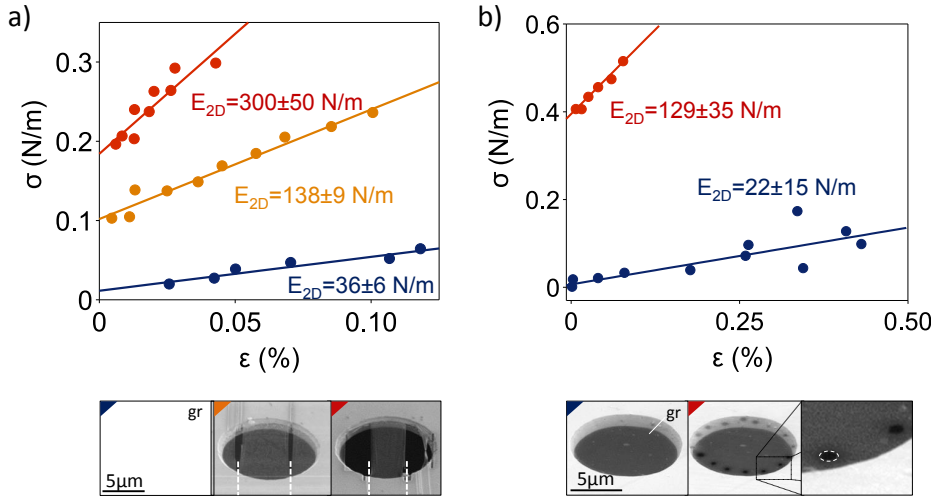

Figure 3.9: Probing wrinkle contribution to mechanics. a) Stress (σ) vs. strain (ε) curves for a single graphene device as its aspect ratio is changed via FIB lithography. SEM images of the device at each step of cutting are shown in bottom panels (cut directions are white dashed lines). b) Stress-strain curves for another device as it is perforated near the edge of the membrane. SEM image of the device before and after perforations is shown in bottom panels.

We also explored an alternative approach to relieve crumpling of graphene by puncturing a series of $\sim$ 100 nm diameter holes near the edge of the membrane using FIB. Similarly, we observe a significant increase in the measured in-plane stiffness after perforations (Fig. 3.9b). Overall, we see that once crumpling associated with static wrinkles is relieved, the stiffness of graphene increases to almost 340 N/m. This further suggests that static wrinkles have the dominant contribution to softening of the effective in-plane stiffness of circular graphene membranes.

3.6 Probing contribution due to defects

Normally, the presence of defects lowers the mechanical stiffness of any material. This has also been shown to be true for graphene [98]. However, it has been reported that under certain conditions vacancy type defects at sufficient density can lead to mechanical stiffening of graphene above 340 N/m [68]. The authors of Ref. [68] claim that defects suppress flexural phonons by scattering them. The underlying assumption of that work is that the accepted value of graphene stiffness, 340 N/m, contains the contribution due to flexural phonons. Later work found that the defects actually induce high strain in their vicinity which in turn is expected to suppress the flexural phonons. Additionally, defects are a source of disorder which may lead to static crumpling in addition to suppressing flexural phonons [99]. At the same time, Ref. [68] and subsequent works use AFM nanoindentation to extract stiffness. Recent work [100] has suggested that the typical models

for the AFM indentation used are not sufficiently accurate to extract the mechanical constants of crumpled membranes. Because of this, the effect of defects on the mechanical response of 2D membranes remain a subject of debate within the literature.

To confirm that the stiffening seen in Fig. 3.9 stems from changes in devices geometry rather than from the induction of defects in graphene that can occur during FIB cutting, we performed an additional experiment to study E_{2D} vs. defect density. We started by ensuring that FIB cutting indeed induced defects. Raman spectroscopy confirms that FIB cutting induces defects in the remaining membrane (Fig. 3.10). The spectra was taken $\sim$ 1 μm away from a single typical FIB cut in an originally pristine graphene membrane. The additional Raman features: D peak at $\sim$ 1400 cm^{-1} and weaker D' above $\sim$ 1500 cm^{-1}, indicate the presence of defects. For a pristine membrane, only the G and $2D$ Raman peaks are seen.

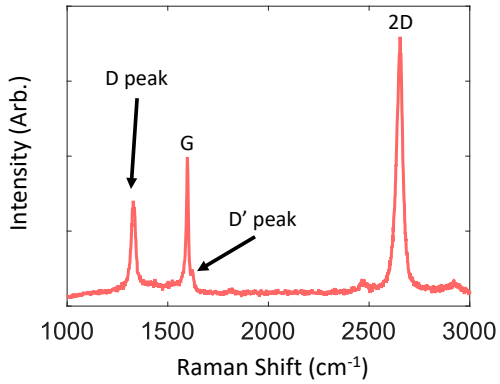

Figure 3.10: Example Raman spectra of graphene $\sim$ 1 μm away from a typical FIB milled cut. The presence of the D and D' peaks indicates a large number of defects. From this data, following the analysis described in the main text, we deduce that a single cut induces $\leq 5 \times 10^{12}$ cm^{-2} of defects.

To controllably introduce defects, we placed our membranes into an FIB chamber and rastered a 5 keV beam of Ga+ ions (29 pA) over an area larger than our samples (100×100 μm^2). Typical exposure times between 0 and 30 s translates into ion doses between 0 and 5×10^{13} cm^{-2}. We took devices devices through several successive steps of irradiation gradually increasing the doses 0 to $\sim 5 \times 10^{13}$ cm^{-2}.

To determine the concentration and type of defects upon irradiation, we collected Raman spectra of our devices following the exposure. Example spectra are shown in Fig.3.11a where each spectrum is offset for clarity. The increase in the intensity of the Raman D peak indicates creation of defects. To determine the defect type, we monitored the ratio between D and D' peaks and determined $\frac{I(D)}{I(D')} \sim 6 \pm 1$ on average across all our samples. This is very close to $\frac{I(D)}{I(D')} = 7$ expected for vacancy-type defects [101]. To quantitatively determine the defect concentration, we analyzed the ratio between the D and G Raman peaks using Eq. 3.7

[102]:

$$\frac{I_D}{I_G} = C_A \frac{\left(r_A^2 - r_s^2\right)}{\left(r_A^2 - 2r_s^2\right)} \left[e^{-\pi r_s^2/L_D^2} - e^{-\pi(r_A^2 - r_s^2)/L_D^2}\right] \tag{3.7}$$

where length scales of scattering $r_s = 1$ nm, $r_A = 3.1$ nm, and $C_A = AE_L^{-B}$ with $A = 160$ eV^4, $B = 4$, and $E_L = 1.96$ eV (for 633 nm excitation), and L_D is the distance between defects. Defect density is then finally evaluated as $\frac{1}{L_D^2}$ cm^{-2}.

Defect density obtained from Eq. 3.7 is plotted vs. the density of impinging ions in Fig. 3.11b. A linear fit to this data, with slope ~ 0.9, suggests that Ga+ ions produce vacancy-type defects in graphene with 90% probability, as expected [103]. The same analysis applied to the spectra in Fig. 3.10 suggests that each cut when forming ribbons induces defects with density $\leq 5 \times 10^{12}$ cm^{-2}. To carve a pristine membrane into multiple thinner ribbons (such as Fig. 3.9a) takes at least 4 cuts. This means that the defect density range we study is sufficient to determine whether or not the reduced in-plane stiffness we measured previously is due to defects.

We examined the evolution of the in-plane stiffness E_{2D} (measured at room temperature, following Ga+ irradiation) vs. defect concentration (as determined from Raman spectra). The data shown in Fig. 3.11c were collected from 14 different devices at room temperature. Two distinct representative devices are shown as red and blue points respectively, the data from the other devices are gray. The inset of Fig. 3.11c shows a zoomed-in region of low defect densities. Every device remained softer than 340 N/m in the entire range of induced defect concentrations. The in-plane stiffness did not appear to be strongly affected by the presence of defects, apart from small changes that could be ascribed to variation in experimental conditions. This confirms that the changes in stiffness observed in Fig. 3.9 can only be caused by changes in devices geometry. This is also further evidence that the stiffness of the membrane is dominated by another effect such as wrinkling.

It is interesting to note that after FIB exposure, the membranes in Fig. 3.9 show higher built-in stress, as indicated by the increased y-intercept. In all our devices we saw no correlation between built-in stress and in-plane stiffness in accordance with other work [68]. Specifically, even if defects do increase built-in stress, our defect analysis previously show there is no correlation between in-plane stiffness and defect density.

3.7 Competition of crumpling mechanisms

It is instructive to estimate relative contributions for flexural phonons and static wrinkling to the in-plane stiffness of our devices. The in-plane stiffness of graphene E_{2D} measured in the experiment can be loosely approximated as:

$$E_{2D}^{-1} = E_{latt}^{-1} + E_{flex}^{-1} + E_{wrin}^{-1} \tag{3.8}$$

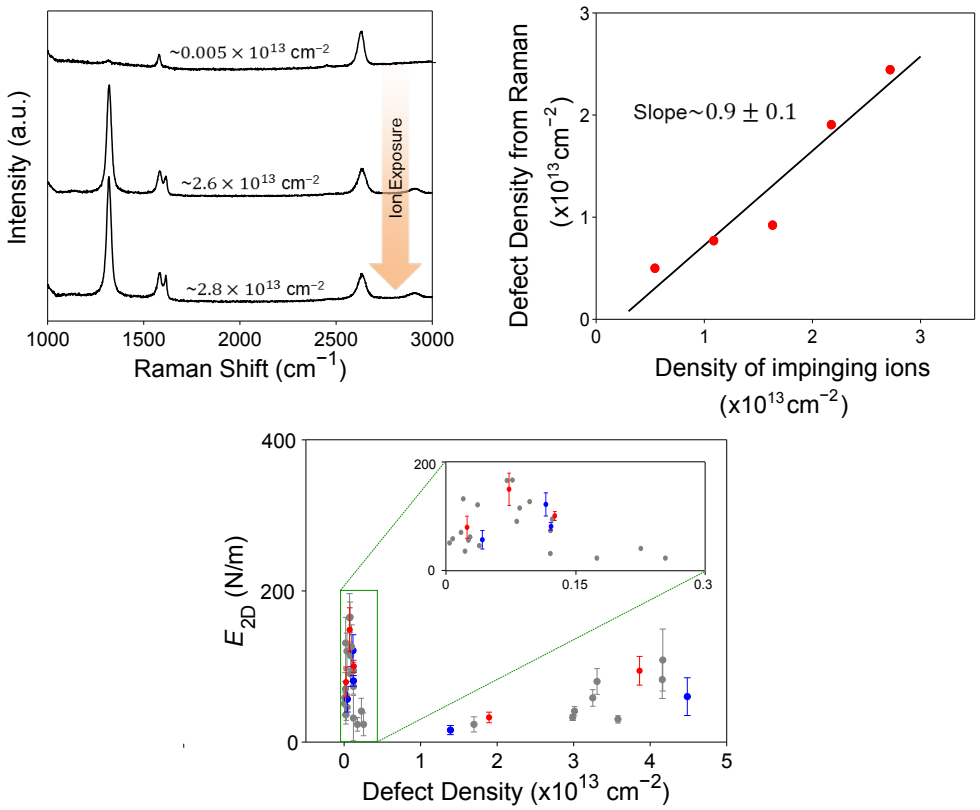

Figure 3.11: Confirming that stiffness is not affected by defects in crumpled graphene. a) Evolution of Raman spectra following ion beam exposure. b) To control the amount of defects we induce into graphene we calibrate the amount of defects we induce by the impinging ions dose. The linear fit to induced defect density vs. impinging ions shows that 90 % of impinging ions create a vacancy type defects. c) E_{2D} vs. defect density. Inset: close-up view close to zero defect density. We conclude that defects in this density range do not affect the mechanical response of crumpled graphene.

where $E_{latt} \sim 340$ N/m, E_{flex} and E_{wrin} are contributions to stiffness from three different mechanisms: stretching of carbon-carbon bonds, flexural phonons, and static wrinkles. The data in Fig. 3.9a suggests that suppression of the contribution due to wrinkling increases E_{2D} from 36 N/m to 300 N/m. Provided that the width of graphene ribbon is much larger compared to the typical wavelength of a flexural phonons, $\sim 10-1000$ nm, we expect that the process of cutting does not affect the contribution due to flexural phonons. Therefore, we can use Eq. 3.8 to estimate $E_{wrin} < 40$ N/m and $E_{flex} > 2500$ N/m from this data. We see, in agreement with our earlier conclusion, that the contribution due to wrinkles dominates E_{2D}.

A simple estimate can clarify why the contribution due to static wrinkling is larger than that of flexural phonons. The degree of crumpling of a membrane can be quantified as $\frac{\Delta A_0}{A} = \frac{A'-A_0}{A}$, where A is the area of the flat membrane and ΔA_0 is the hidden area as discussed in chapter 2. Stretching caused by an external stress gradually flattens the membrane. When stress is large enough to suppress crumpling and flatten the

membrane, the projected area is fractionally increased by $\frac{\Delta A_0}{A}$. This corresponds to a fractional increase $\varepsilon_t = \frac{\Delta A_0}{2A}$ in the linear dimensions of the membrane. We therefore conclude that when graphene is extended less than this threshold strain ε_t, it is mostly crumpled and should appear soft, while at strains above ε_t it is mostly flat and should have in-plane stiffness close to $E_{2D} \sim 340$ N/m. This is in agreement with the FEM in chapter 2. The degree of crumpling of graphene due to flexural phonons can be estimated using Eq. 3.5: $\left(\frac{\Delta A_0}{A}\right)_{flex} \approx 0.5\%$. This estimate agrees with $\frac{\Delta A_0}{A}$ extracted from more detailed calculations [87]. The corresponding strain $\varepsilon = \frac{\Delta A_0}{2A} \sim 0.25\%$ is smaller than the average built-in strain for devices used in our experiments: $\varepsilon_0 = \frac{\sigma_0}{E_{2D}} \sim 0.3\%$. We therefore expect that flexural phonons are at least partially suppressed in our devices. For static wrinkling, assuming sinusoidal wrinkles with wavelength $\lambda = 50 - 100$ nm and amplitude $\delta = 1 - 2$ nm (Fig. 3.2) we estimate: $\left(\frac{\Delta A_0}{A}\right)_{wrin} \sim \pi^2 \frac{\delta^2}{\lambda^2} > 0.1 - 1.6\%$. The lower bound here is likely a very conservative estimate as it neglects wrinkles with longer wavelengths. The corresponding ε_t from this estimate is larger than the average built-in strain observed in experiment, and we therefore do expect softening of graphene due to static wrinkling. The argument above can be summarized simply. The amplitude of crumpling due to static wrinkling is higher than that due to flexural phonons. Therefore, the contribution of static wrinkling to stiffness is also larger.

3.8 Conclusion

We have developed a non-contact technique for probing the mechanical properties of graphene and potentially any conductive 2D material. The approach uses uniform loading and can operate at cryogenic to room temperatures. We have confirmed that graphene is significantly softened by out-of-plane crumpling. Moreover, we developed an approach to test relative contributions of flexural phonons and static wrinkles to the in-plane stiffness of graphene by changing the geometry in-situ, and found that the latter dominates the contribution due to flexural phonons.

CHAPTER 4

ANOMALOUS HOOKE'S LAW

In this chapter we investigate the nonlinear response of graphene membranes as they transition from the crumpled state to the flat state. This was achieved by extending the bulge test technique used in chapter 3 to accommodate higher pressures. We discover an anomalous Hooke's law behaviour in agreement with recent theory. Moreover, we introduce a method to measure the degree of crumpling called hidden area experimentally, by comparing strain extracted from two complementary techniques — interferometry and Raman spectroscopy. Finally, we confirm that strain engineering can suppress and control the degree of crumpling and therefore the mechanical response of 2D materials.

Published as: Phys. Rev. Lett. 118, 266101 (2017)

4.1 Experimental set-up

Two types of samples were produced: standard and strain-engineered. Standard samples are similar to those used in chapter 3 and consisted of a monolayer graphene membrane suspended over a single hole with diameter ~ 10 μm in a silicon nitride (SiN_x) support on a silicon chip. Strain-engineered samples are described in Appendix C.

The mechanical response of graphene membranes was characterized through measurements of sample deflection (as described in chapter 3) under a known pressure (P). Pressure was applied to graphene using compressed nitrogen gas [104]. The gas was fed into a cell that was sealed with the graphene membrane on one side. It has been shown that graphene and other 2D materials are impermeable to all standard gases, and diffusion through the substrate is only significant on the timescale of days [20]. A PDMS O-ring established a leak-tight seal between SiN_x/Si sample substrate and the cell base 4.1. A digital pressure gauge and a gas flow regulator allowed the control of pressure in increments < 1 KPa up to ~ 200 KPa, ~ 10 times larger than in our previous method in chapter 3. This is a key distinction in the methodology used in this chapter. At pressures > 200 KPa the O-ring fails. The pressure was stable to below 0.05 KPa over the length of our measurements, ~ 1 hour.

Upon application of pressure, the mechanical strain ε of the graphene membrane was measured in two different yet complementary approaches: interferometric profilometry (ε_I, as described in chapter 3) and Raman spectroscopy (ε_R, discussed below).

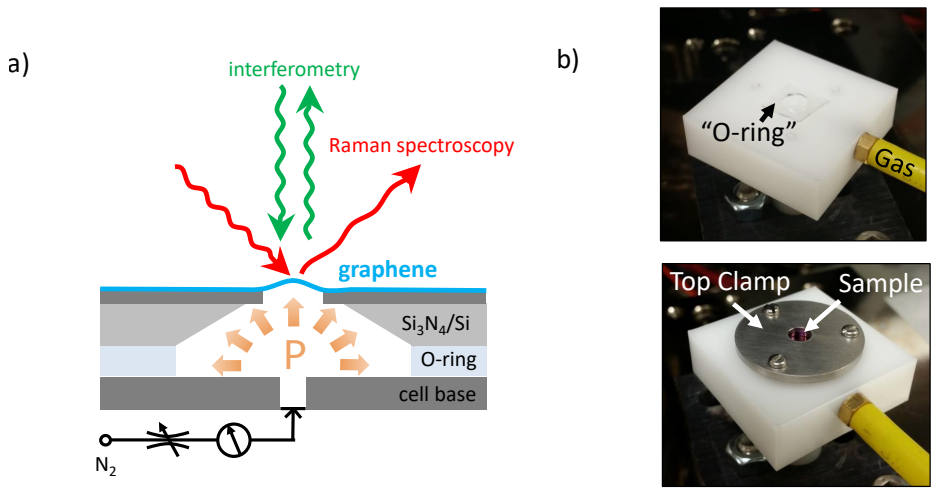

Figure 4.1: Gaseous pressure bulge test experimental setup. a) Device schematic showing the application of pressure and our two measurement techniques: interferometry and Raman spectroscopy. Depending on the orientation of the sample chip we can apply positive (away from the sample, as pictured) or negative (towards the sample) pressures. b) Photograph of pressure cell implementation with custom PDMS O-ring. The top clamp mechanically presses the sample toward the O-ring to ensure a leak-tight seal.

4.2 Strain from Raman Spectroscopy (ε_R)

In this approach, the strain was determined by monitoring the shifts of the $2D$ and G peaks in the Raman spectra of graphene as a function of applied pressure taken at the center of the membrane (e.g. Fig. 4.3a). Inaccuracy of spot position by up to 2 μm changes the results no more than 4%, see Fig. 4.3b. We use a focused 633 nm excitation source with an estimated spot size < 1 μm, resolution ~ 1 cm^{-1} and power < 1 mW to avoid heating. The strain was extracted as [22]:

$$\varepsilon_R^{2D,G} = \left(\frac{\partial \omega^{2D,G}}{\partial \varepsilon_R^{2D,G}}\right)^{-1} \left(\omega^{2D,G} - \omega_0^{2D,G}\right) \tag{4.1}$$

where $\omega^{2D,G}$ is the frequency position of the $2D(G)$ Raman peak of strained graphene, $\omega_0^{2D,G}$ is the peak position at zero strain. Since the $2D$ peak is dispersive with excitation [105] and there are very little mechanical studies using 633 nm excitation, the $2D$ Raman peak is not a reliable way to determine built-in strain. On the other hand, the G peak is not dispersive and has a very well-known position for zero strain, $\omega_0^G = 1580$ cm^{-1} [106]. However, the position of this peak is affected by doping. Neglecting that doping, we estimate a compressive built-in strain between 0.01 and 0.09 $\%$ in our samples from the data shown in Fig. 4.3. Another way to probe the built-in strain is with the lesser known $2D'$ peak. It has a similar peak sensitivity as the G peak, but is less intense. Although it is dispersive with excitation, it has the advantage of being unaffected by doping. Unfortunately there are limited studies of this peak [107], so we do not use it to probe strain. Instead, we define $\omega_0^{2D,G}$ as the position of the $2D(G)$ Raman peak at zero applied pressure. We emphasize that ε_R

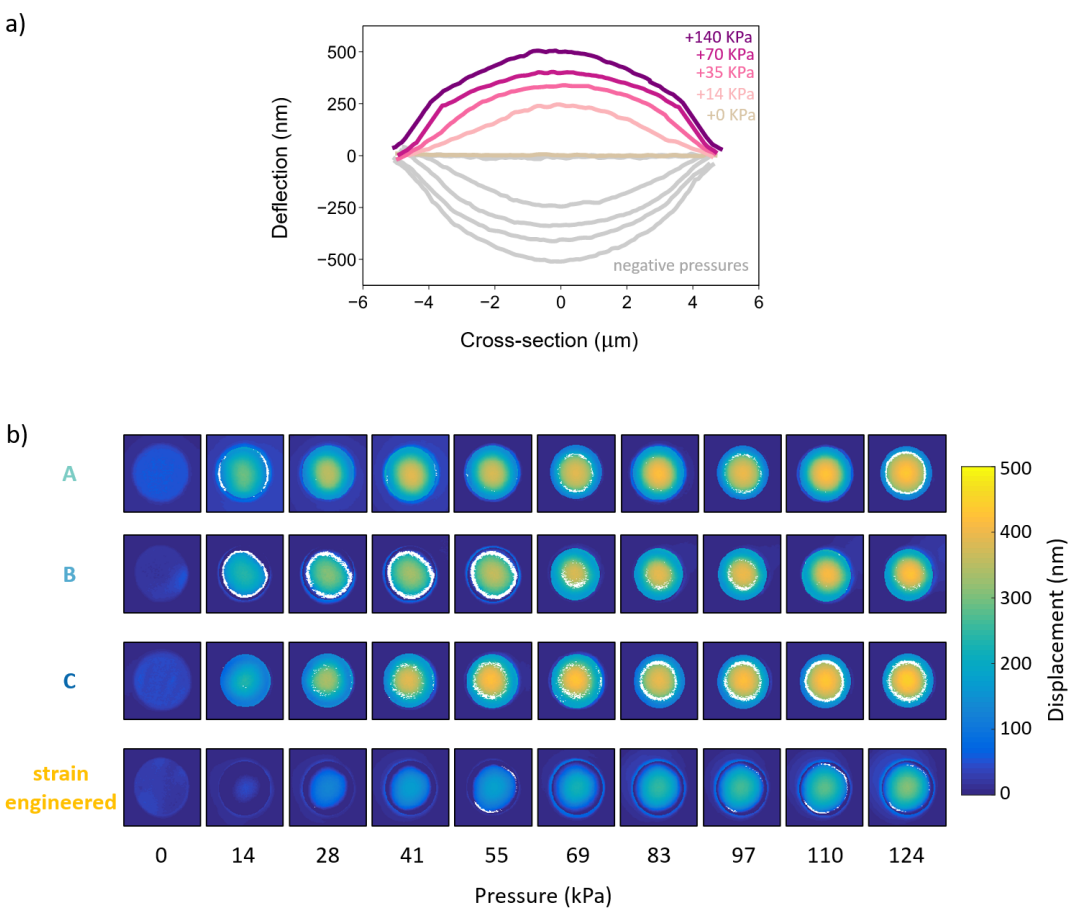

Figure 4.2: Deflection measurements with interferometric profilometry. a) Example membrane profiles for both positive and negative pressures as measured by wide-field interferometry. b) Full interferometric data for standard samples A, B, C, and a strain engineered sample at different pressures. Color is out-of-plane displacement. Missing data are labelled white.

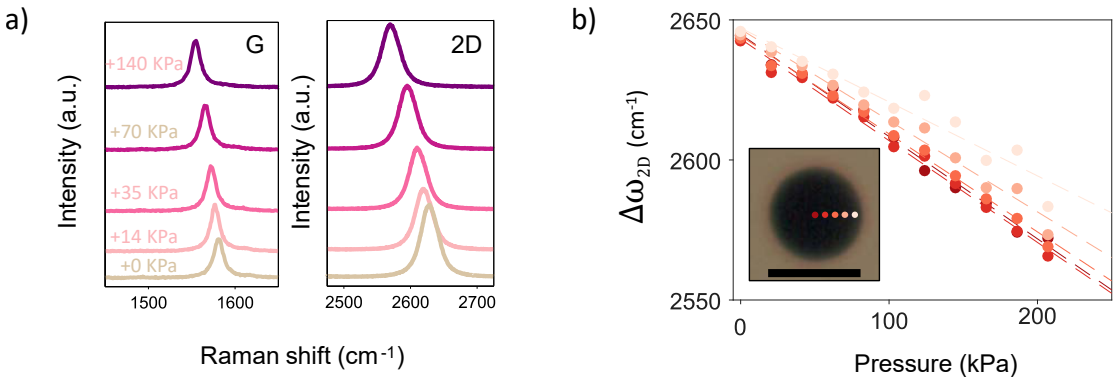

Figure 4.3: Raman spectra in strained graphene. a) Raman spectra of graphene showing the G and $2D$ Raman peaks throughout the range of applied pressure. b) Dependence of Raman spectra on spot position. Raman spectra were taken in 5 locations at 1 μm increments away from the center of a pressurized, non-strain-engineered device These positions are indicated on the photograph of the device (inset, scalebar is 10 μm). The main panel shows the resulting shifts of the $2D$ Raman peak vs. pressure, the dashed lines are linear fits to the data. The spectra show identical trends within $\sim$ 2 μm of the membrane center the slope varies no more than $\sim$ 4 %. Further away from the center, the response changes. For example, 4 μm away from the center there is a $\sim$ 30 % reduction in the magnitude of slope. This is expected: in pressurized bulge test set-up, only the center of the membrane is under perfect biaxial strain. The Raman spectra we used to extract the mechanical response is at the center of the membrane, with accuracy better than $\sim$ 2 μm.

is also a measurement of strain relative to the initial state. Then, we can compare the mechanical response as determined from both types of strain measurements.

The peak sensitivity, $\frac{\partial\omega}{\partial\varepsilon}$, for each device was found by extracting the slope of Raman peak positions vs. ε_I (Fig. 4.4a, left inset, dashed line) at stresses $>$ 1 N/m. We find peak sensitivities $\left|\frac{\partial\omega^{2D}}{\partial\varepsilon_I}\right| \sim 155 - 200\text{cm}^{-1}/\%$ and $\left|\frac{\partial\omega^{G}}{\partial\varepsilon_I}\right| \sim 55 - 90\text{cm}^{-1}/\%$ consistent with recent values in literature [108–110]. The necessity of applying such large stress is discussed later. We ensured that changes in Raman peak positions vs. pressure were entirely due to strain rather than e.g. changes in doping by observing $\frac{\partial\omega^{2D}}{\partial\omega^{G}} \sim 2.2$ (Fig, 4.4a right inset). This result is expected for strain related Raman peak shifts but not doping related shifts [106]. This also confirms identical results for extraction of strain from either G or $2D$ peaks.

4.3 Comparison of stress-strain curves from interferometry and Raman spectroscopy

The stress-strain relationships of three standard samples (A, B, and C) as measured from Raman spectroscopy, $\varepsilon_R(\sigma)$, and interferometry, $\varepsilon_I(\sigma)$, are shown in Fig. 4.4. We observe dramatic differences between the $\varepsilon_R(\sigma)$ and $\varepsilon_I(\sigma)$ curves. The $\varepsilon_R(\sigma)$ curves are linear (Fig. 4.4a). The average biaxial modulus for all devices extracted from them is $\widetilde{E}_{2D} = \frac{d\sigma}{d\varepsilon_R} = 480 \pm 10$ N/m. In contrast, the $\varepsilon_I(\sigma)$ curves are strongly nonlinear (Fig. 4.4b). In the region of low stress ($\sigma < 1$ N/m), graphene is soft, $\widetilde{E}_{2D} \sim 30 - 150$ N/m. At the same time, in the high stress region ($\sigma > 1$ N/m) we retrieve an average value of $\widetilde{E}_{2D} = 450 \pm 70$ N/m, close to what is measured by Raman spectroscopy. In the most interesting intermediate region ($\sigma \sim 1$ N/m), we see

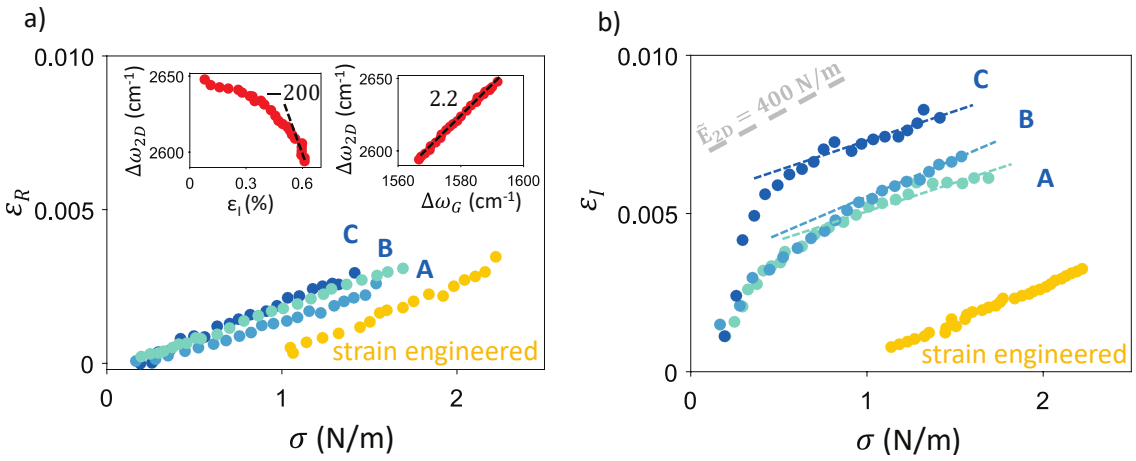

Figure 4.4: Comparision of strain-stress curves measured from Raman spectroscopy and interferometry. a) Stress-strain as determined from Raman spectroscopy, $\varepsilon_R(\sigma)$, for three standard samples A, B, and C (blue points) along with a strain engineered device (orange points). The data for the strain-engineered device is offset for clarity. Left inset: The progression of Raman $2D$ peak shift vs. ε_I used to calibrate peak sensitivity $\frac{\partial\omega}{\partial\varepsilon}$ (dashed black line). Right inset: The position of the $2D$ Raman peak plotted vs. the position of the G Raman peak. The slope of 2.2 indicates that changes in peak positions are due to strain. b) Stress-strain as determined from interferometry, $\varepsilon_I(\sigma)$, for the same devices shown in a). Dashed grey line shows slope expected for flat graphene with the stiffness $\widetilde{E}_{2D} = 400$ N/m. Dashed colored lines indicate the region of linear mechanical behavior.

Table 4.1: Linear fits to stress-strain curves to determine $\widetilde{E}_{2D}$.

Device	Interferometry $\widetilde{E}_{2D}$ (N/m)	Raman $\widetilde{E}_{2D}$ (N/m)
A	570 ± 110	498 ± 5
B	400 ± 50	554 ± 17
C	380 ± 60	424 ± 8
Strain Engineered	426 ± 7	430 ± 10

a transition from non-linear to linear mechanical response with increasing stress. For the strain-engineered device (Fig. 4.4a, b, orange points), we observe a linear and identical response from both Raman spectroscopy ($\widetilde{E}_{2D} = 430 \pm 10$ N/m) and interferometry ($\widetilde{E}_{2D} = 426 \pm 7$ N/m) throughout the range of applied stress.

Table 4.1 summarizes the stiffness extracted from each device from both determinations of strain. The uncertainty for stiffness is computed by determining the standard deviation of the parameters from the linear fit. The stiffness obtained from high stress interferometry and Raman are comparable, with the largest difference seen in device B. The measurement from interferometry is less precise because we only use the last 10 data points at high stress to estimate stiffness. Consequently, depending on the crumpled nature of the membrane, a small inconstancy in stiffness is not surprising. To confirm this view, we recognize that in our strain engineered (flat) device we have perfect agreement of stiffness between both measurement techniques. The value of stiffness is close to the value expected for flat graphene obtained in other experiments [20, 25, 111], calculated from Lamé parameters [86] ($\lambda = 2$ eV Å^{-2} and $\mu = 10$ eV Å^{-2}) and extracted from simulations

[112]. The biaxial modulus can be converted to an in-plane stiffness, $E_{2D} = (1-\nu)\widetilde{E}_{2D}$ with $\nu \sim 0.165$. This yields an average of $E_{2D} = 380 \pm 30$ N/m over all our devices. However as we learned in chapter 2, the Poisson's ratio for graphene is not well known and may not be constant or even take negative values. Therefore, we directly report the biaxial modulus $\widetilde{E}_{2D}$.

While the high stress behavior is clear, the low stress behavior is puzzling. The data of Fig. 4.4 invites the following questions. Why are the observed behavior and magnitudes of ε_R and ε_I so different? What is the nature of the nonlinearity in ε_I and can we quantify it?

4.4 The relation between stress-strain curves and crumpling

We believe the disparity between $\varepsilon_R(\sigma)$ and $\varepsilon_I(\sigma)$ at low stress is a signature of crumpling and can be understood by clarifying the definition of strain. The shifts of Raman peaks, and hence $\varepsilon_R(\sigma)$ derived from them, reflect length changes of the carbon-carbon (C-C) bonds. Quantitatively, $\varepsilon_R = \frac{(L-L_0)}{L_0}$, where L_0 and L are the lengths of the membrane before and after the application of stress averaged over the size of the diffraction limited laser spot ~ 1 μm. The true length of the membrane L is not affected by crumpling, provided C-C bond lengths are unchanged. We observe that Raman spectra for our standard samples are similar to that of substrate supported samples and that changes in the spectra vs. stress are similar in standard and strain-engineered samples. From that, we conclude that the amount of crumpling in our experiment is not sufficient to affect the C-C bonds. On the other hand, interferometric profilometry senses the profile of the entire membrane averaged to micron resolution, $\varepsilon_I(\sigma) = \frac{\left(L^{AV}-L_0^{AV}\right)}{L_0^{AV}}$, where L_0^{AV} and L^{AV} are the lengths of the averaged profiles. Thus defined L^{AV} decreases when the membrane is crumpled. The difference between L (red lines) and L^{AV} (dashed green lines) is illustrated in the cartoon of Fig. 4.5b showing cross sections of circular membranes under the application of stress. At zero applied stress, crumpling causes a large difference between the true length of the cross section, L_0, and the length of its averaged profile, L_0^{AV}. When the stress is large enough to suppress crumpling (σ_*), that difference vanishes and the true profile is virtually indistinguishable from the averaged profile, $L \sim L^{AV}$. Summarizing, ε_R is the microscopic strain, relative change in the bond lengths or the change in true membrane length, whereas ε_I is macroscopic strain, relative change in the length of the averaged profile.

This insight allows the following interpretation of the data. At small stress, the changes in L^{AV} per unit stress are large compared to those in L as the significant amount of 'hidden' length contained in crumpling is being unraveled (Fig. 4.5b, middle). In the experimental data at $\sigma < \sigma_* \sim 1$ N/m, we indeed observe much larger $\frac{d\varepsilon_I}{d\sigma}$ compared to $\frac{d\varepsilon_R}{d\sigma}$ (Fig. 4.5a). As the stress becomes larger, the amount of crumpling is gradually decreased. Finally, the crumpling is suppressed, the membrane is flat, and the difference between the change in L and L^{AV} disappears almost completely (Fig. 4.5b, right). Correspondingly, in standard

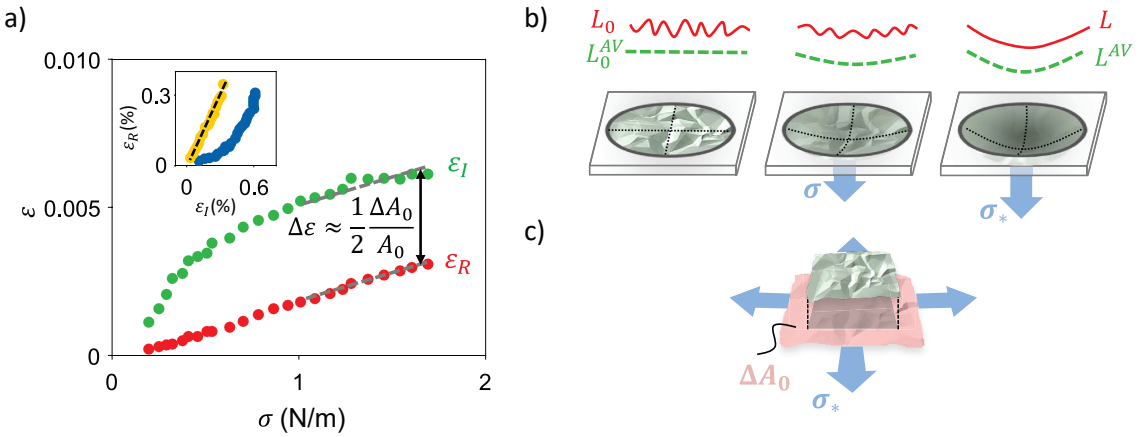

Figure 4.5: Measurement of hidden area. a) The comparison of the strain measured via interferometry (ε_I, green curve) and the strain determined via Raman spectroscopy (ε_R, red curve) vs. stress σ for device A. Inset: ε_R vs ε_I for the same device shown in the main panel (blue points) and strain engineered device (orange points). Dashed black line has slope ~ 1. b) Cartoon illustrating the evolution of crumpling in a membrane under gradually increasing stress. Cross-section of the membrane and the same cross-section averaged with micron resolution are shown above each membrane. c) Visualization of hidden area ΔA_0 of a membrane.

devices at $\sigma > \sigma_* \sim 1$ N/m (Fig. 4.5a) or in strain engineered devices (Fig. 4.5a Inset, orange points) we observe $\frac{d\varepsilon_I}{d\sigma} \sim \frac{d\varepsilon_R}{d\sigma}$ or equivalently $\frac{d\varepsilon_R}{d\varepsilon_I} \sim 1$.

The near-constant difference $\Delta\varepsilon = \varepsilon_I(\sigma) - \varepsilon_R(\sigma)$ observed in the regime of high stress is related to what is known as hidden area in geometry (see chapter 2 for details). The hidden area ΔA_0 is the difference between the true area of the membrane A_0 and the A_0^{AV} area of its projection onto a plane parallel to the membrane at zero applied stress. ΔA_0 is the amount of area hidden in out-of-plane crumpling and is revealed when the membrane is stretched. From simple geometrical considerations, $\Delta\varepsilon \approx \frac{\left(L_0^{AV} - L_0\right)}{L_0} \approx \frac{1}{2}\frac{\left(A_0^{AV} - A_0\right)}{A_0} = \frac{1}{2}\frac{\Delta A_0}{A_0}$. We use the relative hidden area $\frac{\Delta A_0}{A_0}$ extracted from $\Delta\varepsilon$ to quantify the amount of crumpling in our devices. We obtain relatively large $\frac{\Delta A_0}{A_0}$ of 0.6, 0.8 and 1.0 % for devices A, B, and C respectively.

4.5 Exploring the nonlinear response

Having obtained a quantitative measure for crumpling strength, we further investigate the nonlinear behavior of the macroscopic strain (ε_I) relevant for most experiments.

The comparison of our experimental data with the predictions of Eq. 2.60 is greatly facilitated by our complementary measurements of ε_I and ε_R. By taking the difference $\varepsilon_I(\sigma) - \varepsilon_R(\sigma)$, we isolate the contribution of the nonlinear term in Eq. 2.60 pertaining to the mechanics of crumpling. To account for built-in stress in our devices, we subtract an additional term $\varepsilon_0 = \varepsilon(\sigma_0)$, where σ_0 is built-in stress leading to Eq. 4.2. This

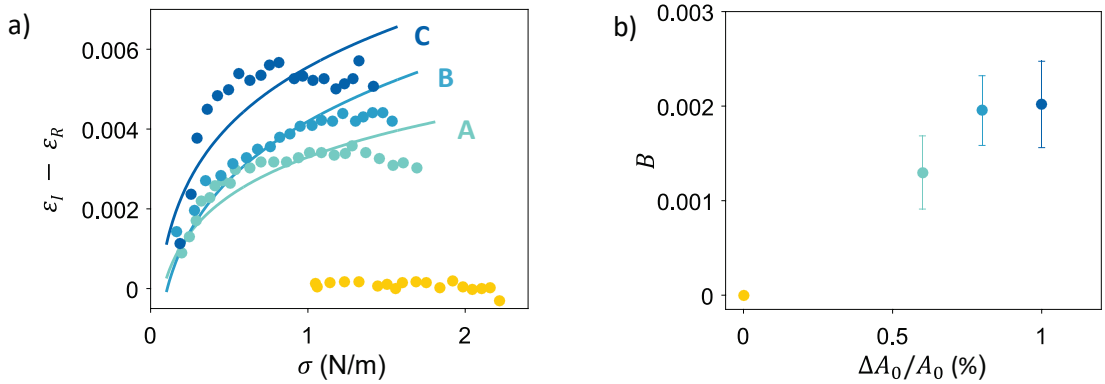

Figure 4.6: Fits to Anomalous Hooke's law (Eq. 4.2) as described in the main text. a) The difference between the strain extracted from interferometry and the strain from Raman $\varepsilon_I - \varepsilon_R$ vs. stress σ for standard samples A, B, C (blue points) and the strain-engineered device (orange points). Solid lines are fits to the non-linear model described in the main text ($\varepsilon \propto \sigma^\alpha$). b) Disorder parameter B from the model vs. experimentally determined hidden area $\frac{\Delta A_0}{A_0}$. The correlation indicates higher disorder in the model corresponds to a higher crumpling strength as seen in experiment.

Table 4.2: Anomalous Hooke's law fit parameters for devices A, B, and C.

Device	α	σ_* (N/m)	σ_0 (N/m)
A	0.08 ± 0.02	0.8 ± 0.2	0.07 ± 0.01
B	0.16 ± 0.02	0.9 ± 0.1	0.09 ± 0.01
C	0.11 ± 0.02	0.8 ± 0.1	0.05 ± 0.01

allows us to compare our data (where only applied strain is measured) with the model:

$$\varepsilon(\sigma) - \varepsilon(\sigma_0) = \frac{\sigma_*}{E}\left[\frac{\sigma}{\sigma_*} + \frac{1}{\alpha}\left(\frac{\sigma}{\sigma_*}\right)^\alpha - \frac{\sigma_0}{\sigma_*} - \frac{1}{\alpha}\left(\frac{\sigma_0}{\sigma_*}\right)^\alpha\right]. \tag{4.2}$$

We are then able to fit our experimental data for devices A, B, and C to the non-linear component in Eq. 4.2 with $\widetilde{E}_{2D}$ determined from interferometry at high stress and α, σ_*, and σ_0 treated as free parameters. We estimate for the uncertainty in the non-linear fits as follows. We calculate the change in residual of the fit by varying the device stiffness, $\widetilde{E}_{2D}$, by the standard deviation obtained from the linear fits in table 4.1. Then we vary each parameter in the model independently to achieve the same change in residual with all other parameters remaining constant. The amount we change the input parameter to achieve the same residual change we deem the uncertainty in that parameter.

Figure 4.6a illustrates the adherence of our data to the non-linear model with fit parameters listed in table 4.2. For all standard devices, we retrieve an average exponent $\alpha = 0.12 \pm 0.02$. This is close to $\alpha = 0.1$ expected for statically wrinkled graphene, confirming our earlier interpretation that static wrinkling rather than flexural phonons is the primary contributor to crumpling (chapter 3). The average value of built-in stress

obtained from the fit, $\sigma_0 = 0.07 \pm 0.01$ N/m, is close to what is observed by others. The average cross-over stress was found to be $\sigma_* = 0.8 \pm 0.1$ N/m. Physically, this means a stress of at least 0.8 N/m was required to flatten the sample and retrieve a linear response at higher stress. In agreement with that, linear $\varepsilon(\sigma)$ was observed for the strain-engineered device where we estimate $\sigma_0 = 0.84 \pm 0.02$ N/m ($> \sigma_*$). It should be noted that the fits are not perfect indicating that there are facets of our experimental data not accounted for by the model. Possible reasons for deviations include: non-uniform stress fields, non-random wrinkle distribution, deviation of the geometry from perfectly circular, and presence of contaminants. We recognize that there may be polymeric residues left on our devices from the fabrication stage. While such residues may contribute to crumpling, their direct effect on the mechanical response of the membrane is expected to be insignificant [113].

The notion of the hidden area can be further used to compare the data to prediction of the model of Ref. 47. There, the degree of crumpling was controlled by the disorder parameter: $B \propto \frac{(\sigma_* - \sigma_0)}{\widetilde{E}_{2D}}$. In Fig. 4b, parameter B extracted from our fits vs. $\frac{\Delta A_0}{A_0}$ is plotted. The correlation seen in Fig. 4.6 means that higher crumpling measured experimentally does, in fact, correspond to higher disorder in the model.

4.6 Possible measurement artifact: graphene slipping

Delamination and slipping of graphene from the substrate surface can happen, potentially distorting our measurements. One careful study of graphene on SiO_2 found delamination occuring at ~ 2.5 MPa for similar sized devices. This is one order of magnitude higher than the pressures we apply [104]. In our data, identical responses for both positive and negative pressures (colored vs. grey curves in Fig. 4.2) confirm that there was no significant slippage or delamination occurring between graphene and the SiN_x interface. With that in mind, if slipping and delamination were occurring, their effects would be seen the in strain engineered device as well, yet it had a perfectly linear behaviour. Additionally, the high pressure device of Fig. 4.7 also shows a perfectly linear mechanical behaviour at even higher stresses > 2 N/m. These conclusions are also consistent with the lack of discontinuities in pressure vs. deflection curves or consequently the strain vs. stress curves. Some devices did show hysteric behaviour, but it is unclear if this was due to slipping, excess contaminants or reorganisation of crumpling (e.g. buckling). Devices like this were excluded from the previous study on the anomalous Hooke's Law of graphene.

4.7 Why do we see such large effects of crumpling?

While working on this project, we noticed that while others have measured mechanical response of graphene, they do not see 'softnening' of E_{2D}. One notable exception is Ref. [57]. Below I would like to suggest a few possible reasons as to why our data are different.

First, all prior work assumes that microscopic and macroscopic strain measurements are identical. We have shown that the two, in general, are not equivalent. Microscopic strain measurements such as Raman spectroscopy only probe C-C bond changes. Therefore, regardless of whether the membrane is crumpled or flat, the measured mechanical constants from this method will always be that of flat graphene. On the other hand, macroscopic strain as measured through e.g. membrane deflection, includes the effects of crumpling. In our experiments, we reconcile this difference by directly comparing the mechanical response of graphene measured by both techniques in tandem.

Second, we use comparatively large devices of circular shape ~ 10 μm in diameter (and even larger in chapter 3). Since crumpling is a highly scale-dependant phenomenon, larger samples are more likely to have crumpling large enough to measurably affect the mechanical response. Furthermore, the circular geometry is a complicated boundary condition to fulfil without wrinkling due to uneven stresses during transfer [114, 115]. This means, in thin nanoribbons, crumpling is likely suppressed to the point it is not noticeable. We have seen evidence of this in chapter 3. This means graphene nanoribbons used in many works likely have highly suppressed crumpling.

Third, we apply uniform stress to our samples as opposed to non-uniform stress used in an AFM indentation test. We believe the high stresses applied by AFM tips may conceal mechanical evidence of uncrumpling. In the analysis of such AFM indentation data, one needs to correctly determine the equilibrium of forces to find the zero-point of the measurement which is quite tricky and has a large impact on the extracted mechanical constants. Reliable fitting of stiffness can only be performed at large indentation where crumpling, if originally present, will be suppressed. Further, the selection of the spring constant of the AFM cantilever is also important; one requires a cantilever of similar spring constant to the effective stiffness of the membrane. This is experimentally found to be $1 - 10$ N/m and supports the use of cantilevers in this range to probe the Young's modulus of ~ 1 TPa. Crumpling can reduce the effective stiffness of a sample by an order of magnitude (or more), making the mechanics of crumpling more difficult to detect since it would require even softer cantilevers ($0.1 - 1$ N/m). See Appendix B for more information regarding AFM indentation for mechanics measurements of 2D materials. Some experiments *do* apply uniform stress. In those works, completely sealed pits in silicon are used in contrast to our to open holes in SiN_x membranes. It is possible that open holes and closed pit samples are not equivalent since there will be trapped gas in the latter case.

Fourth, by clamping our samples very tight to increase the effectiveness of the O-ring seal, we were able to measure the response of a standard sample at pressures > 200 KPa as shown in Fig. 4.7. We find a stiffness of 380 ± 18 N/m in agreement with that expected for flat graphene. It is easy to see how nonlinear effects at low stress could be easily overlooked. In the measurement of high pressure data in Fig. 4.7, we used a course pressure gauge. The first data point is already at fairly large stress (> 1 N/m), concealing

the effects due to crumpling and nonlinear mechanics if present. This highlights the importance of careful pressure measurement using the digital pressure gauge with precision < 1 KPa as used to obtain our main results above.

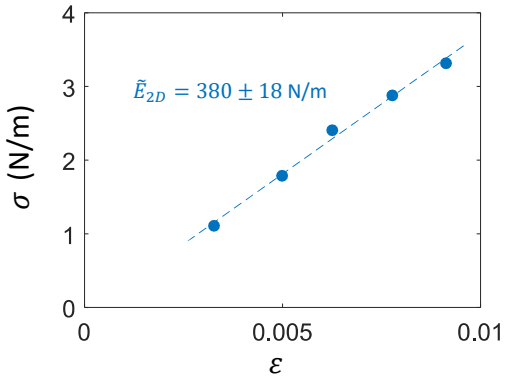

Figure 4.7: Demonstration of linear device mechanics using a course pressure gauge. The first data point is > 1 N/m, which is enough to fully suppress crumpling. This demonstration illustrates the importance of measuring the low stress regime carefully.

Finally, it is important to consider that the nature of crumpling is random. Therefore even small differences in fabrication procedures may have a large impact on the topography of the final device. So perhaps, the fabrication procedure we use produces highly crumpled samples.

4.8 Conclusion

In conclusion, we observed the crossover from nonlinear mechanical response of graphene in the regime of low applied stress to linear response at high stress. The low stress regime gave results consistent with chapter 3, where an electrostatic actuation scheme was used instead of gas. The degree of nonlinearity and the crossover stress were found to depend on the amount of crumpling. We determined the latter, as quantified by the hidden area, through complementary Raman spectroscopy and interferometry measurements. Our data are in good agreement with recent theoretical predictions of the 'anomalous Hookes law' in crumpled membranes. Furthermore, we have demonstrated the distinction between experimentally measuring the microscopic or macroscopic mechanical response of materials.

CHAPTER 5

RENORMALIZATION OF BENDING RIGIDITY

In this chapter I present fabrication techniques to create graphene cantilevers and preliminary measurements of their bending rigidity κ. We find that our devices are significantly stiffer to bend than 1 eV, the bending rigidity of flat graphene. This increase of bending rigidity is likely related to crumpling. Since it is a challenging endeavor to construct a singly clamped atomically thin structure, candidate devices rarely survived to be measured. The process of fabrication also teaches us how atomically thin cantilevers behave and may allow us to gain insight into the optimum fabrication route for future work. Such cantilevers have potential as sensitive force sensors.

5.1 Device Fabrication

Graphene cantilevers were carved with a Ga+ ion beam (Novalab 600 Dual-Beam FEI) with 30 KeV, 50 pA current using the cuts similar to those in chapter 3. The general cutting procedure is shown in Fig. 5.1. We start with suspended graphene prepared similarly to the membranes used in chapters 3 and 4. Figure 5.1a shows the procedure for creating a 'pure' graphene cantilever, whereas Fig. 5.1b shows the procedure for creating a graphene cantilever with a Silicon Nitride (SiN_x) piece attached to the cantilevers end. This is advantageous for the interferometric measurement scheme, were the paddle can be used as a large reflector. First, two parallel cuts, labelled ① and ②, are made to make a ribbon. The final cut labelled ③ frees the cantilever. For the case of the devices with the SiN_x paddle, the final cut takes a significantly longer time and must be at least 500 nm wide to ensure the nitride is completely severed.

This procedure has low yield and seldom results in a stable device. Figure 5.2 shows most of the common

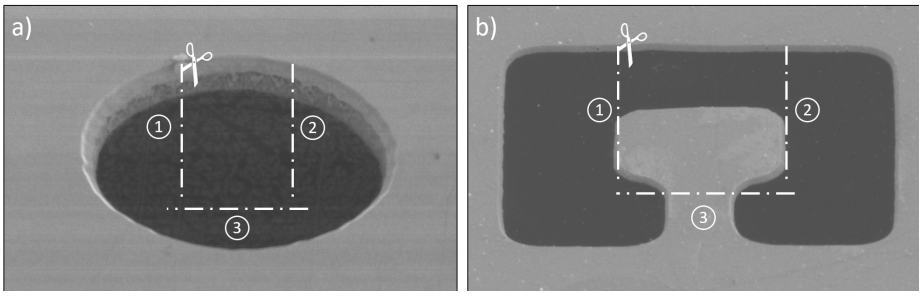

Figure 5.1: General fabrication for graphene cantilevers. Suspended graphene over a) circular hole and b) rectangle with paddle. The cuts along the dashed lines are performed with a FIB. a) Cuts result in a 'pure' graphene cantilever. b) Cuts result in a cantilever with a paddle on the end.

failure mechanisms. Perhaps the primary source of failure is the destructive nature of the ion beam. It induces defects and can damage graphene far from the defined cut region, even under perfect beam conditions (see chapter 3 and below). The Ga+ ions can implant and adsorb on to graphene or the surrounding substrate and cause significant heating. Also, when milling SiN_x there is likely additional sputtering occurring. Figure 5.2a (left and middle) shows graphene rupturing during cuts, likely from the above mechanisms. It is also possible that failure occurs along a grain boundary of graphene. Figure 5.2b (right) shows a 'cross' cut that should result in four triangle cantilevers, but the graphene furls up and adheres to to itself. Another mode of failure is shown in Fig. 5.2b. Upon performing the final cut, the cantilever 'springs away' due to releasing significant built-in stress. We hypothesize that the built-in stress could come from the transfer of graphene and depend on initial hole shape and PMMA residue, be induced by the ion beam cutting, or bending of the nitride (shown in Fig. 5.2b, left).

Even when fabrication is successful, another challenge is removing the devices from the FIB for measurement. Graphene cantilevers are potentially the worlds' most sensitive electrometers with spring constants as low as $k \approx 1 \times 10^{-8}$ N/m. Consequently, any uncontrolled force in the system could render them unstable as shown in Fig. 5.2c. Even though graphene is conductive, SiN_x is highly insulating. Embedded electrons and ions could cause charging on the cantilever. Also, van der Waals interactions with the vertical side walls could also cause unwanted cantilever deflection. Differential stress could be induced due to varying amounts of surface contaminants on either side of the graphene since only the top side was coated in PMMA during fabrication. Normally, the effect of gravity can be ignored in MEMS, but graphene cantilevers are extraordinarily sensitive. Even the mass of a paddle ($\sim 2 \times 10^{-14}$ Kg) could cause measurable deflections. Finally, ubiquitous $\frac{1}{f}$ noise in mechanical systems could excite the cantilever and add to the above instability mechanisms.

Despite a large number of fabrication failures, stable cantilevers do sometimes survive. Figure 5.3 shows one such an example of successful cantilever fabrication. In the following sections we study the behavior of similar devices that survived to be measured after unloading from the SEM.

There has been a few recent works that explore alternate methods to fabricate graphene cantilevers. For example, graphene cantilevers have been suspended with vapor phase etching [33], by using thick samples [32], and prevented furling by stabilizing cantilever edges with carbon nanotubes [116]. The most successful technique involves ebeam patterning and manipulating graphene with microprobes and magnetic paddles within liquid [34]. However, this technique cannot be extended to measurements in vacuum.

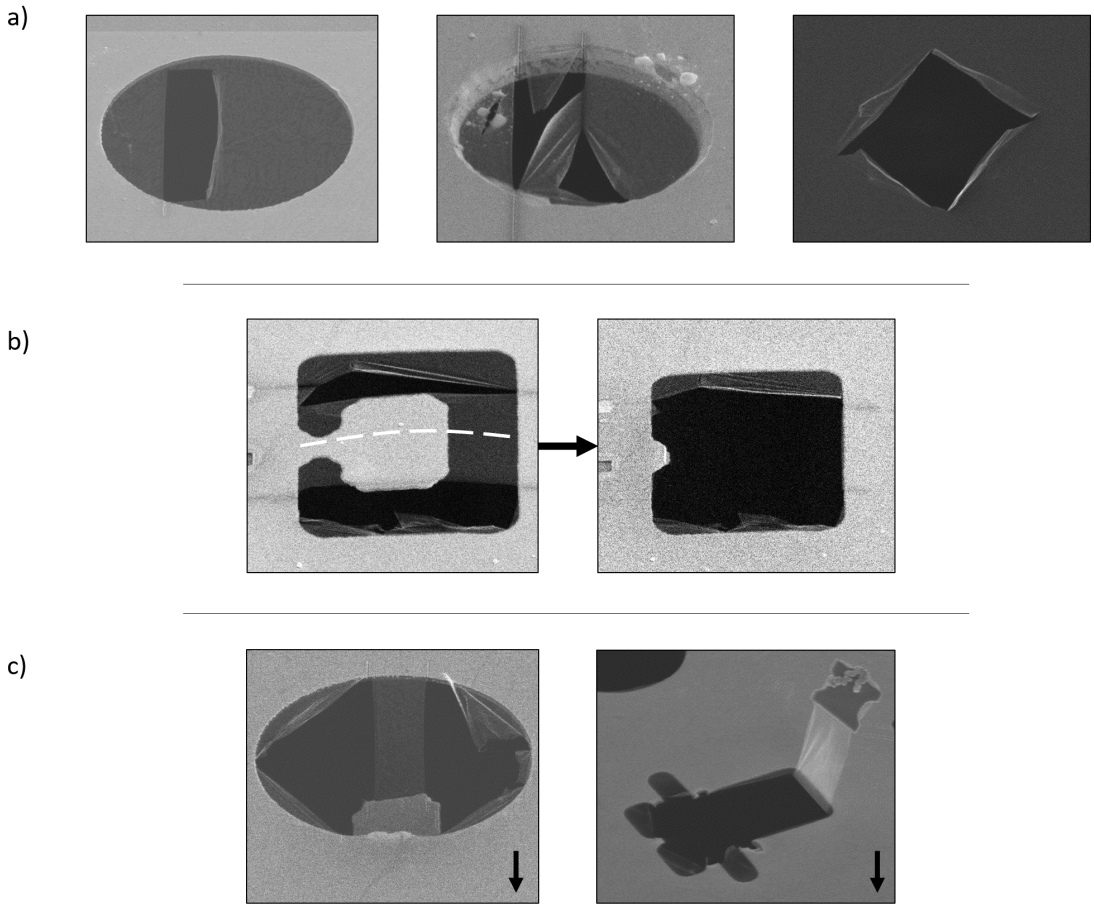

Figure 5.2: Cantilever fabrication failure mechanisms during FIB milling. a) Rupturing, tearing and self-adhesion. b) 'Springing' away after final cut. In this case you can see the initial device is curved (dashed line). c) Drifting downwards (upwards) toward (away) from gravity prohibiting measurement. Arrow indicates direction of gravity.

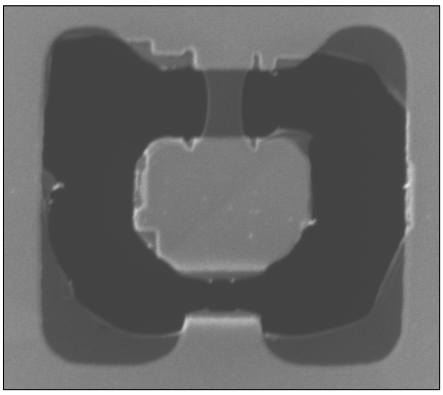

Figure 5.3: SEM of successfully fabricated cantilever. The cantilever is stable within the SEM and can be observed for many minutes.

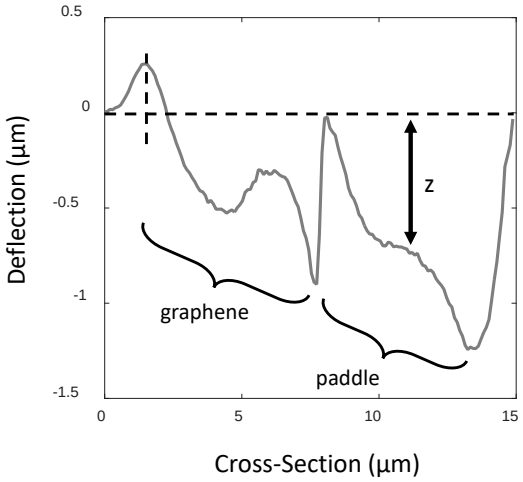

Figure 5.4: Deflection of graphene cantilever under the influence of gravity. Cross-section of cantilever deflection as measured by interferometric profilometry. There is an arbitrary phase jump at the each graphene/SiN_x interface that should be ignored. We can easily measure the out-of-plane displacement $z \sim 0.55$ μm at the center of the paddle

5.2 Preliminary Measurements

5.2.1 Static deflection due to gravity

In our first approach, we determine the bending rigidity by measuring the deflection of the cantilever due to its weight, $F = mg$. Since we observe the cantilevers sometimes deflect upwards, away from gravity (Fig. 5.2c, right), we know that this may be a poor assumption but we should at least check if the estimate makes sense.

The mass of the cantilever shown in Fig. 5.3 is dominated by the 5×5 μm paddle, that has 50 nm of gold and 300 nm of silicon nitride yielding a mass of approximately $m = 2 \times 10^{-14}$ Kg. The mass of the graphene is negligible ($\sim 10^{-17}$ Kg). From the deflection $z = 0.5$ μm measured from the profilometry in Fig. 5.4 under the influence of the force $F = mg$, we calculate a lower limit of the bending rigidity $\kappa > 100$ eV. This is factor of 10^2 larger than expected for flat graphene. Unfortunately the force due to gravity cannot be adjusted. To better measure κ we need to control F.

5.2.2 Electrostatic actuation

Another way to precisely measure κ is by monitoring deflection via interferometric profilometry under known forces. We developed such a scheme using electrostatic actuation of membranes in chapter 3. We first calibrate the technique for cantilevers with similar geometry. We fabricated these calibration cantilevers from silicon nitride (SiN_x) since it is a well characterized material.

Here we used a ~ 150 nm thick SiN_x film coated with ~ 30 nm of gold (to allow for gating), patterned

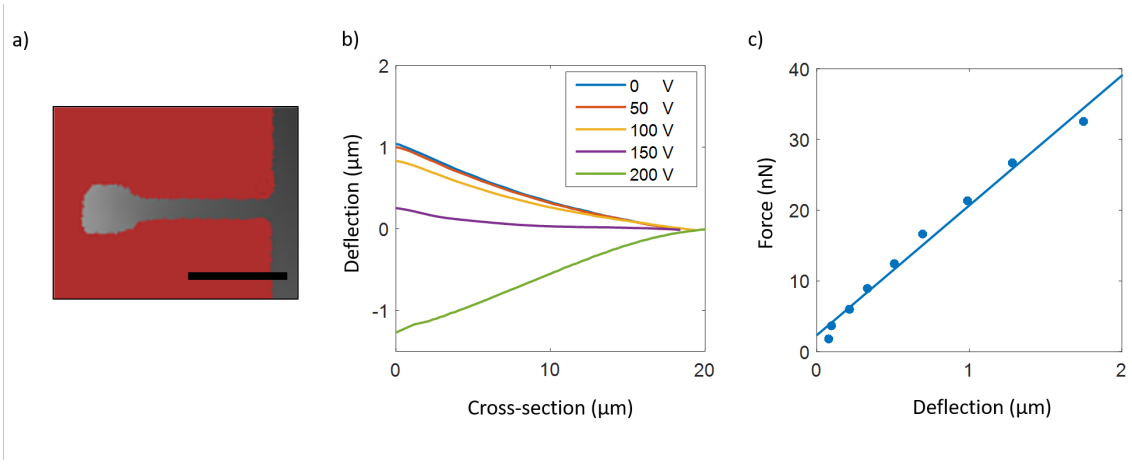

Figure 5.5: Silicon Nitride cantilever measurements. a) Interferometric image of SiN_x cantilever, scale bar is 10 μm. Greyscale is deflection and pink is missing data since there is no material to reflect light under or around the cantilever. b) Cross-sections of cantilever under electrostatic pressure controlled by actuating voltage. The cantilever is initially deflected upwards due to differential stress from fabrication. c) Estimated force from electrostatic pressure vs. measured deflection curves. Line is a fit for the effective spring constant $k \sim 0.02$ N/m

into a ~ 18 μm long ~ 2.5 μm wide cantilever with a ~ 5 μm paddle on the end. An interferometric image of the device is shown in Fig. 5.5a and its electrostatic response is shown in Fig. 5.5b. Force is applied by applying voltage across the cantilever and a gating chip underneath, see chapter 3 for details. The force is estimated by taking the area of the cantilever and multiplying by the effective electrostatic pressure assuming a parallel plate capacitor geometry. Then, the force vs. deflection curves are fit to a straight line as shown in 5.5c. The slope of this curve is the spring constant: $k \sim 0.02$ N/m. This is close to that calculated from Eq. 2.34 in chapter 2: $k = \frac{Et^3w}{4L^3} \sim 0.1$ N/m, where $E \sim 300$ GPa is the Young's modulus of SiN_x. Although the measured and calculated spring constants are close, they are not in perfect agreement. This is expected because a small uncertainty in t or L can cause large differences in the calculated spring constant. Furthermore, we have neglected the effects of built-in stress and small layer of gold. This is why in AFM, spring constant calibration is typically performed by measuring the amplitude of thermal brownian motion of the cantilever end, which is less prone to these uncertainties.

Applying the electrostatic actuation scheme to graphene cantilevers is not straightforward when fabrication is successful. The cantilevers are hard to transport to the measurement setup without destroying them. The most careful protocol we devised was to fabricate cantilevers when the chip was already within the measurement clamp which was grounded to prevent unwanted charging. Then, the clamp becomes a make-shift Faraday cage for transport. Even this method had low yield, but it allowed a simple electrostatic measurement.

Figure 5.6 shows the electrostatic actuation of a ~ 5 μm long graphene cantilever with a 5×5 μm paddle

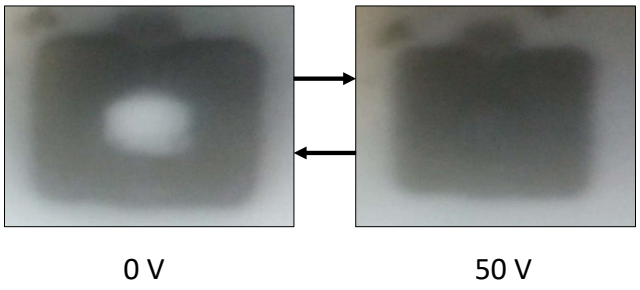

Figure 5.6: Interferometric video snapshots of repeatable electrostatic actuation of a graphene cantilever. Left, only the paddle is visible as a white spot. Right, it becomes invisible to the interferometric imaging technique at the lowest voltage (50 V).

on the end. In these images, graphene is barely visible. Initially, at zero applied force (0 V) the paddle is visible. However, upon application of force (50 V) the cantilever is bent and the paddle is shifted out of view. This is because with the interferometer we can only measure up to 10° deflection before the reflected light is no longer collected by the objective. For a 5 μm graphene cantilever, the maximum displacement we could see at the edge of the paddle is $z_{max} \approx 5 \times \tan(10) \approx 1$ μm. The electrostatic pressure we apply at 15 μm gate distance and 50 V is ~ 50 Pa. Since the area of the cantilever is $\sim 5 \times 10$ μm^2, the force applied to this cantilever ~ 2.5 nN. By assuming this force is *just* enough to bend the paddle out of range we get an upper estimate for spring constant: $k < \frac{F}{z_{max}} \approx 2.5 \times 10^{-3}$ N/m and therefore bending rigidity $\kappa < 5$ KeV.

5.2.3 Dynamics

On occasion, the final cut in the fabrication stage will cause excitation of the cantilever, as shown in Fig. 5.7. The blurriness apparent in Fig. 5.7 stems from the vibration of the cantilever which is much faster compared to the raster speed of the SEM. The fastest raster speed (50 ns per line) of the SEM cannot resolve the cantilevers motion. This does however allow us to estimate a lower limit of the bending rigidity of the cantilevers. This cantilever has width, $W = 5$ μm and length $L = 7.5$ μm. The field of view of the scan shown in Fig. 5.7 is $\sim 10 \times 10$ μm^2, this allows us to determine that the vibration amplitude is $A \sim 1-5$ μm. It is hard to get a very accurate number here because it is impossible to differentiate between the lateral extent of the paddle compared with the vibration of the end of the paddle. Since Fig. 5.7 has ~ 64 lines per μm, we can estimate the resonant frequency of the device $f = \frac{t}{A} > 0.5 - 3.0$ MHz, where t is the time to scan amplitude of the paddle.

With resonant frequency we can estimate the cantilever spring constant $k = m(2\pi f)^2 > 0.1 - 10$ N/m and therefore corresponding bending rigidities of $\kappa > 5 - 500$ MeV! However, we cannot assume the entire

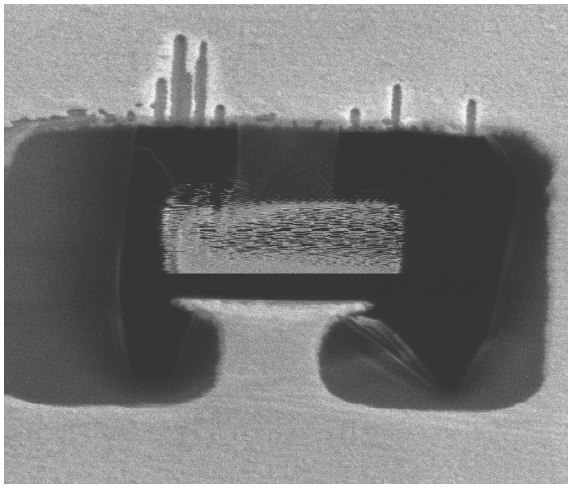

Figure 5.7: Example of oscillating cantilever after fabrication. The highest raster speed of the SEM cannot resolve its motion — hence the cantilever appears blurred.

cantilever is bending. In fact, from the SEM image of Fig. 5.7, it seems as if only the paddle at the end is moving. This brings up the possibility that the entire cantilever is very rigid apart from the final ~ 100 nm where it behaves like a hinge. From this, following the same analysis above yields $\kappa \sim 40 - 4000$ eV in agreement with other measurements.

5.3 Other explanations for bending rigidity renormalization

In all of the preliminary measurements above we extract $\kappa \gg 1$ eV. Given our results in chapters 3 and 4, it is natural to assume that this stiffening compared to $\kappa = 1$ in flat graphene is elastic constant renormalization due to crumpling. Indeed, static wrinkles could still persist in the cantilever. Assuming regular corrugations of 1 nm we estimate $\kappa \approx 10^3$ eV from Eq. 2.42. However, it is pertinent to remember that the scale of forces in the cantilever experiments above is very different from those used to probe in-plane stiffness. Therefore there are a number of other explanations for this data.

First, the effects of gaussian curvature in the free energy cannot be neglected in Eq. 2.11 as for fully clamped membranes as disccussed in chapter 2. In other words, overall curvature of the the device facilitated by the free edges can stiffen the beam. An estimate for the relative change in stiffness due to gaussian curvature is as follows [117]:

$$\frac{\Delta k_G}{k} = \frac{L^2}{60}\frac{\beta^4}{\eta^2}e^{-c\beta}\left(\kappa_y - \nu\kappa_x\right)^2 = \frac{L^2}{60}\frac{\beta^4}{\eta^2}e^{-c\beta}\kappa_y^2 \tag{5.1}$$

where L is the length of the cantilever, $\beta = \frac{w}{L}$ with width w, $\eta = \frac{t}{L}$ with thickness t, numerical constant

$c \approx 3$ and $\kappa_{x,y}$ are curvatures along the x and y directions. Here only the transverse (defined as y) curvatures contribute to stiffening of the beam. This yields a relative stiffening of up to a factor of 10^6 ($\sim 10^{-2}$ N/m) for an assumed curvature of $\kappa_y = \frac{1}{1\times10^{-6}}$ μm^{-1}. Even for weaker curvatures of $\kappa_y = \frac{1}{100\times10^{-6}}$ μm^{-1} yields stiffening of a factor of 10^2.

Second, free edges of the cantilevers could roll up into nanotubes. This would increase the rigidity by a large amount. Modelling the edges as solid cylinders we get an effective spring constant expressed as [116]:

$$k_{roll} = \frac{3\pi r^4 E}{2L^3} \tag{5.2}$$

Here E is the Young's modulus of graphene, and r is the radius of the nanotube at the edge. For a roll as small as 10 nm yields an effective spring constant of $k \sim 1 \times 10^{-6}$ N/m.

Third, bending rigidity may also be affected by defects induced during fabrication. The FIB fabrication procedure induces defects well beyond the region of the cut, since even when the FIB is well focused, there is a large ion tail that extends laterally. Typically such a beam follows a Holtsmark rather than Gaussian distribution [118]. We have seen in chapter 3 that each cut induces a defect density of $\leq 5 \times 10^{12}$ cm^{-2}. While we found earlier that the presence of defects does not change the stiffness. The same conclusion cannot be made for bending rigidity. In fact, the problem is worse for cantilevers with paddles since we have to mill through the SiN$_x$ which takes a much higher dose to achieve. Figure 5.8 shows an example Raman spectra taken on the center of a graphene cantilever with ion-milled SiN$_x$ paddle. The spectrum indicates the presence of graphene oxide. Presumably, the large dose required to mill the SiN$_x$ made the graphene heavily defective. Upon venting the FIB chamber, oxygen then attaches to the defect sites forming oxide. Although it is predicted that graphene oxide should have lower κ than graphene [119], it is unclear how the defects and/or contamination of re-depositing SiN$_x$ contribute to the effective rigidity of graphene. Furthermore, these defects can contribute to the crumpled landscape of the material. Using helium ion microscopy (HIM) instead of FIB could help reduce defects since the beam can be controlled to higher precision.

Finally, although we can neglect contaminants such as PMMA resist in the study of in-plane stiffness (chapters 3 and 4), it is likely that the effects are more prominent in cantilevers. The fact that cantilevers during fabrication sometimes rise away from gravity points to other forces present in the system. Although these could be from electrostatic charging and van der Waals interactions, it is also possible the culprit is PMMA resist. A layer with flexural modulus $E_{flex} \sim 3$ GPa as thin as $t = 5$ nm is enough to explain the stiffness of the cantilevers: $k = E_{flex}\frac{4wt^3}{L^3} = 1 \times 10^{-5}$ N/m. Another contaminant present on graphene is water. The effect of adsorbed water that is present on all surfaces at ambient temperature and pressure on the mechanical response of graphene is unknown.

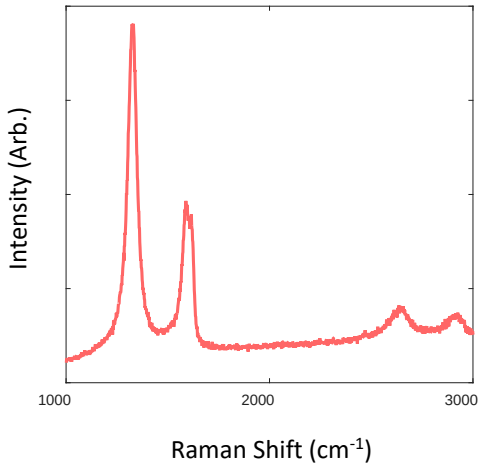

Figure 5.8: Raman spectra from the center of a cut graphene cantilever which included the milling of SiN_x. The spectra is indicative of graphene oxide, meaning FIB milling of SiN_x in the vicinsity of graphene causes a large number of defects.

To conclude that the renormalized bending rigidities measured here are really due to crumpling, one would have to perform additional studies. For example, if the renormalization were caused by flexural phonons, then κ should be both temperature and device size dependent. If static crumpling was the primary cause, one would expect to see modulation of κ via controlled undulations through, for example, patterned substrates.

5.4 Conclusion

Mechanical measurements of cantilevers offer the best way to study the bending rigidity of 2D materials. However these cantilevers are extraordinarily difficult to fabricate and measure. Despite low yield, we find $\kappa \gg 1$ eV from gravity deflection, electrostatic actuation and resonance measurements. Although such high bending rigidity can be caused by crumpling, we cannot rule out other artifacts such as rolled edges, defects, and contaminants. A summary of the measurements and calculations is shown in table 5.1. Developing a scheme that allows fabrication and measurements in-situ and in vacuum will be fruitful but highly challenging.

Table 5.1: Summary of measured bending rigidities of graphene (top). Bottom: Expectations of increased bending rigidity stemming from different mechanisms. All calculations are performed with 5×5 μm^2 cantilever.

Method	k (N/m)	κ (eV)
flat	1×10^{-8}	1.2
gravity	4×10^{-7}	1×10^{2}
electrostatic	3×10^{-3}	$< 5 \times 10^{3}$
resonances	$10^{-7} - 10^{1}$	$10^{1} - 10^{6}$
curvature	$10^{-6} - 10^{-2}$	$10^{3} - 10^{5}$
corrugations	1×10^{-5}	1×10^{3}
edges	1×10^{-6}	1×10^{2}
contaminants	1×10^{-5}	1×10^{3}

CHAPTER 6

CONCLUSION AND FUTURE WORK

6.1 Conclusion

It is clear that graphene has remarkable mechanical properties — high in-plane stiffness and low bending rigidity. I have shown that out-of-plane crumpling greatly renormalizes these properties. To measure the effects of crumpling on the mechanical response of 2D materials, I developed a new interferometric bulge test technique applicable at low applied stresses and cryogenic temperatures. I then extended this technique to allow complementary measurement of strain via Raman spectroscopy at higher stresses applied with gas pressure. Specifically, I have shown that static wrinkling reduces the in-plane stiffness of graphene by up to 10 times compared to flat graphene. I have shown for the first time experimentally, that graphene exhibits a nonlinear ('Anomalous') Hooke's law at low stress. To measure the bending rigidity, I developed process flows to fabricate atomically thin cantilevers. Although difficult to measure, I have also shown that the bending rigidity is increased by at least $10^2 - 10^3$ times compared to flat graphene. While the origin of stiffening could potentially be crumpling, it is currently unclear and requires more detailed experiments and refined fabrication procedures.

My observations reinforce the idea that great care is needed when applying classical elasticity theories to atomically thick materials. I demonstrate that clearly defining strain is critical to the understanding of 2D materials. Strain can refer to stretching the bonds in the lattice or to stretching an entire micron-scale device. These two types of strain are not always equivalent. This distinction is currently not widely considered in literature.

6.2 Future work

The elastic constants of 2D materials strongly depend on crumpling. Since crumpling is a salient feature of graphene or *any* 2D material membrane at finite temperature, the results reported here are relevant to the majority of the experiments and devices dealing with 2D materials. For example, in most mechanical experiments the linear mechanical response of 2D materials is *assumed* in the regime of low stress (e.g. [11, 120]). The conclusions of some of these works may need to be reassessed. Changes in the effective stiffness will affect operation of graphene nanoelectromechanical devices including resonators, mass sensors and switches. And further, controlling crumpling could enable tuning of the mechanical constants in a wide range or enable the design of highly anisotropic devices. Extremely soft devices may be useful, for example, as exquisite force sensors.

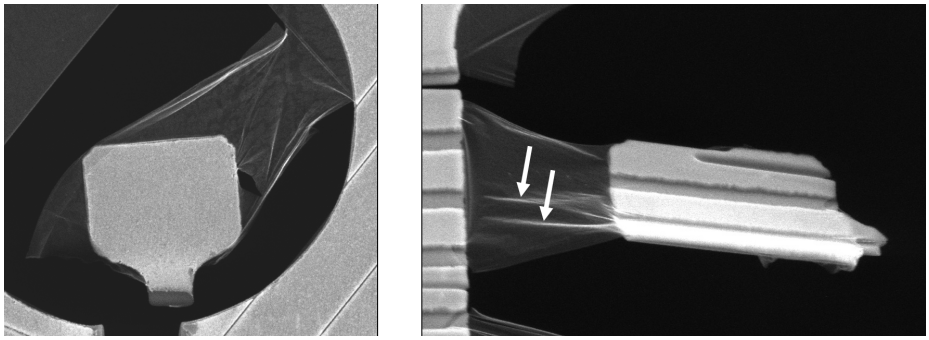

Figure 6.1: Controlling stiffness of graphene cantilevers via crumpling. Left) A cantilever that crumpled during fabrication. Heavily crumpled cantilevers appear very stiff. Right) Controllably corrgated graphene cantilever. Corrugations were formed by patterning grooves into the substrate prior to graphene transfer. Arrows highlight significant wrinkles induced by the groove edges.

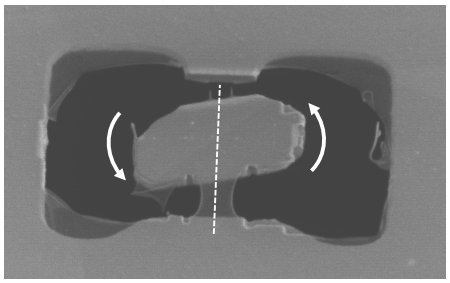

Figure 6.2: Example device for torsion measurement. Force could be applied to one side of the paddle by using light pressure from a focused laser spot. Deflection and/or angle can be monitored with high angle SEM. A more stable geometry may include an additional graphene ribbon, as opposed to the cantilever shown here.

A key future direction is to study the effect of crumpling on the bending rigidity of 2D materials in more detail. This could be facilitated by controllably inducing corrugations of known wavelength and amplitude into cantilevers as shown in Fig. 6.1.

There are many other basic mechanical parameters which could be investigated. For example, it would be interesting to apply non-uniform strain, shear or torsion as has been done in other nanomechanical systems [121]. An example of a torsion measurement is shown in Fig. 6.2. Perhaps the most interesting parameter that is heavily influenced by crumpling is the Poisson's ratio ν. It too is renormalized and depends on crumpling strength. For a highly crumpled device one expects $\nu = -0.3$ [122]. This negative Poisson's ratio means that the membrane would extend transversely as it is stretched. One could potentially extract ν by comparing the mechanical response of a uniaxially stressed (ribbon) and a biaxially stressed (circular membrane) devices in both crumpled and strain engineered 2D membranes.

Extending the quasi-static measurements of this work to multilayer graphene, other 2D materials and

heterostructures offers other platforms to study the coupling between bending and stretching in different thin systems [123]. For example, MoS_2 has $E_{2D} \sim 180$ N/m and $\kappa \sim 10$ eV [124, 125]. Here, due to the lower in-plane stiffness and higher bending rigidity the anharmonic effects of flexural phonons should be reduced by ~ 100 times. This offers another way to suppress the effects of flexural phonons without application of high strains or changing temperatures. One could use other materials like this or varying thickness, as a platform to investigate the competition between static and dynamic crumpling.

Moving toward dynamic measurements, is essential to gain a full understanding the nanomechanics of thin materials. As such, it would be interesting to consider how competition between static and dynamic crumpling, renormalized elastic constants, and the low stress nonlinear response may affect the function of MEMS oscillators. In such oscillators, it has been suggested that wrinkles may be an overlooked dissipation mechanism [91, 126, 127].

6.3 The future of 2D mechanics

Graphene has been considered a wonder material with many proposed applications in the areas of electronics, thermal management, and MEMS. The future of graphene and other 2D materials is still uncertain, but the study of mechanics in these systems has become much more interesting. Strain engineering and harnessing of the third dimension has opened an entire subfield in 2D mechanics where a crumpled membrane should be considered a metamaterial [128]. For example, with careful induction of defects [129] or otherwise [130, 131], one can design the topography of a 2D material and enhance its properties. It is possible to increase fracture stiffness [132, 133] and induce hydrophobicity [134, 135]. Whilst the commercial application of graphene in MEMS may be in the distant future, the utility in of such MEMS in research is very current. Integration of graphene as a mechanical element to 'lab-on-a-chip' setups facilitates the study of exotic physics not limited to: nonlinear dynamics [136], coupling of mechanical motion to electronics [137] and optics [12], and exploring the quantum regime of mechanical motion [138]. Finally, by replicating paper art such applying folds and cuts (origami and kirigami) [34, 139–142] in graphene, we are becoming closer to the goal of understanding, manipulating, and miniaturizing machinery.

APPENDICES

APPENDIX A

FABRICATION OF 2D MATERIAL DEVICES

Basic fabrication was mentioned in many chapters of this thesis, since it was critical in the design and implementation of many experiments. In this appendix I discuss in detail the procedures and recipes for constructing two-dimensional material devices.

A.1 Procurement and Transfer of Graphene

There are two main methods of procuring graphene: chemical vapor deposition (CVD) and exfoliation. As we wish measure the mechanical response of graphene, it is a requirement that the graphene samples are freely suspended. Therefore various techniques have been developed to remove graphene from the substrate. Graphene can be transferred onto pre-made pores or subsequent etching of sacrificial layers below graphene on a substrate. The graphene remains attached to portions of the sample via van der Waals interactions forming suspended graphene devices.

A.1.1 CVD Graphene

Graphene is one of the easiest materials to grow via CVD and the literature is populated with many different types of growths of various quality and characteristics. We start by following the early recipe by the Ruoff group [8] — a low pressure chemical vapor deposition (LPCVD) growth. We use 25 μm thick copper foils. We have performed the recipe in both 1 inch and 4 inch furnaces with no discernable difference between the growths. The copper foil is cut up into strips that fit onto the boat in the furnace. If the furnace position cannot be controlled, it is essential that the boat can be moved during the growth (e.g. with magnets or otherwise). The foils are cleaned with acetone and IPA for several rinses and then blow dried before being loaded into the furnace. The foils should be loaded into the center of the furnace as quickly as possible to avoid further contamination. The vacuum pump is then turned on and allowed to slowly evacuate the chamber. Once reasonable pressure has been achieved (after 5 minutes or < 100 mTorr), 2 sccm of H_2 is introduced for 1 hour with the furnace heating to 1035°C. This further cleans and removes the copper oxide present on the foils. Then, in conjunction with the hydrogen flow, 35 sccm of CH_4 (methane) is introduced for 30 minutes. Following this with these two gasses are still flowing, the foils are removed from the center of the furnace to its edge where they are quickly cooled. After the furnace has cooled to $< 200^{\circ}$C, the H_2 and CH_4 are turned off and 300 sccm of Ar is introduced to flush all of the active gases and to subsequently vent the chamber. This growth will typically yield grain sizes of $\sim 10\mu$m or greater as shown by inspection after partial growth

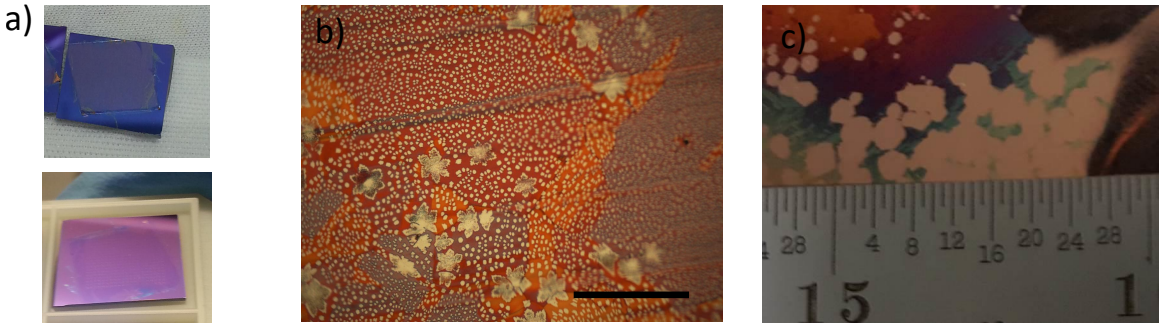

Figure A.1: a) Transfer of graphene onto silicon chip. Top, graphene/PMMA stack on silicon. Bottom, following acetone and IPA cleaning to remove PMMA. b) Partial LPCVD growth, scale bar 50 μm. c) Partial APCVD growth. Grain size is ~ 2.5 mm

Fig. A.1b). This size is sufficient to create electronic devices of $< 1\mu$m in size. However, for the larger mechanical membranes discussed in most of this thesis, larger graphene grain sizes were required.

Before we discuss improved recipes for growth, it is important to mention a number of key factors that can drastically affect the resulting graphene quality. Foil type and thickness, cleaning procedures and foil geometry. Firstly, it has been shown that foils with high oxygen content (Alfa Aesar 99.8% 7440-50-8, oxygen rich 'OR') greatly improve the quality of graphene grown with the above recipe [8]. Alternatively an extremely low flow of oxygen [143] can be introduced during the recipe with regular foils. There is a risk of oxidizing the foils if you do not have precise control of the oxygen flow. Although thin foils are more economical in terms of cost and etching time, they can also be crumpled easily and be very rough microscopically. Therefore it is recommended to use thicker foils for any graphene growth recipe. To the same end, increased graphene quality is achieved using very smooth foils (e.g. [144]) and can be facilitated by mechanically flattening or polishing. Rather than using only acetone and IPA to remove surface contaminants, an overnight etch in glacial acetic acid can remove the copper oxide more effectively. Additionally, acetic acid is a weak copper etchant meaning that it can smooth irregularities and surface roughness. Upon removing the copper from the acid, it should be blow dried and taken directly to the furnace and pumped to vacuum where the growth recipe can continue as normal. Finally, some groups notice that instead of using flat strips of foils, using copper 'pockets' or tubes can improve the quality of graphene by reducing nucleation rate on the interior [145].

To obtain large grain graphene we use a high quality atmospheric growth (APCVD) [146] on 125 μm thick electropolished (in H_3PO_4 [147]) copper foils that yields grain sizes > 50 μm as shown in Fig. A.1 c). In short, the foils are first annealed in a H_2-Ar mixture for 30 minutes. Then partial pressures of methane and hydrogen were controlled by mixing stock gas mixtures, 2.5% of H_2 in Ar and 0.1% of CH_4 in Ar keeping the ratio $\frac{P_{H2}}{P_{CH4}} \sim 1800$. Total flow was kept at 500 sccm during the growth with partial pressure of $H_2 \sim 19$

Torr and $CH_4 \sim 10.5$ mTorr. After the growth the foils are cooled at an initial rate exceeding 50° C/min.

After growth, graphene is transferred from copper. To accomplish this, Microchem 495PMMA A4 photoresist is spin coated onto the copper foils at 1500 RPM. The copper is dissolved in 1M $FeCl_3$ and 3% HCl solution at which point the graphene-PMMA stack will be floating on the surface of the acid. A fresh silicon chip is used to 'fish out' the film for further processing. The films are first transferred to a 3% HCl solution and subsequently rinsed in D.I. water by placing them in consecutive baths and allowing them to rest for at least 5 minutes in each. It is essential to develop a technique to clean the films with enough water otherwise there will be iron particle contamination. There is certainly a trade-off to consider, the more rinsing performed, the more you have to handle the membranes which can potentially damage them. An alternative etchant to use is ammonium sulphate which doesn't have the iron contamination issue. However, the etching reaction is slightly more violent and causes bubbles to form under the films which can only be removed by performing and additional rinse in IPA. It should be noted that the films will not float in an IPA bath, so you should only dip them in this bath momentarily whilst still holding the fishing chip underneath to take it out again. The final step, which finishes the transfer, is to fish out the film onto your device substrate such as a patterned silicon chip which has been O_2 plasma cleaned. The chips are left to dry overnight at room temperature and then baked on a hotplate at 150 °C for 5 minutes. The result is a graphene-PMMA film on your substrate of choice. How to remove the PMMA is discussed in the section below.

A.1.2 Exfoliated Graphene

Next we discuss how to transfer exfoliated graphene rather than CVD graphene. For exfoliated graphene on arbitrary substrates a co-polymer stamp method is used [148, 149]. The first step is to exfoliate graphene flakes onto a transfer slide made from a glass side, block of PDMS and transparent scotch tape spin coated with a copolymer mixture (7.5 g Evlacite powder grade 2550 in 50 ml MIBK) spun at 4000 rpm for 45s and baked for 5 minutes at 100 °C.

The co-polymer layer acts as a sacrificial layer which will be transferred from the slide to your arbitrary substrate. As such, there is risk of accidently removing the layer whilst exfoliating — this happens in about 1 in 10 slides. It is necessary to modify your exfoliation technique to account for this. Since the co-polymer is very sticky it is actually easier to find monolayer flakes compared to silicon. Instead of scratching for 1-2 minutes, all you have to do is carefully and gently apply a little bit of pressure so that the flakes are in contact — this is enough to have lots of candidate flakes remain on the transfer slide. You want to reframe applying excess pressure since this will increase the chance that you will remove the co-polymer layer accidently.

Once candidate graphene flakes are found and confirmed, the transfer slide is aligned to the sample chip (e.g. SiN_x membrane) with a manual x-y stage, brought into contact and heated to 90 °C to melt the co-

polymer layer. This usually takes $\sim$ 5 minutes. You will observe interference fringes spreading as the co-polmer heats indicating that more and more of the co-polymer is sticking to the substrate. After this, the transfer slide is removed from the sample chip and the flake-co-polymer stack should remain on the substrate. How to remove the co-polymer is discussed in the section below. Sometimes the region of the flake is stuck to the substrate, but the co-polymer stretches and doesn't separate from the slide. At this point it is okay to carefully use tweezers or a blade to separate the excess co-polymer from the slide.

If you replace the transparent tape and spin some fresh co-polymer the slides are re-usable. However, if you need to transfer onto fragile substrates (e.g. $<$ 200 nm thick nitride membranes) there is an extra step required during transfer. Prior to loading the transfer slide into the x-y stage a blade is used to cut a very small square (smaller than substrate size) around the flake. The excess PDMS and tape is removed. The transfer proceeds as normal. Then, when you raise up the transfer slide, the PDMS square will remain on top of the substrate/ It can then be carefully removed. This procedure is much more gentle and allows the co-polymer to separate with relative ease, however it comes with the downside of the transfer slides not being reusable. Finally, to transfer onto thick substrates (such as polypropylene) the heater stage will not raise the temperature of the top surface enough to melt the co-polymer. Therefore, a simple solution is to use a heat gun aimed at the sides of the stack during transfer. Again, the rest of the transfer procedure is the same as described above.

A.1.3 Identifying Monolayer Graphene

It is important to know how to distinguish monolayer graphene from bulk or even bilayer specimens. There are typically a number of complimentary techniques such as optical contrast measurements, AFM for height measurements or Raman spectroscopy. Raman spectroscopy is by far the easiest and most reliable method to identify monolayer samples, even though over time you will become confident identifying monolayer flakes by eye.

Here I discuss briefly how Raman is used to confirm monolayer samples. Figure A.3 shows typical Raman spectra of graphene on a variety of substrates that are encountered during fabrication. The Raman spectrum of freestanding graphene is similar to that supported on silicon. Graphene on copolymer is encountered when using transfer slides (as discussed above). Finally, there graphene on copper is following CVD growths. From the Raman spectrum it is hard to tell the quality of graphene on metal due to the additional scattering from the surface but it is a least possible to confirm whether or not it is present.

There are a three key characteristics which should be noted to confirm high quality monolayer samples. The first is peak position. The $2D$ peak should be situated $\sim 2700\,\mathrm{cm}^{-1}$ (depends on laser excitation) and the G peak should be $\sim 1580\,\mathrm{cm}^{-1}$. The second is $2D$ peak shape. For bulk samples the $2D$ peak is asymmetric

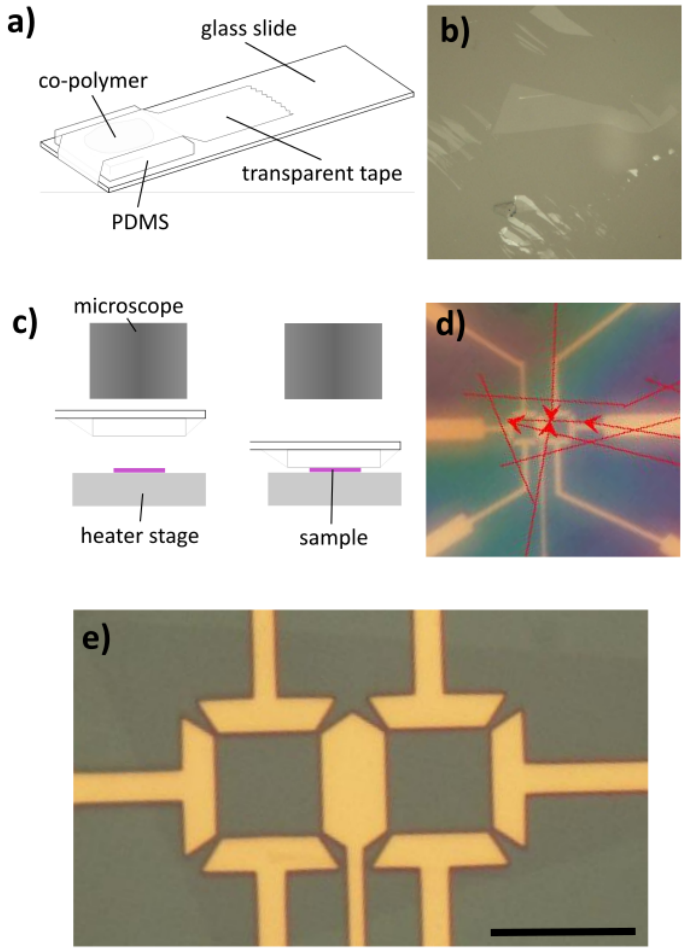

Figure A.2: Example of a device fabricated with the co-polymer stamp method: a) Sketch of prepared transfer slide b) 50x objective optical image showing candidate transfer flake. e) Sketch of transfer set-up d) Reference image taken during transfer — the interference fringes confirm the flake is in intimate contact with the substrate. The red lines are drawn in software to act as guides during the procedure since the flake on co-polymer is almost invisible due to the reflection from the substrate. e) Successful transfer of flake to device, scale bar 10μm.

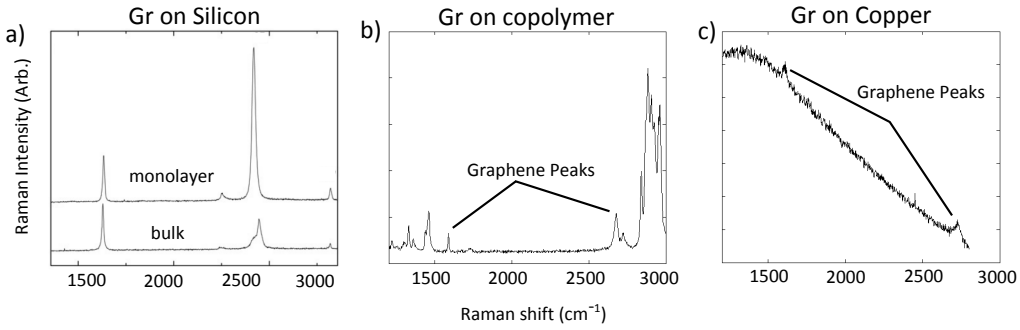

Figure A.3: Characteristic Raman spectra of graphene. a) Bulk and monolayer specimins on Silicon (from [150]) b) Expected spectra on copolymer (transfer slide) where there are lots of spurious peaks not related to graphene c) Spectra of CVD growth on top of copper.

and has an extra feature. For monolayer, the $2D$ peak should be perfectly Lorentzian. Third is peak intensity. Here it should be checked that the intensity of the $2D$ peak, $I(2D)$, is much greater than the intensity of the G peak, $I(G)$, and specifically the ratio between them should be $\frac{I(2D)}{I(G)} \sim 3$.

A.1.4 Cleaning Samples

To remove the PMMA or co-polymer (if present), the samples are left in acetone for up to 1 hour before being dipped in IPA and gently blow dried with N_2. At no point during this cleaning procedure are the samples rinsed from the squeeze bottle — this risks the removal of graphene from the substrate. The likelihood of this is high especially for for transferred flakes.

There are primarily two methods to remove excess polymer residues after the wet cleaning step. The first is vacuum annealing. It is only suitable for chip-based devices that can withstand high temperature. The samples are placed inside a furnace in a Ar-H_2 environment and heated to 350 °C for 1 hour. The second is current annealing which is only suitable for electrical ribbon based devices that can be placed in vacuum. There is no set recipe since the current will depend on the geometry of the device, contact resistance and other components in the circuit (like protective resistors), but the general idea is to pass high current through the device which locally heats the sample. The polymer can re-flow with the thermal gradient (from center of device to the edges which act as heat sinks) but mainly, since the device is in vacuum, the polymer can volatilize and leave the sample. The procedure can be lengthy and is associated with a risk of destroying devices. Typically an as-fabricated graphene ribbon will have poor electrical quality, even when suspended, as evidenced by resistance vs gate voltage (V_g) measurements. The source drain voltage (V_{sd}) is increased gradually whilst measuring device resistance. Whenever a sudden jump occurs in resistance the V_{sd} should be held constant until the changes stop. Then a V_g sweep is performed to monitor the quality. The procedure is continued (to higher current or alternate V_{sd} polarity) until a high quality gate sweep is seen with a Dirac point close to 0 V. This indicates a very clean sample. For special samples that cannot be cleaned with either of the above methods, it is possible to use laser illumination with increasing power to locally heat the sample. This method is not typical, less reliable and harder to reproduce than either of the previously discussed techniques.

A.2 Circular graphene drums on Silicon Nitride (SiN_x) membranes

300 nm thick single crystal silicon (100) double-side polished wafers were used as a starting material. Low-stress silicon-rich silicon nitride ($\sim 100 - 1000$ nm) was deposited on both sides using LPCVD. Two photolithography patterning steps were successively performed using a contact aligner as follows. First, the front side of each wafer was patterned to define the pores over which graphene will be eventually suspended (typically $5 - 30$ μm). For this purpose, positive photoresist 955 CM 2.1 spun at 3000 RPM for 45 s was exposed

for 11 s on the contact aligner and developed for 1 min in CD 26. Although not strictly required, a post-bake for 1 min 30 seconds was performed to further harden the resist.

The pattern in the resist can be transferred into the silicon nitride in one of two ways: by applying an anisotropic reactive ion etch in a mixed C_4F_8:SF_6 plasma or a ICP sputter etch (Oxford Plasma Technology Plasma Pro 100 tool). The RIE was timed until all the silicon nitride in the pore regions was completely removed. To achieve reproducible etch rates, whenever small regions of the wafer are exposed (such as the front side pattern), small chips of bare silicon are attached to the wafer. The area dependance of the etch rate is usually only important for reactive recipes, but it was found to be important for the sputter recipe also.

After stripping the remaining resist in NMP at 70 °C, etch windows and cleaving lines were defined on the back side of each wafer using back side optical alignment to the front side pattern. The same resist, exposure time, resist development conditions and RIE recipe were used for the front and back side lithography. After resist removal, wafers with patterned silicon nitride layers on both sides were transferred into a beaker with 30% KOH solution for the bulk silicon etching. The silicon nitride acts as a mask for the silicon. To ensure the wafers are as clean as possible after the etch, a surfactant in the form of ~ 10 ml of IPA was added to the KOH before etching. During the etch KOH solution was maintained at $80 - 85$ °C while the beaker was covered with a condenser. The etching was carried out until no silicon was remaining in the square regions behind silicon nitride membranes (determined by visual inspection under back illumination). The etching typically takes $\sim 4 - 5$ hours, since IPA reduces the etch rate. After completing the KOH etch, the wafers were thoroughly rinsed with copious amounts of DI water and carefully blow dried. If there are any residues after the etch, this means that the wafers were not cleaned enough beforehand. The residues were found to decrease the adhesion of transferred graphene even with additional O_2 plasma cleaning afterwards. If an electrode is required for gating (e.g. chapter 3). Evaporation of 30 nm Au layer on 10 nm of Ti was carried out at a rate of 0.1 nm/s in a Thermionics dual e-gun evaporator.

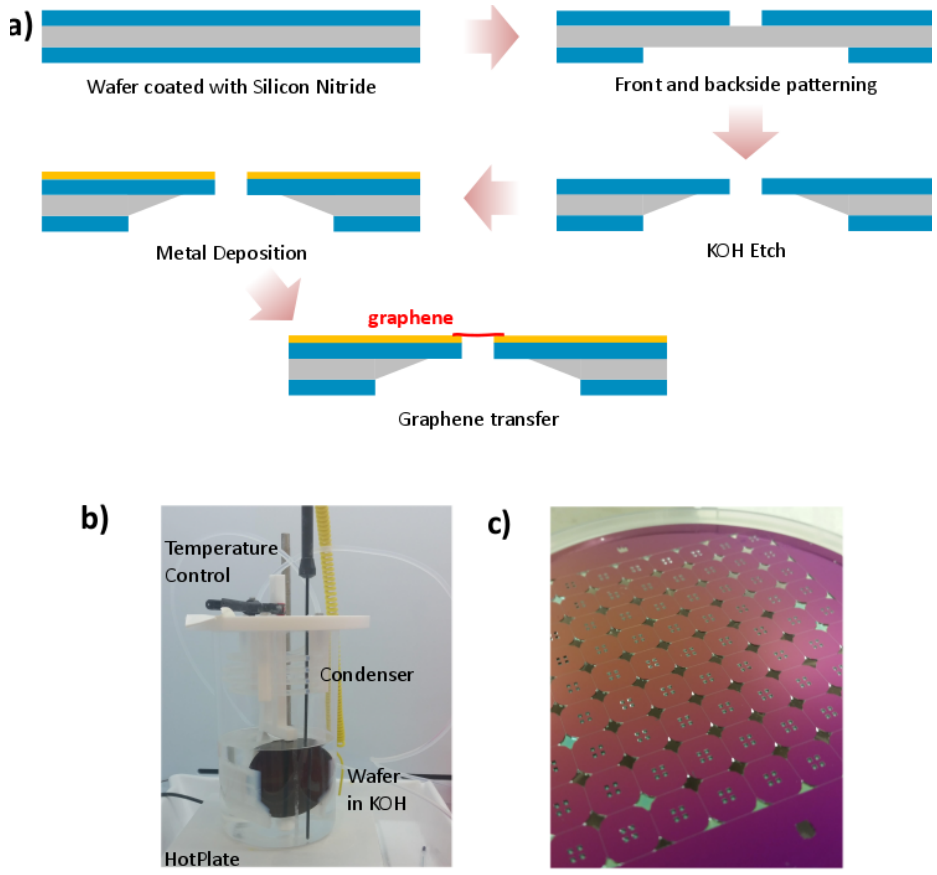

Figure A.4: Fabrication of suspended silicon nitride membranes with pores: a) Process flow including front and backside patterning with photolithography and sputter etching, KOH etching and graphene transfer. b) KOH etching setup allowing a full cassette of wafers to be etched at high temperatures. The condenser consists of a coil of tubing with cold water flowing through it to ensure the concentration of the KOH doesn't change significantly over the course of the etch. c) A finished wafer viewed from the backside. You can clearly see the trenches formed by the KOH — in this case there are four trenches per chip. The wafer is easily broken up into the respective chips by applying a small amount of pressure with tweezers to the defined cleaving boundary.

APPENDIX B

AFM FORCE MEASUREMENTS

AFM nanoindentation is a very important method to characterize the mechanical properties of membranes. This method is described in detail in Refs. [25, 57] and supporting information. In short, a sharp tip on the end of an AFM cantilever of known spring constant and radius is pushed into the center of a suspended sample of known dimensions. The deflection response of the AFM cantilever reveals the deformation of the membrane under the applied forces. Therefore one can accurately extract key parameters about the membrane such as in-plane stiffness and built-in stress. An advantage of this method is that one can also load the membranes to their breaking point which allows characterization of yield strength. In this appendix I discuss these measurements.

B.1 Preparation of samples

Exfoliated or CVD graphene is transferred onto silicon nitride (SiN_x) membranes with holes of varied size described in appendix A — this will create graphene membranes that are suspended and circular. Typically the SiN_x membranes were at least 300 nm thickness and < 500 μm in lateral size so that there was no chance of the SiN_x itself deforming under load. Hole sizes for the graphene membranes are often $1 - 10$ μm. Unless you have extremely high quality graphene and very good transfer techniques, membranes beyond 10μm can break very easily. An easy way to determine candidate graphene membranes is to view them in a SEM — this avoids the pain of trying to find samples with AFM imaging which is very slow in comparison.

B.2 Data collection

The standard tips used for these experiments were Budget Sensors Multi75Al. They offer good tapping and indentation response. Candidate membranes are first imaged in tapping mode. Initially a quick low resolution scan is performed to very roughly center the membrane in the field of view which is followed by a high resolution scan. The high resolution scan is used to minimize the uncertainty of finding the center point of the membrane which is essential since the indentation models are designed assuming perfect center load. For example, if your field of view is 10×10 μm^2 and you scan size is 256×256 lines, the uncertainty in your center point determination is ~ 40 nm. Once the center is found accurately, you should make a note of the x-y co-ordinates so you can return to it precisely.

Prior to indentation, the cantilever spring constant ($k \sim 3$ N/m) is measured via thermal tuning when the cantilever is far from the sample. This will allow determination of the force applied to graphene. The

deflection sensitivity of the cantilever ($\sim$ 100 nm/V) is obtained by pushing it against a hard substrate far from the graphene membranes, which allows you to disentangle the difference in cantilever response from pure bending and actually indenting a sample. These parameters should be checked before every indentation test. The tips should be changed frequently.

Finally, the sample is indented in contact mode at the determined center point co-ordinates. A good rule of thumb is to indent to at least $500 - 1000$nN of force, often set by having a deflection set-point (this is discussed in the next section). It is critical to properly set the ramp speed and data density to have enough points in the range where graphene is being indented because the cantilever will start many microns above the sample meaning a large portion of the measurement will be deadspace with no response. Many indentations can be performed within a matter of seconds which allows for easy collection of statistics and comparing multiple runs. The raw data collected is piezo voltages corresponding to ramp distance z and cantilever deflection δ from photodetector differential voltage, which is often automatically converted to distances. It is good practice to periodically check these calibrations. An indentation test consists of a loading and unloading cycle. The data you should use to determine the mechanical properties of the membrane is the loading curve. The unloading curve will be hysteric due to graphene adhering to the AFM tip and exhibit a large retraction spring back that can be mistaken for the indentation zero point.

B.3 Analysis of indentation curves

Equations B.1 and B.2 show the most common models for AFM indentation of thin materials:

$$F = \sigma_0 \pi h + E_{2D} q^3 \frac{h^3}{a^2} \tag{B.1}$$

$$F = \frac{\sigma_0 2\pi h}{\ln a/r} + E_{2D} q^3 \frac{h^3}{a^2} \tag{B.2}$$

where a is membrane radius, r is AFM tip radius, σ_0 is built-in stress, E_{2D} is in-plane stiffness, h indentation depth and constant $q = 1.02$ is related to the Poisons ratio of graphene. For the large membranes used in the majority of this thesis there is no significant difference by fitting to either of these expressions. An example of successful analysis is shown in Figure B.1.

The hardest part of analysis is the transformation of ramp distance z and deflection δ to force and indentation, even though the equations are trivial: $F = -k\delta$ and $h = z - \delta$. The reason is the difficulty in finding the zero point of indentation. This issue is covered in great detail in the supplementary information of Ref. [25]. The zero point is the instance on the force vs. deflection curve where the tip *just* touches the membrane. Small inaccuracies in finding this point can lead to large uncertainties in the end results. The most common method to determine zero point is to is to find the flat region in the derivative of force vs. time plots $\frac{dF}{dt}(t)$.

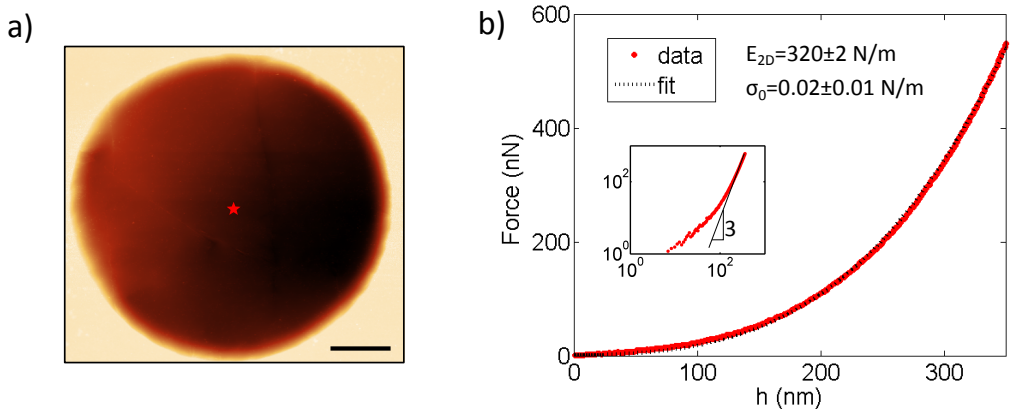

Figure B.1: AFM indentation of graphene membrane. a) High resolution (512×512) tapping mode image. Red star shows location of indentation test. Scale bar :2 μm. b) Results of indentation including fit parameters than are in agreement with monolayer graphene measurements. Inset shows log-log of data approaching a slope of 3 at high h

This allows the best guess of where the forces between the cantilever and membrane are in equilibrium. It is for this reason that decreasing ramp speed and increasing data point density can be of great help. Once you know the time, and from known ramp speed, you know exactly at what point during the z ramp you should designate $h = 0$. Another subtle aspect is ensuring that you indent the membranes enough to reach the regime of cubic response. The cubic term in Eq. B.1 and B.2 is important for fitting for Youngs modulus. A way to check this is to plot the $F(h)$ data as a log-log plot and confirm a slope that approaches 3 as shown in the inset of Fig. B.1b . For a given size of membrane, you will then know the typical force you will have to apply to reach this and the corresponding deflection that you can use in your measurements. These issues have been investigated deeply and the accuracy of the AFM indentation method for thin materials has recently been called into question [100].

Often during loading, especially when using forces $1 - 3$ μN, the membrane will break. This allows us to determine the breaking stress of our membranes. From a tip loading model you can estimate the maximum stress from Eq. B.3:

$$\sigma_{max} = \left(\frac{F E_{2D}}{4\pi r} \right). \tag{B.3}$$

The tips used here have a documented tip radius of 10 nm but to get more accurate results you may have to use specialized tips or measure the tip radius (which can be time consuming and challenging). Here we found the breaking stress $40 - 50$ N/m, which again is in good agreement with other works [25].

APPENDIX C

STRAIN ENGINEERING TECHNIQUES

Strain engineering is important in the mechanics of 2D materials. Many schemes require specialized setups or complicated fabrication. Here I present some new ways to control strain that are very simple to achieve on a silicon chip with no more than three layers of lithography, including graphene patterning. The first technique is 'controlled collapse' where the 2D material is allowed to be pulled down to an underlaying substrate. The second technique is MEMS actuators, where the 2D material is suspended between two cantilevers that can be moved. With either approach we can engineer strain up to 0.2 %.

C.1 Controlled Collapse

One prominent mode of failure of suspending 2D material devices during fabrication is 'collapse'. Instead of the membrane freely suspending as shown in Fig. C.1a, it touches down and adheres to the underlaying substrate (Fig. C.1b). We suggest using this effect to create controllable strain in 2D materials.

To suspend micron-sized devices on silicon, a very careful critical point dry (CPD) is typically performed. Controllably collapsed devices on the other hand are fabricated by a faster CPD procedure or none at all. To create strain engineered devices on SiN_x suitable for mechanics measurements as used in chapter 4, they must be suspended over open holes in SiN_x. To accomplish this, we patterned an additional $\sim 50 - 100$ nm deep, 5 μm wide recess in the SiN_x around the edges of the holes in SiN_x. Then, when graphene is transferred it is pulled into the recess by Van der Waals forces. From geometrical considerations, this process is expected to impart ≤ 1 % strain on graphene. A comparison of standard and strain-engineered devices is shown in Fig. C.2a. By transferring onto these pre-defined insets, graphene is pulled-in by Van der Waals forces thereby

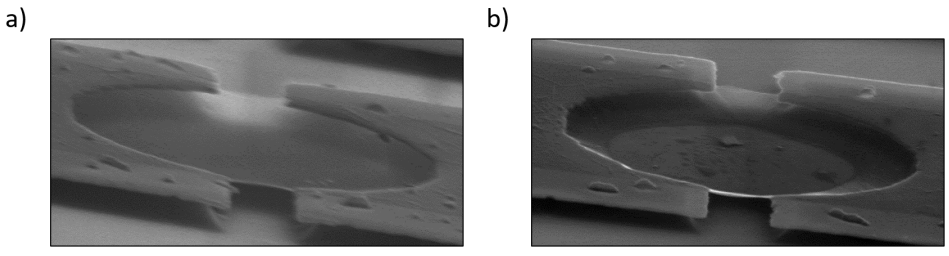

Figure C.1: High angle SEM of graphene drums. a) A large graphene sample suspended by HF etching and the subsequent CPD b) Similar collapsed samples fabricated by drying quickly, allowing graphene to 'collapse' and adhere onto the underlying substrate.

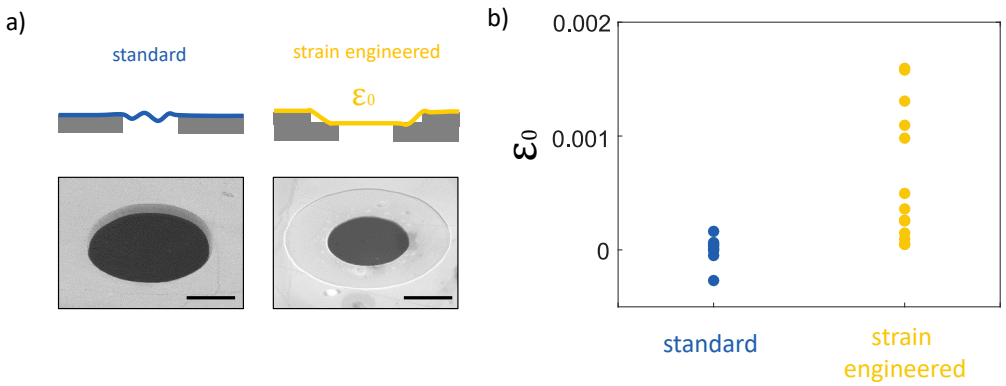

Figure C.2: a) Top row: Cartoon views of standard and strain-engineered devices. Bottom row: scanning electron microscopy (SEM) images of representative samples (scale bar is 5 μm) b) Strain of standard and strain engineered samples for $P = 0$ determined from Raman spectroscopy (described in chapter 4). Here, $\varepsilon = 0$ is defined as the average of all standard devices. The strain-engineered devices, on average, show higher levels of built-in strain.

creating strained samples. A comparison of the built-in strain of standard and strain-engineered devices is shown in Fig. C.2b. Strain engineered devices show significantly higher built-in strain on average, up to a max strain of ~ 0.2 %. The effectiveness of strain engineering depends on many factors including: whether the membranes stay perfectly intact, if there is slipping during transfer and if the inset is large enough to unravel the hidden area present in graphene prior to transfer.

Overall, this method will require more research into 2D material adhesion to enable engineering a specific amount of strain. For now, patterns with large insets allow creating flat/strained suspended graphene.

C.2 MEMS actuators

A more elaborate way to strain 2D materials is with the help of MEMS actuators. This is another piece of microfabricated machinery to apply forces or extension to graphene in real time. Such devices can be actuated thermally (heater lines) and electrically (comb drive and piezo's) and typically consist of many moving parts [23].

Here, we created our own very simple MEMS actuators fabricated with only a few layers of lithography. The mechanism behind the design is simple. The MEMS actuators induce strain by suspending graphene between two movable cantilever supports. When the cantilever supports are bent downwards, the distance between the support edges increase and the graphene between them is stretched. To fabricate such structures, we design a typical suspended graphene sample with thin metal electrodes (Fig. C.3). The design was made so that the width of the electrodes was < 600 nm so that etching away the underlaying 300 nm of SiO_2 would also suspend the electrodes forming cantilever actuators. The thickness of the cantilever was chosen to be ~ 90 nm, 3 times thicker than typical electrical contacts so they would be stiff enough to support themselves.

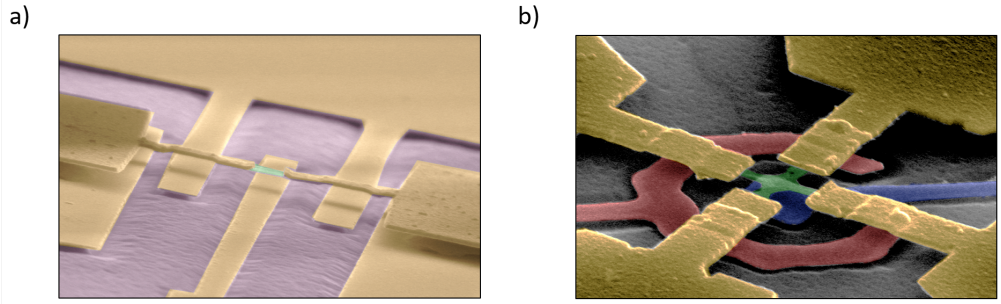

Figure C.3: MEMS actuators to strain graphene a) 2-probe and b) 4-probe schemes. False color: green is graphene, yellow is the movable gold supports. For the 4-probe device red is actuation electrodes and blue is an additional gate electrode.

Critical point drying allowed the fabrication of up to ~ 3 μm long cantilevers. The longer the cantilevers, the more strain that can be induced via bending. These cantilevers can be bent electrostatically with a gate voltage between the cantilevers and electrodes underneath or pushed downwards with another manipulator e.g. AFM tip. From FEA simulations we expect to achieve 0.5 $\%$ strain for ~ 10 V (Fig. C.4a). In experiment, we saw repeatable modulation of strain up to ~ 0.05 $\%$ strain as measured from Raman spectroscopy in the 2-probe device for $0 - 40$ V as shown in Fig. C.4b. We attribute the difference between experiment and FEA to imprecise knowledge of the Young's modulus and built-in stress of the gold supports.

We also demonstrate the successful fabrication of a 4-probe device geometry shown in Fig. C.3b. This may be useful for more detailed transport measurements or studying strain induced pseudomagnetic fields [30]. In this geometry, strain is induced along two, instead of one direction. Graphene that is patterned into a cross shape is suspended between four movable supports, with the same design considerations as discussed above. As the supports are bent downwards, the graphene between them is stretched. In experiment, the graphene ruptured before any modulation of strain could be observed. The failure was likely due to the edges in the cross pattern of graphene. A reasonable step forward would be using Si or SiN_x cantilevers in a 2-probe geometry to be actuated by AFM since electrostatic actuation is not desirable if electronic properties are going to be measured due to unwanted gating.

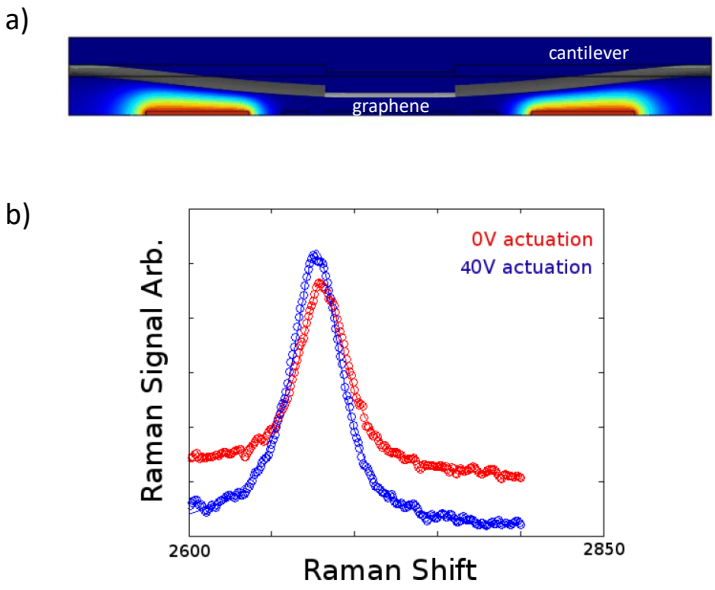

Figure C.4: Modelling and experiment in 2-probe MEMS actuators used to strain graphene. a) Cross-section of COMSOL model for deflecting cantilevers at 10 V with graphene in between. Color is electric potential, dark blue is 0V. $0.5\ \%$ strain is obtainable with 10 V of actuation on the cantilevers. This model also confirms that there should be no doping effect due to applied voltage since graphene is sufficiently far away. b) Strain induced Raman shift of a graphene nanoribbon by actuating gold electrodes by 40 V.

BIBLIOGRAPHY

[1] *Website: https://en.wikipedia.org/wiki/10_nanometer*, en, Page Version ID: 777555485, Apr. 2017.

[2] V. V. Gobre and A. Tkatchenko, "Scaling laws for van der Waals interactions in nanostructured materials", en, Nature Communications **4**, 2341 (2013).

[3] L. Liang, H. Ma, and Y. Wei, "Size-Dependent Elastic Modulus and Vibration Frequency of Nanocrystals", en, Journal of Nanomaterials **2011**, e670857 (2010).

[4] X.-Y. Zhou, B.-L. Huang, and T.-Y. Zhang, "Size- and temperature-dependent Young's modulus and size-dependent thermal expansion coefficient of thin films", en, Physical Chemistry Chemical Physics **18**, 21508–21517 (2016).

[5] "Nanoelectromechanical systems", Review of Scientific Instruments **76**, 061101 (2005).

[6] S. Z. Butler, S. M. Hollen, L. Cao, Y. Cui, J. A. Gupta, H. R. Gutiérrez, T. F. Heinz, S. S. Hong, J. Huang, A. F. Ismach, E. Johnston-Halperin, M. Kuno, V. V. Plashnitsa, R. D. Robinson, R. S. Ruoff, S. Salahuddin, J. Shan, L. Shi, M. G. Spencer, M. Terrones, W. Windl, and J. E. Goldberger, "Progress, Challenges, and Opportunities in Two-Dimensional Materials Beyond Graphene", ACS Nano **7**, 2898–2926 (2013).

[7] A. H. Castro Neto, F. Guinea, N. M. R. Peres, K. S. Novoselov, and A. K. Geim, "The electronic properties of graphene", Reviews of Modern Physics **81**, 109–162 (2009).

[8] X. Li, W. Cai, J. An, S. Kim, J. Nah, D. Yang, R. Piner, A. Velamakanni, I. Jung, E. Tutuc, S. K. Banerjee, L. Colombo, and R. S. Ruoff, "Large-Area Synthesis of High-Quality and Uniform Graphene Films on Copper Foils", en, Science **324**, 1312–1314 (2009).

[9] J. S. Bunch, A. M. v. d. Zande, S. S. Verbridge, I. W. Frank, D. M. Tanenbaum, J. M. Parpia, H. G. Craighead, and P. L. McEuen, "Electromechanical Resonators from Graphene Sheets", en, Science **315**, 490–493 (2007).

[10] X. Liu, J. W. Suk, N. G. Boddeti, L. Cantley, L. Wang, J. M. Gray, H. J. Hall, V. M. Bright, C. T. Rogers, M. L. Dunn, R. S. Ruoff, and J. S. Bunch, "Large Arrays and Properties of 3-Terminal Graphene Nanoelectromechanical Switches", en, Advanced Materials **26**, 1571–1576 (2014).

[11]C. Chen, S. Rosenblatt, K. I. Bolotin, W. Kalb, P. Kim, I. Kymissis, H. L. Stormer, T. F. Heinz, and J. Hone, "Performance of monolayer graphene nanomechanical resonators with electrical readout", en, Nature Nanotechnology **4**, 861–867 (2009).

[12]R. D. Alba, F. Massel, I. R. Storch, T. S. Abhilash, A. Hui, P. L. McEuen, H. G. Craighead, and J. M. Parpia, "Tunable phonon-cavity coupling in graphene membranes", en, Nature Nanotechnology **11**, 741–746 (2016).

[13]K. I. Bolotin, K. J. Sikes, Z. Jiang, M. Klima, G. Fudenberg, J. Hone, P. Kim, and H. L. Stormer, "Ultrahigh electron mobility in suspended graphene", Solid State Communications **146**, 351–355 (2008).

[14]A. K. Geim and K. S. Novoselov, "The rise of graphene", Nature Materials **6**, 183–191 (2007).

[15]D. R. Cooper, B. D'Anjou, N. Ghattamaneni, B. Harack, M. Hilke, A. Horth, N. Majlis, M. Massicotte, L. Vandsburger, E. Whiteway, and V. Yu, "Experimental review of graphene", arXiv:1110.6557 (2011).

[16]F. Schwierz, "Graphene transistors", en, Nature Nanotechnology **5**, 487–496 (2010).

[17]T. J. Booth, P. Blake, R. R. Nair, D. Jiang, E. W. Hill, U. Bangert, A. Bleloch, M. Gass, K. S. Novoselov, M. I. Katsnelson, and A. K. Geim, "Macroscopic Graphene Membranes and Their Extraordinary Stiffness", Nano Letters **8**, 2442–2446 (2008).

[18]A. A. Balandin, S. Ghosh, W. Bao, I. Calizo, D. Teweldebrhan, F. Miao, and C. N. Lau, "Superior Thermal Conductivity of Single-Layer Graphene", Nano Letters **8**, 902–907 (2008).

[19]J. S. Bunch, S. S. Verbridge, J. S. Alden, A. M. van der Zande, J. M. Parpia, H. G. Craighead, and P. L. McEuen, "Impermeable Atomic Membranes from Graphene Sheets", Nano Letters **8**, 2458–2462 (2008).

[20]J. S. Bunch, S. S. Verbridge, J. S. Alden, A. M. van der Zande, J. M. Parpia, H. G. Craighead, and P. L. McEuen, "Impermeable Atomic Membranes from Graphene Sheets", Nano Letters **8**, 2458–2462 (2008).

[21]J.-U. Lee, D. Yoon, and H. Cheong, "Estimation of Young's Modulus of Graphene by Raman Spectroscopy", Nano Letters **12**, 4444–4448 (2012).

[22]T. M. G. Mohiuddin, A. Lombardo, R. R. Nair, A. Bonetti, G. Savini, R. Jalil, N. Bonini, D. M. Basko, C. Galiotis, N. Marzari, K. S. Novoselov, A. K. Geim, and A. C. Ferrari, "Uniaxial strain in graphene

by Raman spectroscopy: G peak splitting, Gr\"uneisen parameters, and sample orientation", Physical Review B **79**, 205433 (2009).

[23]P. Zhang, L. Ma, F. Fan, Z. Zeng, C. Peng, P. E. Loya, Z. Liu, Y. Gong, J. Zhang, X. Zhang, P. M. Ajayan, T. Zhu, and J. Lou, "Fracture toughness of graphene", en, Nature Communications **5** (2014) 10.1038/ncomms4782.

[24]R. Nicklow, N. Wakabayashi, and H. G. Smith, "Lattice Dynamics of Pyrolytic Graphite", Physical Review B **5**, 4951–4962 (1972).

[25]C. Lee, X. Wei, J. W. Kysar, and J. Hone, "Measurement of the Elastic Properties and Intrinsic Strength of Monolayer Graphene", en, Science **321**, 385–388 (2008).

[26]F. Liu, P. Ming, and J. Li, "Ab initio calculation of ideal strength and phonon instability of graphene under tension", Physical Review B **76**, 064120 (2007).

[27]T. Zhu and J. Li, "Ultra-strength materials", Progress in Materials Science **55**, 710–757 (2010).

[28]C. Chen, S. Lee, V. V. Deshpande, G.-H. Lee, M. Lekas, K. Shepard, and J. Hone, "Graphene mechanical oscillators with tunable frequency", en, Nature Nanotechnology **8**, 923–927 (2013).

[29]V. M. Pereira, A. H. Castro Neto, and N. M. R. Peres, "Tight-binding approach to uniaxial strain in graphene", Physical Review B **80**, 045401 (2009).

[30]F. Guinea, M. I. Katsnelson, and A. K. Geim, "Energy gaps and a zero-field quantum Hall effect in graphene by strain engineering", en, Nature Physics **6**, 30–33 (2010).

[31]N. Lindahl, D. Midtvedt, J. Svensson, O. A. Nerushev, N. Lindvall, A. Isacsson, and E. E. B. Campbell, "Determination of the Bending Rigidity of Graphene via Electrostatic Actuation of Buckled Membranes", Nano Letters **12**, 3526–3531 (2012).

[32]A. Reserbat-Plantey, L. Marty, O. Arcizet, N. Bendiab, and V. Bouchiat, "A local optical probe for measuring motion and stress in a nanoelectromechanical system", en, Nature Nanotechnology **7**, 151–155 (2012).

[33]K. Matsui, A. Inaba, Y. Oshidari, Y. Takei, H. Takahashi, T. Takahata, R. Kometani, K. Matsumoto, and I. Shimoyama, "Mechanical properties of few layer graphene cantilever", in 2014 IEEE 27th International Conference on Micro Electro Mechanical Systems (MEMS) (Jan. 2014), pp. 1087–1090.

[34]M. K. Blees, A. W. Barnard, P. A. Rose, S. P. Roberts, K. L. McGill, P. Y. Huang, A. R. Ruyack, J. W. Kevek, B. Kobrin, D. A. Muller, and P. L. McEuen, "Graphene kirigami", en, Nature **524**, 204–207 (2015).

[35]J.-W. Jiang, "Graphene versus mos2: a short review", Frontiers of Physics **10**, 287–302 (2015).

[36]W. Wong and S. Pellegrino, "Wrinkled membranes I: experiments", Journal of Mechanics of Materials and Structures **1**, 3–25 (2006).

[37]E. Cerda and L. Mahadevan, "Geometry and Physics of Wrinkling", Physical Review Letters **90**, 074302 (2003).

[38]J. Genzer and J. Groenewold, "Soft matter with hard skin: From skin wrinkles to templating and material characterization", en, **2**, 310–323 (2006).

[39]N. Liu, Z. Pan, L. Fu, C. Zhang, B. Dai, and Z. Liu, "The origin of wrinkles on transferred graphene", en, Nano Research **4**, 996–1004 (2011).

[40]S. Deng and V. Berry, "Wrinkled, rippled and crumpled graphene: an overview of formation mechanism, electronic properties, and applications", Materials Today **19**, 197–212 (2016).

[41]W. Bao, F. Miao, Z. Chen, H. Zhang, W. Jang, C. Dames, and C. N. Lau, "Controlled ripple texturing of suspended graphene and ultrathin graphite membranes", Nature Nanotechnology **4**, 562–566 (2009).

[42]A. Fasolino, J. H. Los, and M. I. Katsnelson, "Intrinsic ripples in graphene", en, Nature Materials **6**, 858–861 (2007).

[43]J. C. Meyer, A. K. Geim, M. I. Katsnelson, K. S. Novoselov, T. J. Booth, and S. Roth, "The structure of suspended graphene sheets", Nature **446**, 60–63 (2007).

[44]R. Ramírez, E. Chacón, and C. P. Herrero, "Anharmonic effects in the optical and acoustic bending modes of graphene", Physical Review B **93**, 235419 (2016).

[45]D. A. Kirilenko, A. T. Dideykin, and G. Van Tendeloo, "Measuring the corrugation amplitude of suspended and supported graphene", Physical Review B **84**, 235417 (2011).

[46]W. Helfrich and R.-M. Servuss, "Undulations, steric interaction and cohesion of fluid membranes", en, Il Nuovo Cimento D **3**, 137–151 (1984).

[47]E. Evans and W. Rawicz, "Entropy-driven tension and bending elasticity in condensed-fluid membranes", Physical Review Letters **64**, 2094–2097 (1990).

[48]J. F. Marko and E. D. Siggia, "Stretching DNA", Macromolecules **28**, 8759–8770 (1995).

[49]D. Nelson and L. Peliti, "Fluctuations in membranes with crystalline and hexatic order", Journal de Physique **48**, 1085–1092 (1987).

[50]J. A. Aronovitz and T. C. Lubensky, "Fluctuations of Solid Membranes", Physical Review Letters **60**, 2634–2637 (1988).

[51]A. Košmrlj and D. R. Nelson, "Thermal excitations of warped membranes", Physical Review E **89**, 022126 (2014).

[52]A. Košmrlj and D. R. Nelson, "Response of thermalized ribbons to pulling and bending", Physical Review B **93**, 125431 (2016).

[53]I. V. Gornyi, V. Y. Kachorovskii, and A. D. Mirlin, "Rippling and crumpling in disordered free-standing graphene", Physical Review B **92**, 155428 (2015).

[54]J. H. Los, A. Fasolino, and M. I. Katsnelson, "Scaling Behavior and Strain Dependence of In-Plane Elastic Properties of Graphene", Physical Review Letters **116**, 015901 (2016).

[55]M. J. Bowick, A. Kosmrlj, D. R. Nelson, and R. Sknepnek, "Non-Hookean statistical mechanics of clamped graphene ribbons", arXiv:1608.04197 [cond-mat], arXiv: 1608.04197 (2016).

[56]D. Wan, D. R. Nelson, and M. J. Bowick, "Thermal stiffening of clamped elastic ribbons", arXiv:1702.01863 [cond-mat], arXiv: 1702.01863 (2017).

[57]C. S. Ruiz-Vargas, H. L. Zhuang, P. Y. Huang, A. M. van der Zande, S. Garg, P. L. McEuen, D. A. Muller, R. G. Hennig, and J. Park, "Softened Elastic Response and Unzipping in Chemical Vapor Deposition Graphene Membranes", Nano Letters **11**, 2259–2263 (2011).

[58]A. Košmrlj and D. R. Nelson, "Mechanical properties of warped membranes", Physical Review E **88**, 012136 (2013).

[59]J.-W. Jiang, T. Chang, X. Guo, and H. S. Park, "Intrinsic Negative Poisson's Ratio for Single-Layer Graphene", Nano Letters (2016) 10.1021/acs.nanolett.6b02538.

[60]J.-W. Jiang and H. S. Park, "Negative Poisson's Ratio in Single-Layer Graphene Ribbons", Nano Letters **16**, 2657–2662 (2016).

[61]D. Yoon, Y.-W. Son, and H. Cheong, "Negative Thermal Expansion Coefficient of Graphene Measured by Raman Spectroscopy", Nano Letters **11**, 3227–3231 (2011).

[62]P. L. de Andres, F. Guinea, and M. I. Katsnelson, "Density functional theory analysis of flexural modes, elastic constants, and corrugations in strained graphene", Physical Review B **86**, 245409 (2012).

[63]I. V. Gornyi, V. Y. Kachorovskii, and A. D. Mirlin, "Anomalous Hooke's law in disordered graphene", en, 2D Materials **4**, 011003 (2017).

[64]L. Lindsay, D. A. Broido, and N. Mingo, "Flexural phonons and thermal transport in graphene", Physical Review B **82**, 115427 (2010).

[65]A. Laitinen, M. Oksanen, A. Fay, D. Cox, M. Tomi, P. Virtanen, and P. J. Hakonen, "Electron–Phonon Coupling in Suspended Graphene: Supercollisions by Ripples", Nano Letters **14**, 3009–3013 (2014).

[66]K. I. Bolotin, K. J. Sikes, J. Hone, H. L. Stormer, and P. Kim, "Temperature-Dependent Transport in Suspended Graphene", Physical Review Letters **101**, 096802 (2008).

[67]M. I. Katsnelson and A. Fasolino, "Graphene as a Prototype Crystalline Membrane", Accounts of Chemical Research **46**, 97–105 (2013).

[68]G. López-Polín, C. Gómez-Navarro, V. Parente, F. Guinea, M. I. Katsnelson, F. Pérez-Murano, and J. Gómez-Herrero, "Increasing the elastic modulus of graphene by controlled defect creation", en, Nature Physics **advance online publication** (2014) 10.1038/nphys3183.

[69]L. D. Landau, E. M. Lifshitz, A. M. Kosevich, and L. P. Pitaevskiĭ, *Theory of Elasticity*, en (Elsevier, 1986).

[70]M. H. Sadd, *Elasticity: Theory, Applications, and Numerics*, en (Academic Press, Jan. 2014).

[71]J. Vlassak and W. Nix, "A new bulge test technique for the determination of Young's modulus and Poisson's ratio of thin films", Journal of Materials Research **7**, 3242–3249 (1992).

[72]I. H. S. (Clive L. Dym, *Solid mechanics: a variational approach, augmented edition*, 1st ed. (Springer-Verlag New York, 2013).

[73]M. I. Katsnelson and M. I. Kat?s?nel'son, *Graphene: Carbon in Two Dimensions*, en (Cambridge University Press, Apr. 2012).

[74]U. Komaragiri, M. R. Begley, and J. G. Simmonds, "The Mechanical Response of Freestanding Circular Elastic Films Under Point and Pressure Loads", Journal of Applied Mechanics **72**, 203–212 (2005).

[75]H. Hencky, *Der Spannungszustand in rechteckigen Platten*, de, Google-Books-ID: QV1YAAAAYAAJ (R. Oldenbourg, 1913).

[76]M. K. Small and W. Nix, "Analysis of the accuracy of the bulge test in determining the mechanical properties of thin films", Journal of Materials Research **7**, 1553–1563 (1992).

[77]W. B. Fichter, *Some Solutions for the Large Deflections of Uniformly Loaded Circular Membranes*, tech. rep. (July 1997).

[78]E. W. Schweitzer and M. Göken, "In situ bulge testing in an atomic force microscope: microdeformation experiments of thin film membranes", Journal of Materials Research 22.10 (2013).

[79]"A nondestructive method for determining the spring constant of cantilevers for scanning force microscopy", Review of Scientific Instruments **64**, 403–405 (1993).

[80]R. Ramírez and C. P. Herrero, "Elastic properties and mechanical tension of graphene", Physical Review B **95**, 045423 (2017).

[81]W. Wong and S. Pellegrino, "Wrinkled membranes II: analytical models", Journal of Mechanics of Materials and Structures **1**, 27–61 (2006).

[82]H. Vandeparre, M. Piñeirua, F. Brau, B. Roman, J. Bico, C. Gay, W. Bao, C. Lau, P. Reis, and P. Damman, "Wrinkling Hierarchy in Constrained Thin Sheets from Suspended Graphene to Curtains", Physical Review Letters **106**, 224301 (2011).

[83]D. Briassoulis, "Equivalent orthotropic properties of corrugated sheets", Computers & Structures **23**, 129–138 (1986).

[84]L. X. Peng, K. M. Liew, and S. Kitipornchai, "Analysis of stiffened corrugated plates based on the FSDT via the mesh-free method", International Journal of Mechanical Sciences **49**, 364–378 (2007).

[85]W. Wong and S. Pellegrino, "Wrinkled membranes III: numerical simulations", Journal of Mechanics of Materials and Structures **1**, 63–95 (2006).

[86]P. L. de Andres, F. Guinea, and M. I. Katsnelson, "Bending modes, anharmonic effects, and thermal expansion coefficient in single-layer and multilayer graphene", Physical Review B **86**, 144103 (2012).

[87]R. Roldán, A. Fasolino, K. V. Zakharchenko, and M. I. Katsnelson, "Suppression of anharmonicities in crystalline membranes by external strain", Physical Review B **83**, 174104 (2011).

[88]J. H. Los, A. Fasolino, and M. I. Katsnelson, "Mechanics of thermally fluctuating membranes", arXiv:1703.08400 [cond-mat], arXiv: 1703.08400 (2017).

[89]P. Blake, "Making graphene visible", Applied Physics Letters **91**, 063124 (2007).

[90]R. A. Barton, I. R. Storch, V. P. Adiga, R. Sakakibara, B. R. Cipriany, B. Ilic, S. P. Wang, P. Ong, P. L. McEuen, J. M. Parpia, and H. G. Craighead, "Photothermal Self-Oscillation and Laser Cooling of Graphene Optomechanical Systems", Nano Letters **12**, 4681–4686 (2012).

[91]D. Davidovikj, J. J. Slim, S. J. Cartamil-Bueno, H. S. J. van der Zant, P. G. Steeneken, and W. J. Venstra, "Visualizing the Motion of Graphene Nanodrums", Nano Letters **16**, 2768–2773 (2016).

[92]R. R. Nair, P. Blake, A. N. Grigorenko, K. S. Novoselov, T. J. Booth, T. Stauber, N. M. R. Peres, and A. K. Geim, "Fine Structure Constant Defines Visual Transparency of Graphene", en, Science **320**, 1308–1308 (2008).

[93]G.-H. Lee, R. C. Cooper, S. J. An, S. Lee, A. v. d. Zande, N. Petrone, A. G. Hammerberg, C. Lee, B. Crawford, W. Oliver, J. W. Kysar, and J. Hone, "High-Strength Chemical-Vapor–Deposited Graphene and Grain Boundaries", en, Science **340**, 1073–1076 (2013).

[94]Y.-C. Lin, C.-C. Lu, C.-H. Yeh, C. Jin, K. Suenaga, and P.-W. Chiu, "Graphene Annealing: How Clean Can It Be?", Nano Letters **12**, 414–419 (2012).

[95]J. A. Johnson and D. W. Jones, "The mechanical properties of PMMA and its copolymers with ethyl methacrylate and butyl methacrylate", en, Journal of Materials Science **29**, 870–876 (1994).

[96]E. H. Mansfield, "Tension field theory, a new approach which shows its duality with inextensional theory", en, in *Applied Mechanics*, DOI: 10.1007/978-3-642-85640-2_23 (Springer, Berlin, Heidelberg, 1969), pp. 305–320.

[97]D. J. Steigmann, "Tension-Field Theory", en, Proceedings of the Royal Society of London A: Mathematical, Physical and Engineering Sciences **429**, 141–173 (1990).

[98]A. Zandiatashbar, G.-H. Lee, S. J. An, S. Lee, N. Mathew, M. Terrones, T. Hayashi, C. R. Picu, J. Hone, and N. Koratkar, "Effect of defects on the intrinsic strength and stiffness of graphene", en, Nature Communications **5** (2014) 10.1038/ncomms4186.

[99]T. Zhang, X. Li, and H. Gao, "Fracture of graphene: a review", en, International Journal of Fracture **196**, 1–31 (2015).

[100]D. Vella and B. Davidovitch, "Indentation metrology of clamped, ultra-thin elastic sheets", en, Soft Matter **13**, 2264–2278 (2017).

[101]A. Eckmann, A. Felten, A. Mishchenko, L. Britnell, R. Krupke, K. S. Novoselov, and C. Casiraghi, "Probing the Nature of Defects in Graphene by Raman Spectroscopy", Nano Letters **12**, 3925–3930 (2012).

[102]L. G. Cançado, A. Jorio, E. H. M. Ferreira, F. Stavale, C. A. Achete, R. B. Capaz, M. V. O. Moutinho, A. Lombardo, T. S. Kulmala, and A. C. Ferrari, "Quantifying Defects in Graphene via Raman Spectroscopy at Different Excitation Energies", Nano Letters **11**, 3190–3196 (2011).

[103]O. Lehtinen, J. Kotakoski, A. V. Krasheninnikov, and J. Keinonen, "Cutting and controlled modification of graphene with ion beams", en, Nanotechnology **22**, 175306 (2011).

[104]S. P. Koenig, N. G. Boddeti, M. L. Dunn, and J. S. Bunch, "Ultrastrong adhesion of graphene membranes", en, Nature Nanotechnology **6**, 543–546 (2011).

[105]A. C. Ferrari and D. M. Basko, "Raman spectroscopy as a versatile tool for studying the properties of graphene", en, Nature Nanotechnology **8**, 235–246 (2013).

[106]J. E. Lee, G. Ahn, J. Shim, Y. S. Lee, and S. Ryu, "Optical separation of mechanical strain from charge doping in graphene", en, Nature Communications **3**, 1024 (2012).

[107]R. Narula and S. Reich, "Probing LO phonons of graphene under tension via the2d' Raman mode", Physical Review B **87**, 115424 (2013).

[108]C. Metzger, S. Rémi, M. Liu, S. V. Kusminskiy, A. H. Castro Neto, A. K. Swan, and B. B. Goldberg, "Biaxial Strain in Graphene Adhered to Shallow Depressions", Nano Letters **10**, 6–10 (2010).

[109]C. Androulidakis, E. N. Koukaras, J. Parthenios, G. Kalosakas, K. Papagelis, and C. Galiotis, "Graphene flakes under controlled biaxial deformation", Scientific Reports **5**, 18219 (2015).

[110]D. Metten, F. Federspiel, M. Romeo, and S. Berciaud, "All-Optical Blister Test of Suspended Graphene Using Micro-Raman Spectroscopy", Physical Review Applied **2**, 054008 (2014).

[111]T. J. Booth, P. Blake, R. R. Nair, D. Jiang, E. W. Hill, U. Bangert, A. Bleloch, M. Gass, K. S. Novoselov, M. I. Katsnelson, and A. K. Geim, "Macroscopic Graphene Membranes and Their Extraordinary Stiffness", Nano Letters **8**, 2442–2446 (2008).

[112]W. Gao and R. Huang, "Thermomechanics of monolayer graphene: Rippling, thermal expansion and elasticity", Journal of the Mechanics and Physics of Solids **66**, 42–58 (2014).

[113]C. Berger, M. Dirschka, and A. Vijayaraghavan, "Ultra-thin graphene-polymer heterostructure membranes", en, Nanoscale (2016) 10.1039/C6NR06316K.

[114]A. Beck and H. Grabmüller, "Wrinkle-free solutions in the theory of curved circular membranes", en, Journal of Engineering Mathematics **27**, 389–409 (1993).

[115]C. D. Coman and A. P. Bassom, "Boundary Layers and Stress Concentration in the Circular Shearing of Annular Thin Films", Proceedings: Mathematical, Physical and Engineering Sciences **463**, 3037–3053 (2007).

[116]O. Martynov, "Carbon nanotube stabilized single layer graphene cantilevers", Applied Physics Letters **110**, 151901 (2017).

[117]V. Pini, J. J. Ruz, P. M. Kosaka, O. Malvar, M. Calleja, and J. Tamayo, "How two-dimensional bending can extraordinarily stiffen thin sheets", en, Scientific Reports **6**, 29627 (2016).

[118]"Gas-assisted focused electron beam and ion beam processing and fabrication", Journal of Vacuum Science & Technology B: Microelectronics and Nanometer Structures Processing, Measurement, and Phenomena **26**, 1197–1276 (2008).

[119]P. Poulin, R. Jalili, W. Neri, F. Nallet, T. Divoux, A. Colin, S. H. Aboutalebi, G. Wallace, and C. Zakri, "Superflexibility of graphene oxide", Proceedings of the National Academy of Sciences of the United States of America **113**, 11088–11093 (2016).

[120]W. Bao, K. Myhro, Z. Zhao, Z. Chen, W. Jang, L. Jing, F. Miao, H. Zhang, C. Dames, and C. N. Lau, "In Situ Observation of Electrostatic and Thermal Manipulation of Suspended Graphene Membranes", Nano Letters **12**, 5470–5474 (2012).

[121]A. M. Fennimore, T. D. Yuzvinsky, W.-Q. Han, M. S. Fuhrer, J. Cumings, and A. Zettl, "Rotational actuators based on carbon nanotubes", en, Nature **424**, 408–410 (2003).

[122]R. Cuerno, R. Gallardo Caballero, A. Gordillo-Guerrero, P. Monroy, and J. J. Ruiz-Lorenzo, "Universal behavior of crystalline membranes: Crumpling transition and Poisson ratio of the flat phase", Physical Review E **93**, 022111 (2016).

[123]Y. Guo, J. Qiu, and W. Guo, "Tunable bending stiffness of MoSe 2 /WSe 2 heterobilayers from flexural wrinkling", en, Nanotechnology **28**, 195701 (2017).

[124]S. Bertolazzi, J. Brivio, and A. Kis, "Stretching and Breaking of Ultrathin MoS2", ACS Nano **5**, 9703–9709 (2011).

[125]S. Xiong and G. Cao, "Bending response of single layer MoS 2", en, Nanotechnology **27**, 105701 (2016).

[126]N. E. Firsova and Y. A. Firsov, "A new loss mechanism in graphene nanoresonators due to the synthetic electric fields caused by inherent out-of-plane membrane corrugations", en, Journal of Physics D: Applied Physics **45**, 435102 (2012).

[127]C. G. Wang, L. Lan, Y. P. Liu, H. F. Tan, and X. D. He, "Vibration characteristics of wrinkled single-layered graphene sheets", International Journal of Solids and Structures **50**, 1812–1823 (2013).

[128]X. Li and H. Gao, "Mechanical metamaterials: Smaller and stronger", en, Nature Materials **15**, 373–374 (2016).

[129]T. Zhang, X. Li, and H. Gao, "Defects controlled wrinkling and topological design in graphene", Journal of the Mechanics and Physics of Solids **67**, 2–13 (2014).

[130]W.-K. Lee, J. Kang, K.-S. Chen, C. J. Engel, W.-B. Jung, D. Rhee, M. C. Hersam, and T. W. Odom, "Multiscale, Hierarchical Patterning of Graphene by Conformal Wrinkling", Nano Letters **16**, 7121–7127 (2016).

[131]P.-Y. Chen, J. Sodhi, Y. Qiu, T. M. Valentin, R. S. Steinberg, Z. Wang, R. H. Hurt, and I. Y. Wong, "Multiscale Graphene Topographies Programmed by Sequential Mechanical Deformation", en, Advanced Materials **28**, 3564–3571 (2016).

[132]G. López-Polín, J. Gómez-Herrero, and C. Gómez-Navarro, "Confining Crack Propagation in Defective Graphene", Nano Letters **15**, 2050–2054 (2015).

[133]Y. Ren and G. Cao, "Effect of geometrical defects on the tensile properties of graphene", Carbon **103**, 125–133 (2016).

[134]C. Feng, Z. Yi, F. She, W. Gao, Z. Peng, C. J. Garvey, L. F. Dumée, and L. Kong, "Superhydrophobic and Superoleophilic Micro-Wrinkled Reduced Graphene Oxide as a Highly Portable and Recyclable Oil Sorbent", ACS Applied Materials & Interfaces **8**, 9977–9985 (2016).

[135]W.-K. Lee, W.-B. Jung, S. R. Nagel, and T. W. Odom, "Stretchable Superhydrophobicity from Monolithic, Three-Dimensional Hierarchical Wrinkles", Nano Letters **16**, 3774–3779 (2016).

[136]V. Singh, O. Shevchuk, Y. M. Blanter, and G. A. Steele, "Negative nonlinear damping of a multilayer graphene mechanical resonator", Phys. Rev. B **93**, 245407 (2016).

[137]G. Luo, Z.-Z. Zhang, G.-W. Deng, H.-O. Li, G. Cao, M. Xiao, G.-C. Guo, and G.-P. Guo, "Coupling graphene nanomechanical motion to a single-electron transistor", Nanoscale **9**, 5608–5614 (2017).

[138]J. D. Teufel, T. Donner, D. Li, J. W. Harlow, M. S. Allman, K. Cicak, A. J. Sirois, J. D. Whittaker, K. W. Lehnert, and R. W. Simmonds, "Sideband cooling of micromechanical motion to the quantum ground state", en, Nature **475**, 359–363 (2011).

[139]T. C. Shyu, P. F. Damasceno, P. M. Dodd, A. Lamoureux, L. Xu, M. Shlian, M. Shtein, S. C. Glotzer, and N. A. Kotov, "A kirigami approach to engineering elasticity in nanocomposites through patterned defects", en, Nature Materials **14**, 785–789 (2015).

[140]B. G.-g. Chen, B. Liu, A. A. Evans, J. Paulose, I. Cohen, V. Vitelli, and C. D. Santangelo, "Topological Mechanics of Origami and Kirigami", Physical Review Letters **116**, 135501 (2016).

[141]T. S. Shim, Z. G. Estephan, Z. Qian, J. H. Prosser, S. Y. Lee, D. M. Chenoweth, D. Lee, S.-J. Park, and J. C. Crocker, "Shape changing thin films powered by DNA hybridization", en, Nature Nanotechnology **12**, 41–47 (2017).

[142]D. Joung, A. Nemilentsau, K. Agarwal, C. Dai, C. Liu, Q. Su, J. Li, T. Low, S. J. Koester, and J.-H. Cho, "Self-Assembled Three-Dimensional Graphene-Based Polyhedrons Inducing Volumetric Light Confinement", Nano Letters **17**, 1987–1994 (2017).

[143]Y. Hao, M. S. Bharathi, L. Wang, Y. Liu, H. Chen, S. Nie, X. Wang, H. Chou, C. Tan, B. Fallahazad, H. Ramanarayan, C. W. Magnuson, E. Tutuc, B. I. Yakobson, K. F. McCarty, Y.-W. Zhang, P. Kim, J. Hone, L. Colombo, and R. S. Ruoff, "The Role of Surface Oxygen in the Growth of Large Single-Crystal Graphene on Copper", en, Science **342**, 720–723 (2013).

[144]P. Procházka, J. Mach, D. Bischoff, Z. Lišková, P. Dvořák, M. Vaňatka, P. Simonet, A. Varlet, D. Hemzal, M. Petrenec, L. Kalina, M. Bartošík, K. Ensslin, P. Varga, J. Čechal, and T. Šikola, "Ultrasmooth metallic foils for growth of high quality graphene by chemical vapor deposition", eng, Nanotechnology **25**, 185601 (2014).

[145]S. Chen, H. Ji, H. Chou, Q. Li, H. Li, J. W. Suk, R. Piner, L. Liao, W. Cai, and R. S. Ruoff, "Millimeter-Size Single-Crystal Graphene by Suppressing Evaporative Loss of Cu During Low Pressure Chemical Vapor Deposition", en, Advanced Materials **25**, 2062–2065 (2013).

[146]I. Vlassiouk, P. Fulvio, H. Meyer, N. Lavrik, S. Dai, P. Datskos, and S. Smirnov, "Large scale atmospheric pressure chemical vapor deposition of graphene", Carbon **54**, 58–67 (2013).

[147]I. Vlassiouk, S. Smirnov, M. Regmi, S. P. Surwade, N. Srivastava, R. Feenstra, G. Eres, C. Parish, N. Lavrik, P. Datskos, S. Dai, and P. Fulvio, "Graphene Nucleation Density on Copper: Fundamental Role of Background Pressure", The Journal of Physical Chemistry C **117**, 18919–18926 (2013).

[148]P. J. Zomer, S. P. Dash, N. Tombros, and B. J. v. Wees, "A transfer technique for high mobility graphene devices on commercially available hexagonal boron nitride", Applied Physics Letters **99**, 232104 (2011).

[149]C. R. Dean, A. F. Young, I. Meric, C. Lee, L. Wang, S. Sorgenfrei, K. Watanabe, T. Taniguchi, P. Kim, K. L. Shepard, and J. Hone, "Boron nitride substrates for high-quality graphene electronics", en, Nature Nanotechnology **5**, 722–726 (2010).

[150]A. C. Ferrari, J. C. Meyer, V. Scardaci, C. Casiraghi, M. Lazzeri, F. Mauri, S. Piscanec, D. Jiang, K. S. Novoselov, S. Roth, and A. K. Geim, "Raman Spectrum of Graphene and Graphene Layers", Physical Review Letters **97**, 187401 (2006).